DISSERTATION/ DOCTORAL THESIS

Titel der Dissertation / Title of the Doctoral Thesis

„Mechanical properties and phase transformation of biocompatible nanostructured Ti-Nb alloys processed by severe plastic deformation"

verfasst von / submitted by

Ajit Panigrahi

angestrebter akademischer Grad / in partial fulfilment of the requirements for the degree of

Doktor der Naturwissenschaften (Dr. rer. nat)

Wien, 2016 / Vienna, 2016

Studienkennzahl lt. Studienblatt/ degree programme code as it appears on the student record sheet:	A 796 605 411
Dissertationsgebiet (lt. Studienblatt)/ field of study as it appears on the student record sheet:	Physik
Betreuer von / Supervisor:	ao. Univ. -Prof. Dr. Michael J. Zehetbauer ao. Univ. -Prof. Dr. Thomas Waitz

Abstract

The current thesis investigates the mechanical properties and phase transformations in biocompatible Ti-Nb alloys before and after processing with different methods of „Severe Plastic Deformation – SPD". The phase structure of the Ti-Nb alloys has a strong impact to the mechanical properties like the strength as well as the elastic constants. These quantities are highly important for the materials' suitability for orthopaedic applications. Here a sufficient strength of the implant is equally essential as a low Young's modulus, in order to avoid the adverse stress shielding effect which, after orthopaedic surgery, might lead to the successive degradation of the bone.

As the Young's modulus of Ti-Nb alloys shows two pronounced minima at compositions near 16.0 and 45.0 wt.% Nb, these alloys were selected for this thesis. Different SPD techniques including high pressure torsion (HPT), and rolling and folding (R&F) were applied.

In case of Ti–16.1 wt.% Nb, SPD processing strongly affected the phase stability. Even if a hydrostatic pressure was applied solely, a partial transformation of the parent α''-martensite to the ω-phase and α/α' occurred. Adding plastic shear deformation by HPT a nanocrystalline ω-phase formed at the expense of parent α'' which – according to in-situ Synchrotron diffraction experiments – showed a very high thermal stability. Annealing after HPT yielded an ultrafine grained and equiaxed ($\alpha+\beta$) phase structure which hardly can be reached by another processing route. The SPD induced formation of the ω-phase was also the reason why the Young's modulus of the Ti–16.1 Nb alloy strongly increased, which has been confirmed by successfully modelling the Young's modulus in terms of the measured phase fractions using a rule of mixture. Considering the plastic strength of the material, not only marked dislocation and grain boundary hardening occurred but also a large strength increase of the phase fractions was observed. Again, modelling with a rule of mixture was successful.

In case of SPD processed Ti–45.0 wt.% Nb, no phase transformations occurred; therefore the apparent Young's modulus did not increase upon SPD, even slightly decreased because of SPD specific texture evolution. In spite of missing hardening from phase transformation, the HPT induced increase of strength was still pronounced while maintaining a considerable ductility. This is very promising for the applicability of this alloy for medical implants having a strong potential to substitute traditional implant materials such as Ti–6Al–4V containing toxic elements.

Kurzfassung

Die vorliegende Dissertation untersucht die mechanischen Eigenschaften und Phasenumwandlungen in biokompatiblen Ti-Nb Legierungen vor und nach Bearbeitung mit verschiedenen Methoden der „Severe Plastic Deformation – SPD". Die Phasenstruktur der Ti-Nb Legierungen hat auf deren mechanische Eigenschaften wie die Festigkeit und die elastischen Konstanten einen starken Einfluß. Diese Größen sind für die Eignung des Materials für orthopädischen Anwendungen von entscheidender Bedeutung. Dabei ist eine ausreichende Festigkeit des Implantats genauso essentiell wie ein kleiner Elastizitätsmodul, mit dem der Spannungs-Abschirmeffekt vermieden wird, der nach der Operation zu einem sukzessiven Knochenabbau führen kann.

Da der Elastizitätsmodul von Ti-Nb Legierungen zwei ausgeprägte Minima bei den Konzentrationen 16 und 45 Gew.% Nb zeigt, wurden diese beiden Legierungen für die vorliegende Dissertation ausgesucht. Verschiedene SPD Techniken (u.a. Hochdrucktorsion – HPT, sowie Walzen & Falten (R&D)) gelangten dabei zur Anwendung.

Im Fall von Ti–16.1 Gew.% Nb zeigte die SPD-Bearbeitung einen starken Einfluß auf die Phasenstabilität. Selbst das bloße Anlegen eines erhöhten hydrostatischen Drucks führte bereits zu einer Teilumwandlung des ursprünglichen α"-Martensits zu einer ω-Phase bzw. zu zwei koexistierenden α/α′ Phasen. Wurde das Material zusätzlich auch plastisch scherverformt mittels HPT bildete sich eine nanokristalline ω-Phase auf Kosten des ursprünglichen α"-Martensits. Dabei wies diese ω-Phase zufolge von in-situ Synchrotron Beugungsexperimenten eine sehr hohe thermische Stabilität auf. Thermische Behandlung nach HPT führte zu einer ultrafeinen gleichachsigen (α+β) Phasen–Struktur, die sich nur schwer mit anderen Herstellungsrouten realisieren lässt. Die SPD-induzierte Bildung der ω-Phase führte auch zu einer starken Erhöhung des Elastizitätsmoduls der Ti–16.1 Gew.% Nb Legierung, was durch Modellierung mithilfe der Elastizitätsmodule der gemessenen, einzelnen Phasenanteile mittels Anwendung einer Mischungsregel quantitativ bestätigt wurde. Zur Festigkeitssteigerung des Materials tragen nicht nur Versetzungen und Korngrenzen bei, sondern auch die Festigkeiten der verschiedenen Phasenanteile, was ebenfalls durch Anwendung einer Mischungsregel quantitativ beschrieben werden konnte.

Im Fall der SPD Behandlung von Ti–45.0 Gew.% Nb wurde keine Phasenumwandlung beobachtet. Deshalb nahm auch der Elastizitätsmodul nicht zu, sondern eher – je nach Art der SPD Behandlung – texturbedingt ab. Trotz des fehlenden Anteils der Phasenhärtung war die HPT-induzierte Festigkeitszunahme immer noch deutlich, zudem aber ergab sich auch eine beträchtliche Duktilität. Diese Resultate scheinen im Hinblick auf die Einsetzbarkeit des Materials für Implantate vielversprechend bzw. hat diese Legierung ein hohes Potential für den Ersatz der traditionellen Implantantmaterialien wie Ti–6Al–4V, die toxische Elemente enthalten.

Table of contents

1. Introduction & Aim of the Thesis

In recent years the research in the field of nanostructured materials processed by severe plastic deformation (SPD) has attracted growing interest because of their unique physical as well as functional properties. In particular, the strength of metals and alloys can be substantially enhanced by the application of SPD owing to the exceptional grain refinement and introduction of a high density of defects which is not achievable by conventional thermo-mechanical treatments in their coarse grained counterparts [1–3]. In addition, using methods of SPD bulk nanocrystalline materials driven far from their thermodynamic equilibrium can be obtained. Grain size at the nano-scale also strongly impacts the stability of phases as well as the kinetics of phase transformations. Elastic properties dependent on the texture of a polycrystalline aggregate may arise during SPD. All of these SPD effects can strongly impact the mechanical properties.

In the present PhD thesis, the microstructure and mechanical properties of Ti–Nb alloys subjected to SPD were systematically studied. The research was carried out within the framework of the Marie Curie Research Training Network "BioTiNet" focusing on alloys such as Ti–Nb, Ti–Nb–Zr and Ti–Nb–Ta–Zr subjected to different methods SPD These materials can show rather low values of the Young's modulus E. In general, E depends strongly on the chemical composition and thermomechanical processing via the formation of various equilibrium and metastable lattice structures arising both by diffusional and diffusionless phase transformations. In general the body centered cubic β lattice structure and the orthorhombic α''-martensite phase both show low values of E while that of the hexagonal phases α, α'-martensite and ω-phase are rather high; this can be summarized as $E_\omega > E_{\alpha'} > E_{\alpha''} > E_\beta$ [4].

A low value of the Young's modulus of a material is of particular importance for its applicability to implants. A large difference of the values of E between the implant material and humane bone limits the stress transfer to the bone (stress shielding effect [5]) causing the death of bone cells and therefore loosening and premature failure of the implant. Ti–Nb based alloys can show a low value of E near that of the human bone (E = 4–30 GPa [6]); $E_{Ti-16.1\ Nb}$ = 65 GPa (containing entirely α''-martensitic structure) [7,8], $E_{Ti-45.0Nb}$ = 65 GPa (containing entirely β-phase)[9], $E_{Ti-13Nb-13Zr}$ = 77 GPa (mixture of α' and β) [6]. In comparison, conventional implants materials such as stainless steel (E = 206 GPa [10]), Co–Cr based alloys (E = 240 GPa [10]), Ti–6Al–4V (E = 110 GPa [10]), and pure Ti (E = 100 GPa [10]) have rather high values of the Young's modulus. Therefore, Ti–Nb based alloys have a strong potential for orthopaedic applications. Besides the low Young's modulus these materials also show excellent biocompatibility [11] and high corrosion resistance [12,13]. However, despite of these rather superior properties alloys the replacement of conventional

biomaterials by Ti–Nb based is hindered so far because of the lower strength [10]. Therefore, a central aim of the present PhD thesis is to elucidate the physical conditions of SPD suitable to achieve Ti–Nb alloys with a tailored combination of high strength and low Young's modulus.

To achieve the aims of the PhD thesis, two Ti–Nb alloys were carefully selected for the investigations. The alloys containing 16.1 and 45.0 wt.% Nb both show low values of E. However, in their coarse grained state the lattice structures of the alloys differ: Ti–16.1 and Ti–45.0 Nb show α"-martensite and the β-phase, respectively, at room temperature. Methods of SPD include high pressure torsion (HPT, application of a high hydrostatic pressure and a high strain) and rolling and folding (R&F, relatively low hydrostatic pressure and strain). In addition, the samples were subjected to hydrostatic pressure only. This allows to separately investigate the impact of plastic strain and hydrostatic pressure on the microstructure formation and mechanical properties. The microstructure, phase evolution and mechanical properties were investigated using a combination of X-ray diffraction (XRD), Transmission Electron Microscopy (TEM), Differential Scanning Calorimetry (DSC), nanoindentation tests, microhardness measurements, and tensile tests. Rietveld analyses were carried out to evaluate the phase fractions before and after SPD. In the case of Ti–16.1 Nb, the thermal stability of the SPD induced phases were studied using in-situ heating experiments in the European Synchrotron Facility ESRF in Grenoble, France. In the case of Ti–45.0 Nb, XRD diffraction profiles were subjected to a line profile analysis to measure the dislocation density and coherent domain size. Texture investigations were also performed to investigate the effect of texture on the Young's modulus in Ti–45.0 Nb alloy.

2. Background

2.1. Ti–Nb based alloy system

2.1.1. Pure Ti and P-T phase diagram

The chemical element Ti belongs to the transition metals, positioned in the group of IV in the periodic table. Its electronic configuration is [Ar] $3d^2 4s^2$ having four valence electrons. The d orbitals are partially occupied and screened by the outer S electrons. It has a melting point of 1668°C, exhibits hexagonal close packed (hcp) structure at ambient conditions and undergoes an allotropic transformation from α-hexagonal to β-body centered cubic (bcc) phase at a temperature of 882.5 °C [14,15].

Upon the application of a pressure in the range of 3 to 9 GPa [16–18]) a transformation from to the α-phase to a hexagonal ω-phase was reported, see the P-T diagram of Ti depicted in **Fig. 2.1**. The triple point where α-, β-, and ω-phases coincide occurs at a pressure of ~ 9 GPa and a temperature of 667°C [14,19,20]. The extrapolation of the ω↔β phase boundary to a pressure of 0 GPa gives the hypothetical ω↔β transformation temperature in theabsence of the α-phase is 470°C[21]. With addition of shear along with pressure, the sensitivity of this transformation increases as the activation barrier for α→ω transformation with shear decreases [19]. Therefore, with the aid of shear deformation bulk nanocrystalline ω-phase can be achieved in pure Ti [22–25] at relatively low pressure. In order to alter this transformation Ti must be annealed to a temperature of $T_{\omega \to \alpha} = 150°C$ [22,24].

2.1.2. Ti–Nb alloys and phase diagrams

It is well known that Ti can form extensive substitutional solid solution with most of the elements within variation of about 20% in the atomic size factor [14] and thus enable it to form binary (Ti–Zr, Ti–Mo, Ti–V, Ti–Al, Ti–Co etc.), ternary (Ti–Nb–Zr, Ti–Nb–Al, Ti–Nb–Sn, Ti–Al–V, Ti–Al–Fe etc.), and quaternary (Ti–Nb–Ta–Zr, Ti–Mo–Zr–Fe, Ti–Mo–Zr–Al etc.) alloy systems. These titanium alloys are broadly classified into α, (α+β), and β-alloys depending on their alloying content and type of alloying elements. The non-transition metals such as Al and interstitial elements such as C, N, and O raise α/β transformation temperature and therefore regarded as α-stabilizers [14,26,27]. Similarly, the transition metals raising the extent of β-field are considered as β-stabilizers. The β-stabilizers [26] involve two types: β-eutectoid (the elements which show a limited solubility in the β-phase and decompose into

α-phase and intermetallic phases with the elements: Cu, Ni, Cr) and β-isomorphous (the elements which are soluble in the β-phase such as Mo, Nb, Ta, W, and V).
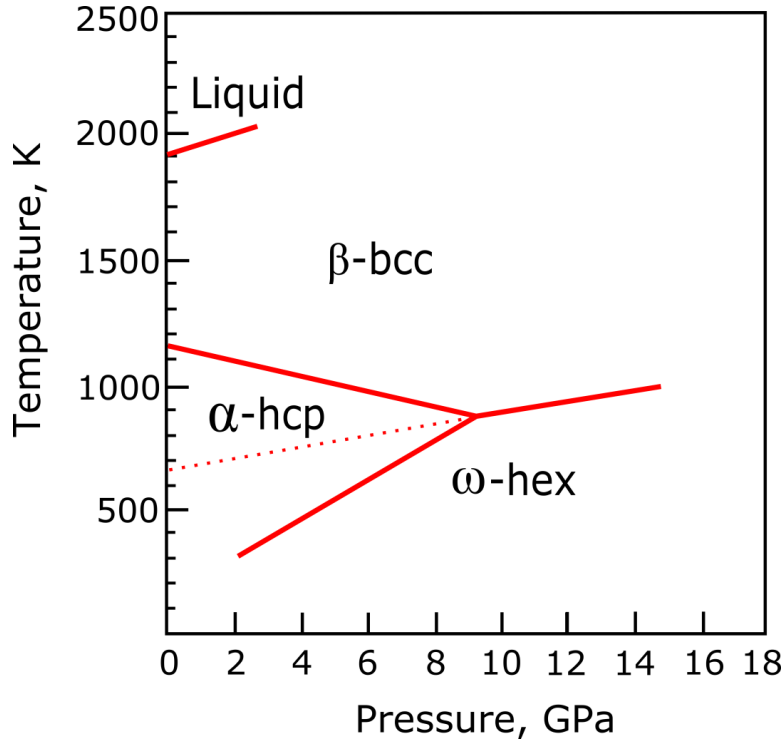
Fig. 2.1: The pressure (P) – temperature (T) phase diagram of pure Titanium [14,19,20].

For the multicomponent Ti-alloys, the quantification of α-and β-stabilizing elements are estimated by $[Al]_{eq}$ and $[Mo]_{eq}$ [14], respectively from the expressions given below:

$$[Al]_{eq} = [Al] + [Zr]/3 + [Sn]/3 + 10[O] \tag{2.1}$$

$$[Mo]_{eq} = [Mo] + [Ta]/5 + [Nb]/3.6 + [W]/2.5 + [V]/1.25 + 1.25 [Cr] + 1.25 [Ni] + 1.7 [Mn] + 1.7 [Co] + 2.5 [Fe] \tag{2.2}$$

Although Zr and Sn belong to α-stabilizers, the effect towards phase transformation temperature is very little and so sometimes referred to as neutral elements.

In the **Ti–Nb equilibrium phase diagram** three phases (liquid L, bcc β, and hcp α) exist as shown in **Fig. 2.2**. Here it is important to mention that the equilibrium phase diagram is constructed [28] using regular solution model of Gibb's free energy by method of CALPHAD. Because of the low diffusion rates at temperatures below 600°C, there is a lack of experimental data for an accurate experimental assessment of the phase diagram. For an example, diffusion coefficient at 500°C decreases by eight orders of magnitude from 20 to 70 at.% Nb. It indicates that if the equilibrium is achieved at 20 at.% Nb is 3 s at 500°C, it would take almost 10 years to reach the equilibrium in the case of 70 at.% Nb alloy [21]. It is also very difficult to achieve the β/ (β+α) phase boundary experimentally. This is confirmed by the following experiments:(i) the quenching experiments from the β-phase for Nb content greater than 28 at.% the β-structure persists in the alloys [28–30] and (ii) the ageing experiments at 500°C for 5 months in 50, 60, and 70 at.% Nb alloys does not even yield any α-precipitates, only β-phase was observed [21]. The maximum solubility of Nb in α-Ti–Nb is estimated as 2.5 $\pm$ 0.5 at.% Nb at the temperature range between 600 and 650°C.

There are three **metastable phases** which occur in the Ti–Nb binary system: two are of martensitic types (α'-hcp and α"-orthorhombic) formed during rapid quenching from β-phase in Ti-rich alloys and another is the ω-hexagonal phase, see **Fig. 2.3**. Alloys with relatively low Nb content ($\leq$ 7.2 at.% i.e. 13.3 wt.% [7,31,32]) favors the formation of the α'-martensite while for an Nb content larger than 7.2 at.% the α"-martensitic phase forms and persists up to the concentration as high as 25.5 at.% Nb i.e. 40.4 wt.% [28,32] upon rapid quenching. As the martensitic start temperature M_s-curve is below the ω-start curve Ω_s (here it is assumed that Ω_s coincides with $T_0^{\beta \to \omega}$ curve) between 14.3 and 25.5 at. % Nb, the α"-martensite forms if rapidly quenched and ω-phase will form if slowly quenched [21] (see **Fig. 2.3**).

Quenched alloys in the range of 25.5 to 42.7 at.% Nb may contain the ω-phase. However, the experimental evidences by TEM observations shows sharp ω-reflections in alloys containing 18 to 25 at.% Nb [28,30] and then the concentrations up to 42.7 at% Nb weak diffuse reflections and streaking corresponding to ω-phase are seen [32]. The type of ω-phase is formed by slow quenching (0.3 to 3°C/s [32]), called as athermal ω. The ω-phase can form also during an ageing experiments in the quenched alloys (see the marked region in **Fig. 2.4**) at a temperature of $\leq$ 425°C by spinodal decomposition of the β-phase, regarded as isothermal ω [21,32]. However, ageing experiments carried out at a temperature > 425°C result in α-precipitates forming in the β-matrix. Alloys with a Nb content exceeding 42.7 at.% Nb only exist in the single β-phase.
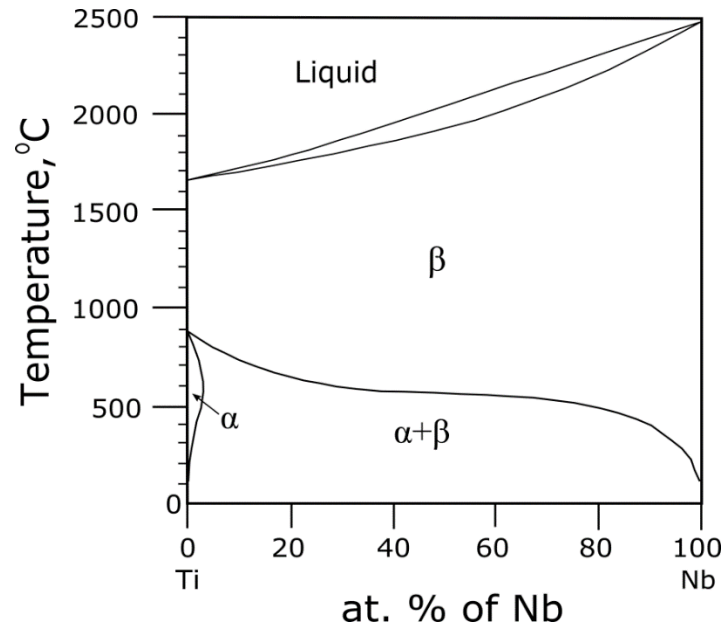
Fig. 2.2: The calculated Ti–Nb equilibrium phase diagram [28]. *The experimental β/(β+α) phase boundary matches with that of calculation above 600°C.*
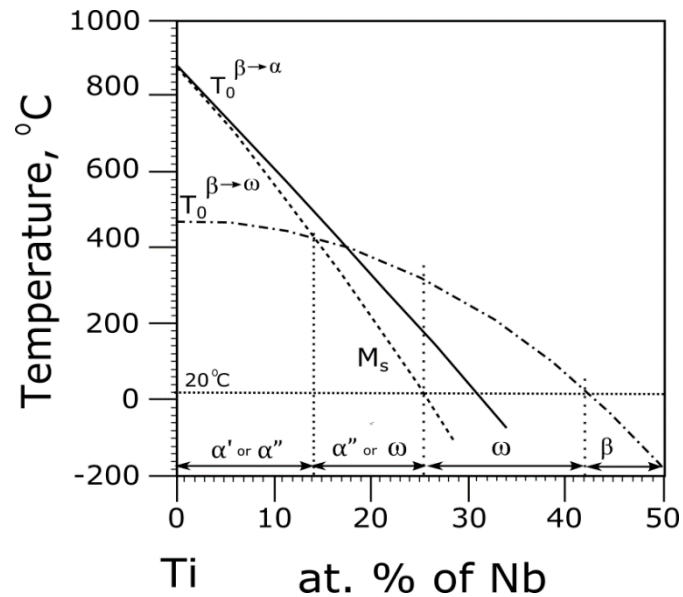
Fig. 2.3: The calculated T_0 curves and experimental M_s curve, adopted from [21].
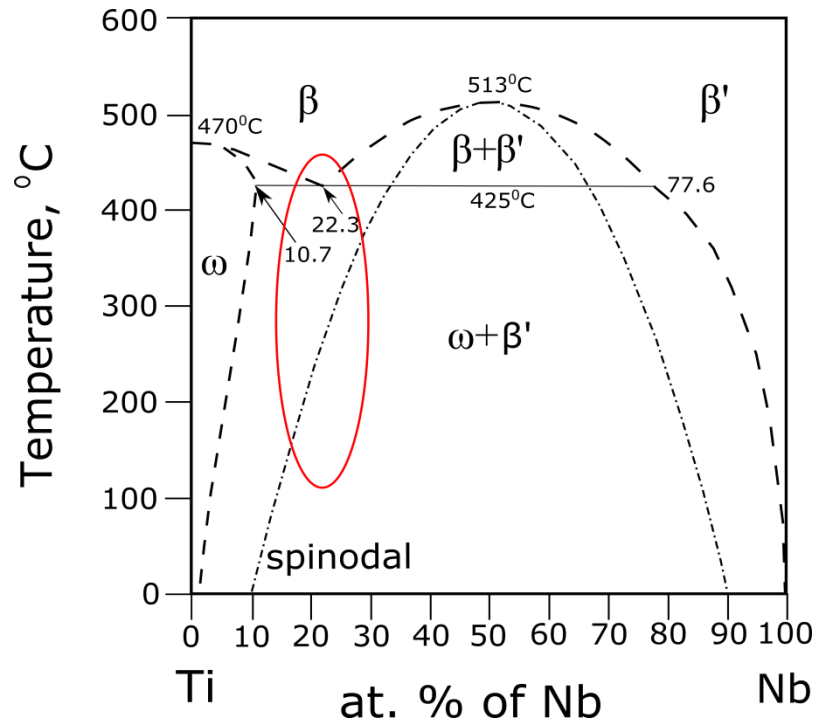
Fig. 2.4: The calculated metastable ω/β-phase diagram [21]. *Marked region (red) corresponds to the ageing experiments for the range of composition.*

The formation of phases can be classified into two types: reconstructive and displacive. The former type involves the breakage of the atomic bonds and reestablishing a new configuration from the previous one. This requires atomic diffusion process to occur. On the other hand, transformations of the displacive type involve only small atomic movements (typically only a fraction of the interatomic distances) to yield structural changes without the need of long range diffusion. Martensitic phase transformations are of the displacive type showing co-operative, military-like movements of the atoms to. A martensitic phase transformation that does not require a thermally activated atomic motion is denoted athermal and cannot be suppressed by rapid quenching [14]. In the Ti–Nb system, depending on the Nb content two types of martensitic structures form (α' and α"). Also athermal ω-phase forms by a displacive mechanism (see **Fig. 2.3).** The isothermal ω- and α-phase may form as precipitation products from the β-phase depending on the temperature and isothermal holding time; following a reconstructive mechanism (see **Fig. 2.4).**

2.1.3. Crystallography and orientation relationship between phases

2.1.3.1. The β-phase

The high temperature phase of Ti–Nb is the β-phase that has a bcc lattice structure (space group = Im-3m, Wyckoff position = 2a) containing two atoms in a unit cell with atomic positions at (0, 0, 0) and (½, ½, ½). With increasing concentration of Nb the β-phase becomes stable at room temperature. The alloys with Nb concentration beyond 25 at.% show the β-phase as the main phase [30,33]. The lattice parameters: a_β increases by 0.13×10^{-4} nm, with 1 at.% increase of Nb [34].

2.1.3.2. α'and α" lattice structures

For a martensitic phase transformation (being of the displacive type) the maintenance of coherency at the interface between the parent (the austenite) and product phase (the martensite) is an essential condition. In other words, the interface between parent and product should be the invariant i.e. undistorted and unrotated. For this the requirements [14,35] are:

    (i)   The lattice deformation or Bain strain causing the change in the lattice structure (for an example bcc to hcp) in a way that one of the principal strains would be zero; other two are positive and negative by equal amounts.

    (ii)   If the condition (i) is not met, a lattice invariant shear (LIS) by slip or twin in the product of step (i), provides the undistorted (but not necessarily atomically flat) habit plane. When LIS is provided by slip the martensite plate contains only single variant of martensitic crystal while twinning yields a laminate of two twin related variants in a single martensitic plate.

A rigid body rotation is required to ensure the undistorted habit plane is unrotated.

To estimate the Bain strain, the lattice correspondence between parent and martensitic phases is important to know. The correct choice is made by selecting the one which involves the less strain and minimum rotation.

The lattice (Bain) deformation B is given by

$$B = \begin{bmatrix} n_1 & 0 & 0 \\ 0 & n_2 & 0 \\ 0 & 0 & n_3 \end{bmatrix} \qquad (2.3)$$

β → α′ transformation

The structure of α′ is hexagonal closed packed hcp (space group = P6$_3$/mmc, Wyckoff position 2c [36]) is similar to that of α. The unit cell contains 2 atoms with atomic positions (0,0,0) and (½, ½, ½). The lattice parameters are almost identical to that of pure Ti [32] and influenced slightly by addition of Nb [7]. The lattice correspondence between bcc and hcp structure was first purposed by Burgers [37]. He purposed that the basal plane {0001} of α-phase can be constructed out of a {110}$_\beta$ plane. Close packed directions in this plane (i.e. $[1\bar{1}1]_\beta$ and $[\bar{1}1\bar{1}]_\beta$ for the (110)$_\beta$ plane) correspond to two of the hcp close packed vectors of the type $<11\bar{2}0>_\alpha$. The third $<11\bar{2}0>_\alpha$ close packed direction is derived from a $<100>_\beta$ direction (see **Fig. 2.5**).

So the lattice orientation relationship between the β- and the α/α′ -phase is

$$(0001)_\alpha \parallel (110)_\beta$$

$$[11\bar{2}0]_\alpha \parallel [1\bar{1}1]_\beta$$

The principal lattice strains for the β→α′ transformation are:

for one variant:
$$n_1 = \sqrt{\frac{3}{2}} \left(\frac{a_\alpha}{a_\beta} \right) \tag{2.4}$$

$$n_2 = \frac{a_\alpha}{a_\beta} \tag{2.5}$$

$$n_3 = \frac{1}{2} \left(\frac{c_\alpha}{a_\beta} \right) \tag{2.6}$$

Substituting the lattice parameters for pure Ti shows that the lattice strains n_1, n_2, and n_3 are approximately 1% tensile, 11% tensile, and 11% compression, respectively.

β→α″ transformation

The structure of the α″-phase is C-centered orthorhombic (space group = Cmcm, Wyckoff position 4c [38,39]). its conventional unit cell contains four atoms with atomic positions (0, y, ¼), (0, -y, ¾), (½, ½+y, ¼), (½, ½-y, ¾), where y is the position of atoms on a (002) plane along a [010] direction (**Fig. 2.6**, for a clear graphical visibility the origin has been shifted by (0, y, ¼)[40]). The α″ structure may be viewed as a transition between the hcp and bcc structures. By adjusting y, b and c all the three structures can be produced. For example a hcp structure can be obtained when y = 1/6 and b/a = $\sqrt{3}$ and a bcc structure can be constructed when y = 1/4 and b/a = c/a = $\sqrt{2}$ (see **Fig. 2.6**). Therefore, the lower limit of y

value for α"-phase is 0.1666 and the upper limit 0.25. In Ti–Nb cases, this value has been estimated to be around 0.18–0.21 depending on composition [7,41]. The lattice parameters: $a_{\alpha"}$ increases by 1.364×10^{-3} nm, $b_{\alpha"}$ decreases by 1.564×10^{-3} nm and $c_{\alpha"}$ decreases by 0.238×10^{-3} nm with 1 at.% increase of Nb [34]. The lattice correspondence arising by the transformation of β→α" can be expressed as follows (see **Fig. 2.6**):

$$[100]_{\alpha"} \; || \; [100]_{\beta}$$

$$[010]_{\alpha"} \; || \; [011]_{\beta}$$

$$[001]_{\alpha"} \; || \; [0\overline{1}1]_{\beta}$$

The principal lattice strains for the β→α" transformation are:

for one variant:
$$n_1 = \frac{a_{\alpha"}}{a_{\beta}} \tag{2.7}$$

$$n_2 = \frac{b_{\alpha"}}{\sqrt{2}a_{\beta}} \tag{2.8}$$

$$n_3 = \frac{c_{\alpha"}}{\sqrt{2}a_{\beta}} \tag{2.9}$$

2.1.3.3. The ω-phase and its formation

The ω-phase is a metastable phase that can be generated through application of a a hydrostatic pressure to the α-phase in Ti alloys with low β-stabilizer content. In the case of pure Ti, the pressure is in the range of 3–9 GPa [16–18,42]). With increasing the content of β-stabilizing elements the ω-start pressure (defined as the pressure necessary to nucleate the ω-phase) rises substantially [43,44]. Therefore relatively high pressure is required to induce the ω-phase from the β-phase [19,44–47]. When the material is processed by the shear deformation in addition to a superimposed hydrostatic pressure it reduces the value of the ω-start pressure. On the other hand, athermal and isothermal ω-phase can be formed during heat treatments; by quenching and isothermal holding (ageing experiments) of β-phase alloys, respectively. The number density of athermal ω-phase precipitates is generally extremely large which suggest the precipitates are very fine (because of no involvement of long range diffusion processes). In the isothermal case, the ω-precipitates formed by a spinodal decomposition mechanism are rather large and can be of ellipsoidal or cuboidal shapes [48,49] depending on the lattice misfit. When the solute is a 4d transition metal such as Nb or Mo the lattice misfit is very small leading to ellipsoidal shape. When the solute

element is a 3d transition metals (like V, Cr or Mn), a relatively large misfit occurs which leads to formation of cuboidal morphology of ω-phase.

The structure of ω-phase is hexagonal (space group = P6/mmm, Wyckoff positions = 1a, 2d [19]). This unit cell contains three atoms with atomic positions (0, 0, 0), (2/3, 1/3, 1/2), and (1/3, 2/3, 1/2). The formation of the ω-phase transformation from α and β can be understood considering the lattice correspondence between these phases. This is outlined in the following.

β→ω transformation

The formation of the ω-phase from the β-phase can be explained by a $(111)_\beta$ plane collapse model [50–52] i.e. the unit cell of the ω-phase can be created by collapsing two of every three $(111)_\beta$ planes in the [111] direction to an intermediate position, retaining the others unaffected, as shown in **Fig. 2.7**. When the collapse is complete, the ideal hexagonal ω-phase forms showing a six-fold rotation symmetry and when it is incomplete the lattice structure exhibits trigonal structure (space group = P-3m1). Based on the lattice correspondence the lattice parameters of the ω-phase can be expressed in terms of the bcc lattice parameter: $a_\omega = \sqrt{2}a_\beta$, $c_\omega = \sqrt{3}a_\beta/2$.

The orientation relationships between β and ω phases can be expressed as

$$(111)_\beta \,||\, (0001)_\omega$$

$$[1\bar{1}0]_\beta \,||\, [2\bar{1}\bar{1}0]_\omega$$

Since there are four possible sets of <111> directions there are four crystallographic variants of the ω-structures present in a bcc crystal.

α→ω transformation

Two distinct lattice orientation relationships between the α and ω-phases were reported in the literature based on the several diffraction experiments [18,19,46,53–55].

Orientation Relation I (OR I)

$$(0001)_\alpha \ || \ (11\bar{2}0)_\omega \text{ and } [11\bar{2}0]_\alpha \ || \ [0001]_\omega$$

Orientation Relation I (OR II)

$$(0001)_\alpha \ || \ (01\bar{1}0)_\omega \text{ and } [11\bar{2}0]_\alpha \ || \ [1\bar{1}01]_\omega$$

These two orientation relationships imply to two distinct mechanisms of the phase transformation involving a direct α → ω route and a two stage α→β→ω route. Silcock [53] was the first to propose the transformation from α to ω-phase based involving OR I, shown in **Fig. 2.8** [19]. It involves generation of $(11\bar{2}0)_\omega$ plane from the $(0001)_\alpha$ plane by displacement of alternate hexagons on $(0001)_\alpha$ plane by 0.148 nm (the atoms marked a, b, c and d shift to a', b', c' d'). In addition a contraction of ~4.7% along $[11\text{-}20]_\alpha$ and an expansion of ~4.5% along the $[1\text{-}100]_\alpha$ are necessary for generation of a ω-unit cell. The two stage transformation involving α→β→ω route was first proposed by Usikov et al. [18] based on orientational relationship (OR II). Later this route was also reported by Vohra et al [46] while investigating the high pressure experiments on various concentration of solute atom V in the case Ti–V alloys. It is concluded that addition of V atoms is responsible for retention of intermediate β-phase.

The orientation relationships for this transformation [19]:

   Variant I: $(0001)_\alpha \ || \ (011)_\beta \ || \ (11\bar{2}0)_\omega \text{ and } [11\bar{2}0]_\alpha \ || \ [11\bar{1}]_\beta \ || \ [0001]_\omega$

   Variant II: $(0001)_\alpha \ || \ (110)_\beta \ || \ (01\bar{1}1)_\omega \text{ and } [10\bar{1}0]_\alpha \ || \ [\bar{1}11]_\beta \ || \ [\bar{1}011]_\omega$
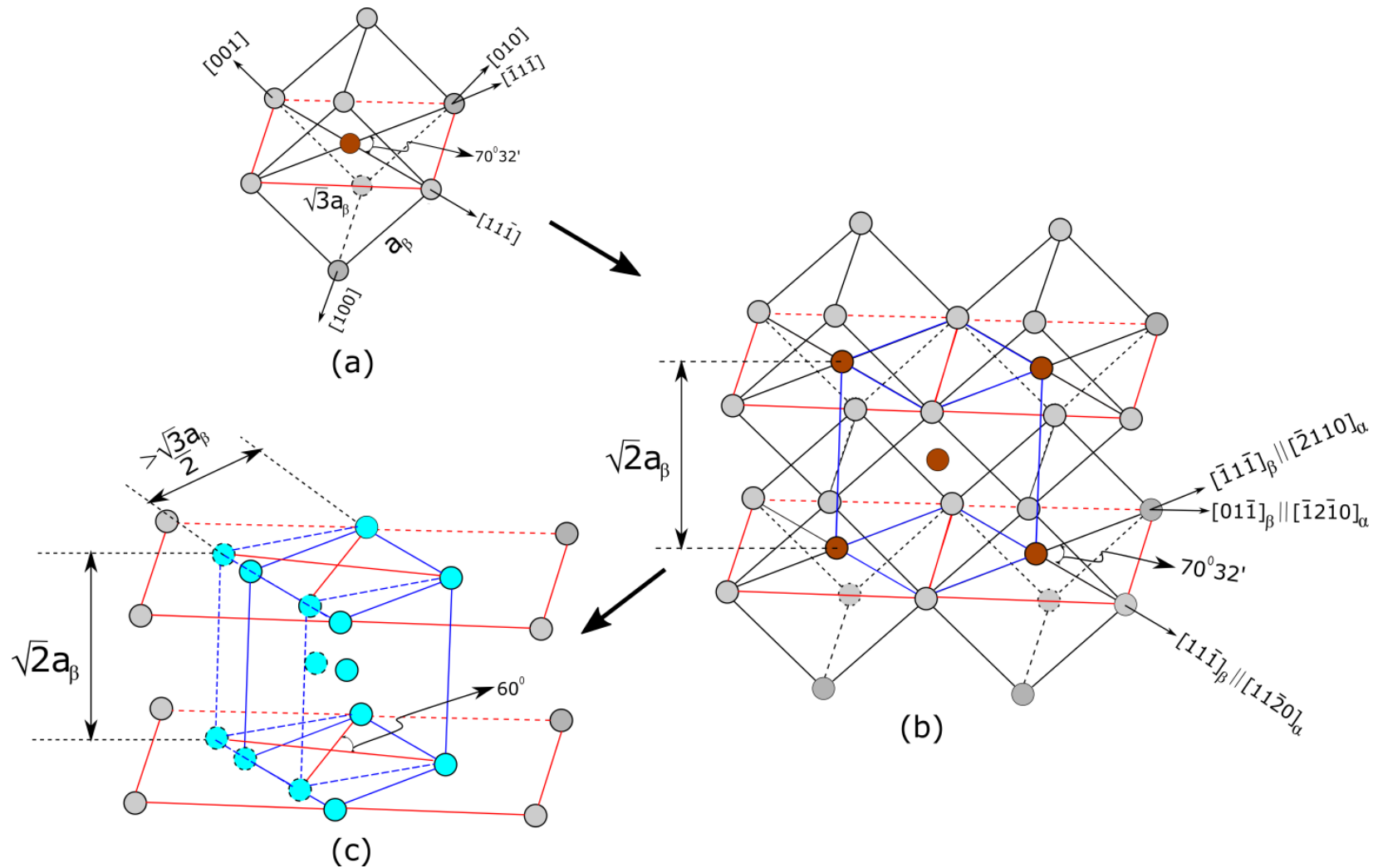
Fig. 2.5: The orientational relationships for β→α transformation: (a) bcc β-phase structure highlighting most close packed plane, (b) distorted hcp α-phase (lattice parameters: cα =√2aβ and aα =√3/2 (aβ), cα/aα = 1.633) constructed from bcc phase, and (c) one unit cell of α-phase (cα =√2aβ and aα >√3/2 (aβ), cα/aα < 1.633).
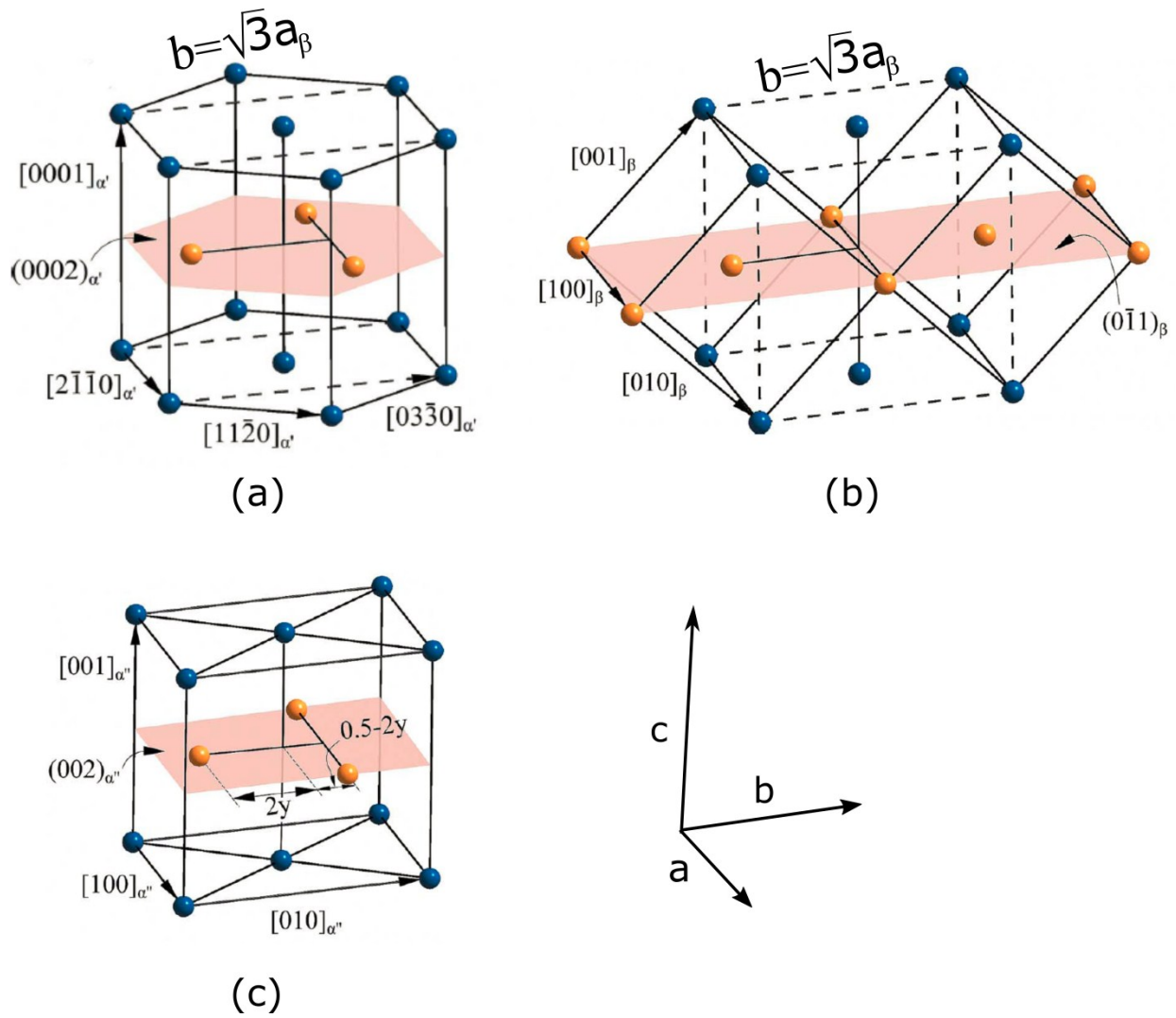
Fig. 2.6: Representation of Orthorhombic lattice structure: (a) as formed from the HCP lattice structure, (b) as formed from bcc unit cells, and (c) one unit cell of orthorhombic α"-martensite; the y indicates the position of atoms on $(002)_{\alpha"}$ plane in $[010]_{\alpha"}$ direction. For better visibility the origin has been shifted by (0, y, ¼) [7].
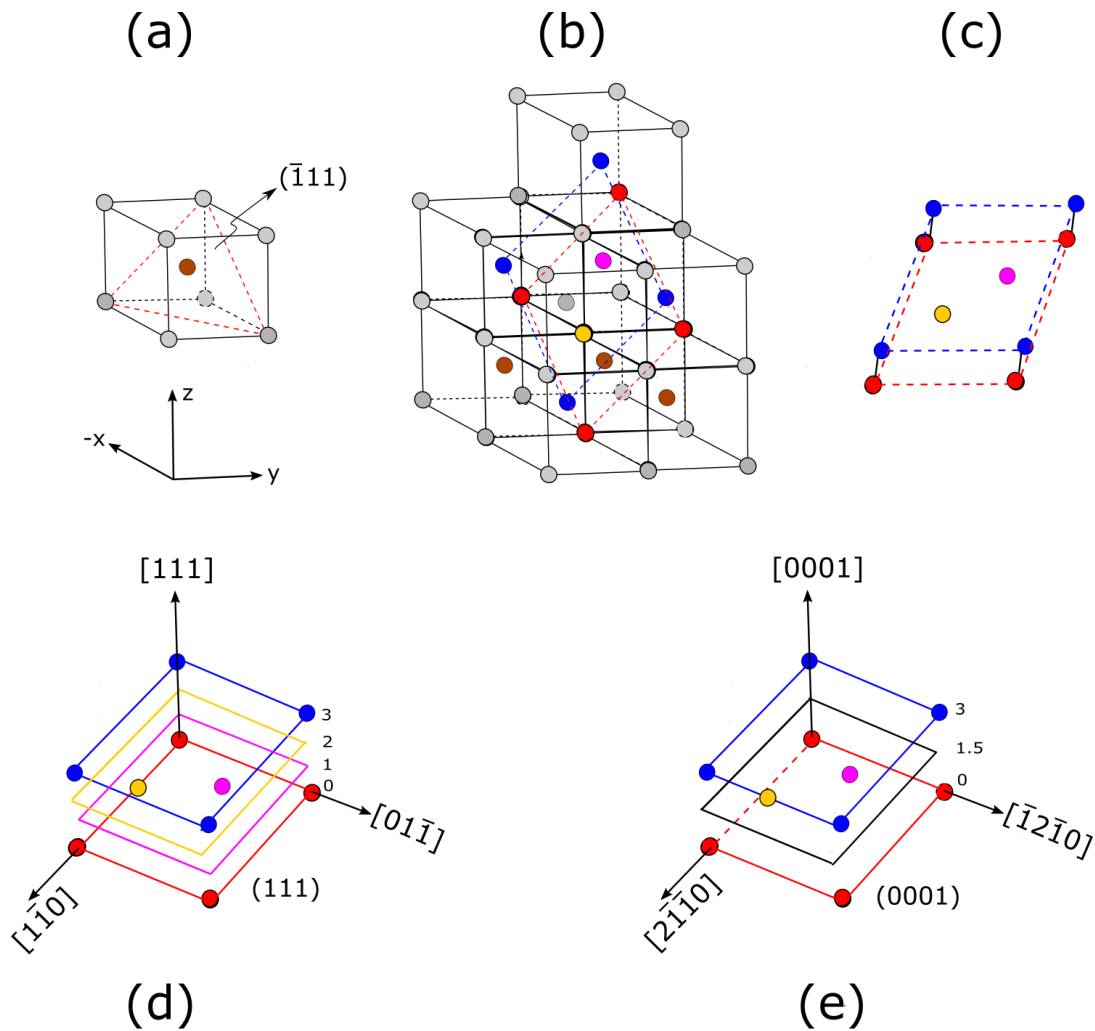
Fig. 2.7: The β-bcc to ω-hexagonal phase transition in steps: (a) bcc lattice structure, (b) and (c) show stacking of (111) planes in 3D space, (for visibility it is rotated in (c)), (d) bcc unit cell showing stacking of (111) planes in [111] direction, with the position of the planes indicated as 0,1,2,3; (e) ideal hexagonal ω-unit cell showing complete collapse of the planes of 1 and 2 to the intermediate position of 1.5. The lattice parameters of hexagonal ω-phase are related to that of bcc β phase as $a_\omega = \sqrt{2}a_\beta$, $c_\omega = \sqrt{3}a_\beta/2$.
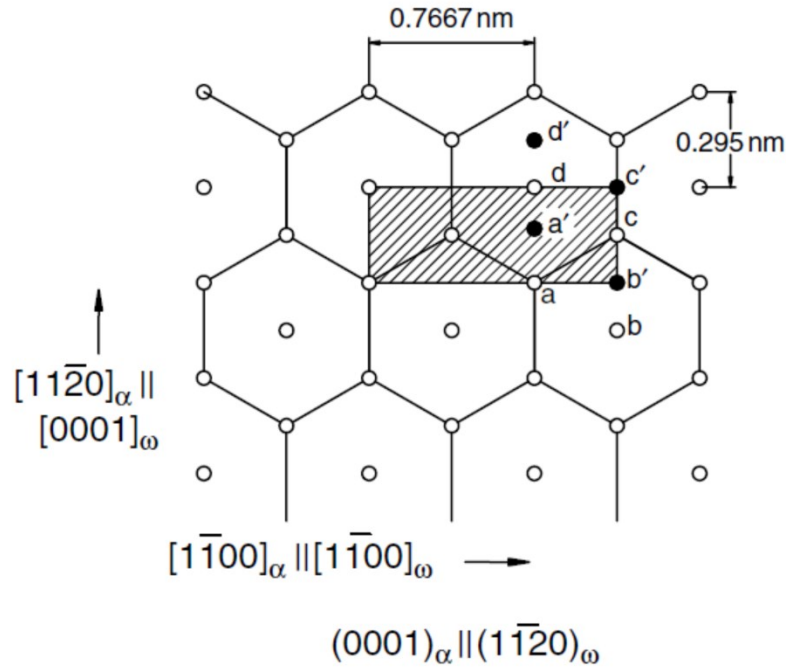
Fig. 2.8: The lattice correspondence between α and ω-phases [19]. *The atoms shift from positions of a, b, c and d on the (0001)α plane, to those of a', b', c', d' to form (11-20)ω plane. The contraction along [11-20]α and an expansion along [1-100]α are required to generate the ω-unit cell.*

2.1.4. Mechanical properties and applications of Ti–Nb based alloys

Exploiting different phases existing in the stable and metastable phase diagrams through proper selection of heat treatments and mechanical processing it is possible to control the mechanical properties owing to different microstructures and dislocation densities. In particular the mechanical properties such as Young's modulus E and the mechanical strength H are of interest while considering the material for biomedical applications in addition to excellent biocompatibility [11,56–59] and high corrosion resistance [10–13,60]. The E of the alloy close to that of human bone (E = 4–30 GPa depending on the type of the bone and direction of measurement [6,61]) is an important criterion since this facilities the easy stress transfer between human bone and implant (i.e. minimization of stress shielding effect [5]) which is required for the bone cells to be alive near to the implant. The Young's moduli of different orthopaedic alloys are summarized in **Fig. 2.9**.

Currently Pure Ti and Ti–6Al–4V (Ti64, $\alpha+\beta$-microstructure) are the most commercially used orthopaedics in biomedical applications (see **Fig. 2.10**). Although their E values (E_{Ti64} = 110 GPa and E_{Ti} = 100 GPa [6,10]) are far less than other biomaterials such as stainless steel (E = 206 GPa [10]) and Co–Cr based alloys (E = 240 GPa [10]), these values are still about 3 to 4 times higher than that of human bone. Therefore, there is a necessity of a search of novel materials with even lower modulus.

Recently β-Ti alloys [8,34,62–73] containing high concentration of β-stabilizing elements have received increased attention because of lower Young's modulus (most materials falls in the range of E = 55–85 GPa [10]). This low value of E in β-bcc metals and alloys is mainly the cause of an anomalously low value of C'= ($C_{11}-C_{12}$)/2 which corresponds to the shear modulus associated with a shear deformation occurring on a {110} plane in a $<\bar{1}10>$ direction [62,74] (see **Table 2.1**, C_{11}, C_{12} and C_{44} are the elastic constants of the bcc lattice structure). In other words, a bcc lattice structure shows a rather low resistance with respect to a {110} $<\bar{1}10>$ shear deformation since, to a first approximation, this shear does not change the distance between next nearest atoms. Also the bcc structure shows a relatively low value of the shear modulus C_{44} (corresponding to a shear deformation on a {100} along a <001> direction) with respect to that of fcc lattice systems (see **Table 2.1**). The value of C' is also related to the phase stability of bcc lattice structure and depends on e/a ratio (e/a denotes the number of valence electrons per atom and depends on the outer d + s orbital electrons in a free atom configuration), C' becomes a very value when the e/a ratio is in the range of 4.20–4.24 [75].

Knowing the elastic constants C_{ij}, the Young's modulus E and the shear modulus G of a polycrystalline cubic material can be calculated e.g.. by using the Voigt approximation [76] corresponding to the upper limit of the values E and G. This is expressed as:

$$E = \frac{(C_{11} - C_{12} + 3C_{44})(C_{11} + 2C_{12})}{2C_{11} + 3C_{12} + C_{44}} \quad \text{and} \quad G = \frac{C_{11} - C_{12} + 3C_{44}}{5} \quad (2.10)$$
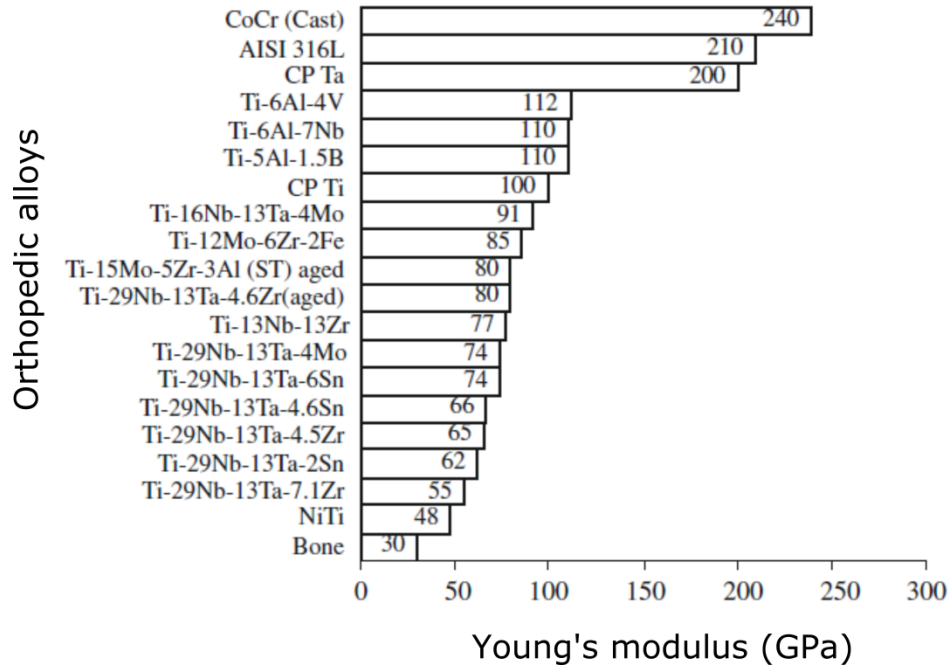
Fig. 2.9: The Young's moduli of various orthopaedic alloys [6].

Table 2.1: Comparison of C', C_{44} and anisotropy factor $A = C_{44}/C'$ for cubic systems.

Material [at.%]	C' (GPa)	C₄₄ (GPa)	A
Ti–22Nb–6Ta [62]	8	21.3	2.7
Ti–30Nb [9]	13.7	33.1	2.3
Ti–23Nb–0.7Ta–2Zr–1.2O [77]	16.0	28.0	1.7
Ti–Ni [62]	17–19	35–39	2
Ni–Al [78]	14.6	132	9
Ni [62]	49.6	124.7	2.5
Fe [62]	47.8	112	2.3
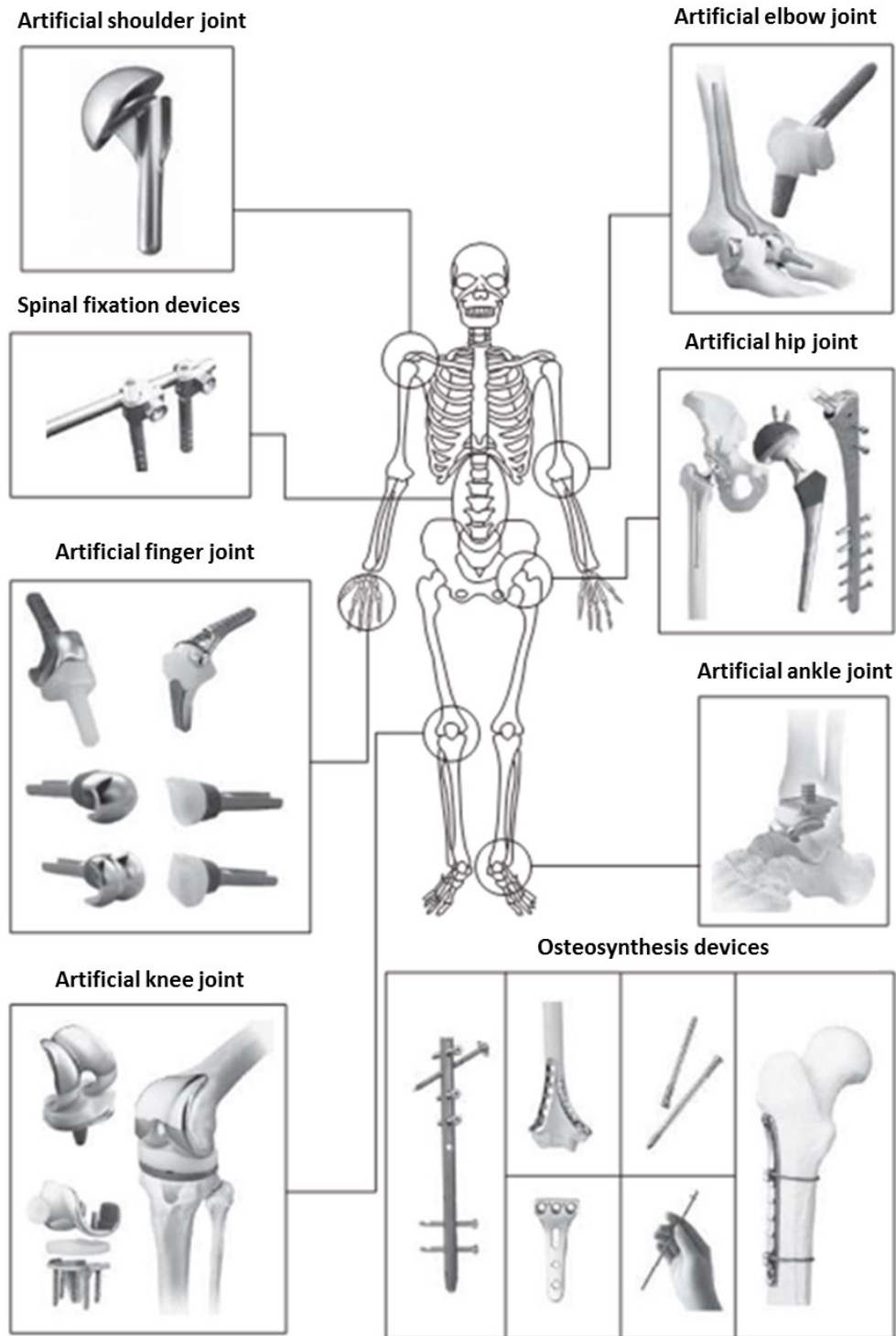
Fig. 2.10: The implants that are used for in-vivo orthopaedic surgery and dentistry [79].

In the case of Ti–Nb, studies on quenched alloys show that E and G strongly depend on the Nb content following a W shaped curve having two local minima at about 15 wt.% (~8 at.%) and 42.5 wt.% (~27 at.%) Nb (see **Fig. 2.11**). These minima correspond to Ti–Nb alloys with containing α"-orthorhombic martensite and the β-bcc phase, respectively [8,80]. The highest values of E and G are observed for the alloy containing about 30 wt.% (~18 at.%)of Nb. This is attributed to the formation of athermal ω-phase (high modulus phase) along with α" phase during quenching [80]. Further increase of the Nb content up to 42.5 wt.% Nb shows a drop in values due to increasing volume fraction of β-phase, despite of the fact that isothermal ω-phase forms during ageing [29]. Beyond 47 wt.% of Nb there is increase of the moduli with increasing Nb content approaching the values of pure Nb (E =104 GPa, G = 38 GPa) [30]. The single ω-phase in bulk form is obtained only either under high pressure [43,44] or during severe plastic deformation [31] but never achieved in bulk form under ambient pressure during heat treatments. The E value for the bulk ω-phase has been reported to be about 130 GPa [25,31]. The value of E for single crystalline β-Ti–45.0 wt.% Nb is about 65 GPa [9]. In the case of Ti–Nb alloys containing single α" and α' phase in bulk forms the values of E are ~65 [8,31] and ~97 GPa [31]. The E values for different phases can be summarized as $E_\omega > E_{\alpha'} > E_{\alpha''} > E_\beta$ [4].

In the case of Ti–Nb, studies on quenched alloys show the E and G dependence over Nb content follow a W shaped curve having two local minima at 15 wt.% (~8 at.%) and 42.5 wt.% (~27 at.%) Nb (see **Fig. 2.11**) corresponding to α"-orthorhombic martensitic and β-bcc phase, respectively [8,80]. The highest values of E and G are observed for the alloy containing 30 wt.% (~18 at.%)of Nb attributed to the formation of athermal ω-phase (high modulus phase) along with α" phase during quenching [80]. Further increasing of Nb content up to 42.5 wt.% Nb show a drop in values due to increasing volume fraction of β-phase, despite of the fact that isothermal ω-phase forms during ageing [29]. Beyond 47 wt.% of Nb, moduli increase and approach towards to the values of pure Nb (E =104 GPa, G = 38 GPa) [30]. This behavior of moduli is both function of present phases and potential gradients between atoms. The single ω-phase in bulk form is obtained only either under high pressure [43,44] or during severe deformations [31] but never achieved in bulk form under ambient pressure during heat treatments. The E value for the bulk ω-phase has been reported to be about 130 GPa [25,31]. The value of E for single crystalline β- Ti–45.0 wt.% Nb is about 65 GPa [9]. In the case of Ti–Nb alloys containing single α" and α' phase in bulk forms the values of E are ~65 [8,31] and ~97 GPa [31]. The E values for different phases can be summarized as $E_\omega > E_{\alpha'} > E_{\alpha''} > E_\beta$ [4].
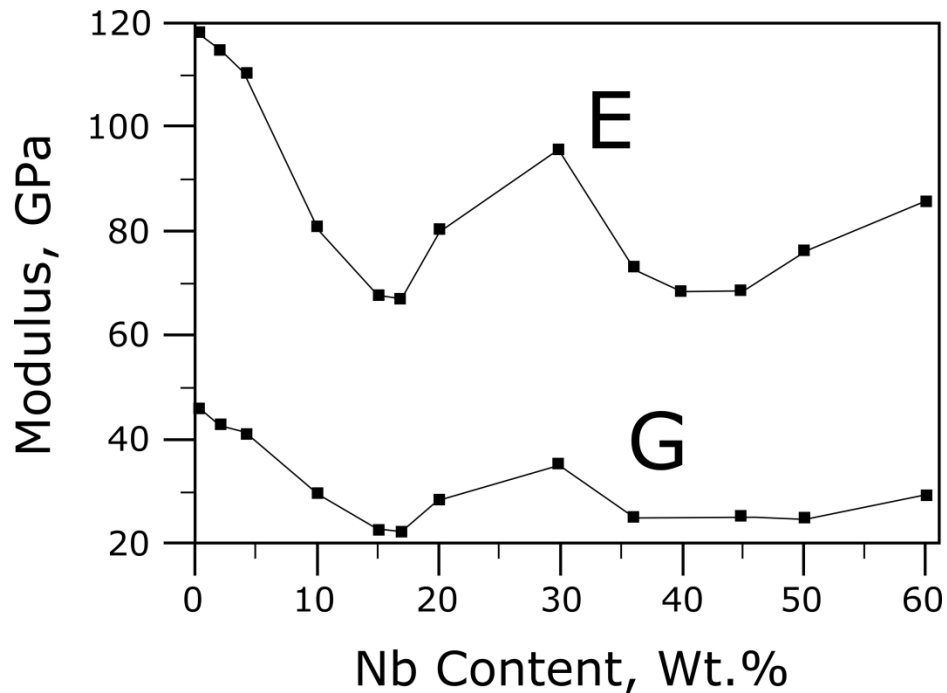
Fig. 2.11 Compositional dependence of the Young's modulus (E) and shear modulus (G) [8,80,81] *of Ti–Nb.*

Another important aspect while considering the material for orthopaedics is the high strength in combination with low E. The mechanical strength H of α"-Ti–Nb, β-Ti–Nb (both showing a low value of E = ~65 GPa, see **Fig. 2.11**), Ti–13Nb–13Zr (E =77 GPa [6]) alloys are less than conventional biomaterials such as stainless steel (H = 2.0 GPa [82]), Co–Cr based alloy (H = 3.2 GPa [83]), pure Ti (H = 1.5 GPa [71]) and Ti–64 (H = 3.3 GPa [10,84]), etc. Therefore a method should be developed to enhance the strength without increasing the value of E. The strength β-type Ti–Nb alloys can be enhanced by the ageing treatment [49,85]. However, this is frequently associated with formation of fine precipitates of isothermal ω-phase causing increase of the Young's modulus [29,49,86]. On the other hand, processing metals and alloys through severe plastic deformation (SPD) is well known to enhance mechanical properties [1,2,87,88]; especially strength which can be substantially increased by grain refinement due to the Hall-Petch relation and introduction of a high density of defects while maintaining the Young's modulus unless there is SPD induced change of the lattice structure. An overview of the mechanical properties in relation to SPD on Ti and Ti–Nb based alloys are presented in the **section 2.2.4.**

2.2. Nanostructured materials by Severe Plastic Deformation

2.2.1. Synthesis of Ultrafine–grained and Nanocrystalline Materials

The control over the microstructure and grain size offers a pathway to design the materials for specific properties. In particular grain sizes in the range 100 nm–1µm (ultrafine-grained materials) and smaller than 100 nm (nanocrystalline materials) can show an excellent combination of physical and mechanical properties compared to their coarse grained counterparts.

Obtaining ultrafine/nano-grained materials in the bulk has been a subject of great interest for a long time. In general, there exist two complementary approaches to obtain such a material denoted as "bottom-up" and "top-down". The bottom-up approach starts with individual atoms/molecules as building blocks and assembles them to form bulk material [89,90]. It includes techniques such as inert gas condensation [91], physical vapor deposition [91], electro-deposition [92], etc. In the case of top-down approach, grain refinement occurs through successively breaking up the coarse-grained structure of bulk materials into smaller grains using corresponding effects of severe plastic straining. This approach is represented best by the so called "SPD" (=Severe Plastic Deformation) techniques.

2.2.2. Severe Plastic Deformation

According to the literature [1–3], Severe plastic deformation – SPD is defined as a materials forming process in which exceptionally large strains can be imposed to the bulk sample without a significant change in overall dimension of the work piece [93]. The deformation is maintained because of the permanent application of an hydrostatic pressure of about 1 GPa or more which prevents from the formation of cracks. The hydrostatic pressure also favours the storage of lattice defects [94] especially of dislocations most of which arrange as new grain boundaries thus achieving an ultrafine grained or even nanocrystalline structure.

There exist different SPD techniques, like high-pressure torsion (HPT) [95–97], Equal channel angular pressing (ECAP) [98,99], rolling and folding (R&F, a modified form of accumulative roll bonding [100,101]), hydrostatic extrusion (HE) [102], and others.

2.2.2.1. High-Pressure Torsion

The concept of plastic deformation by combination of torsion and pressure was first proposed by Bridgman [95]. In the nineties, it has been modified to achieve HPT under mostly hydrostatic pressure as this method is used for current state-of-the-art research (see **Fig. 2.12**) [2,96,97]. In HPT, a disc shaped specimen is held between cavities of two anvils and strained under torsion in addition to a high hydrostatic pressure (typically in the range of 4-10 GPa). In a first approximation, the deformation can be considered as a simple shear. For a successful HPT experiment, sufficient friction between the sample and anvil surfaces has to be maintained to avoid the sliding of the specimen during deformation. Therefore, some micro-roughness on both sides of the specimen and the cavities of anvils must be achieved by sand blasting. In an idealized case the thickness of the specimen should be constant throughout of the deformation (see **Fig. 2.12 (a)**). However, in real case (see **Fig. 2.12 (b)**) some amount of the material flows out of the cavities as the height of the sample is slightly higher than the combined depth of the cavities and thus the thickness of the specimen slightly gets reduced. The von Mises strain ε is given by the relation

$$\varepsilon = \frac{2\pi r N}{\sqrt{3} t_e}$$

(2.11)

where r, N and t_e are the radius of the sample, the number of rotations applied during the deformation, and the final thickness of the sample, respectively.
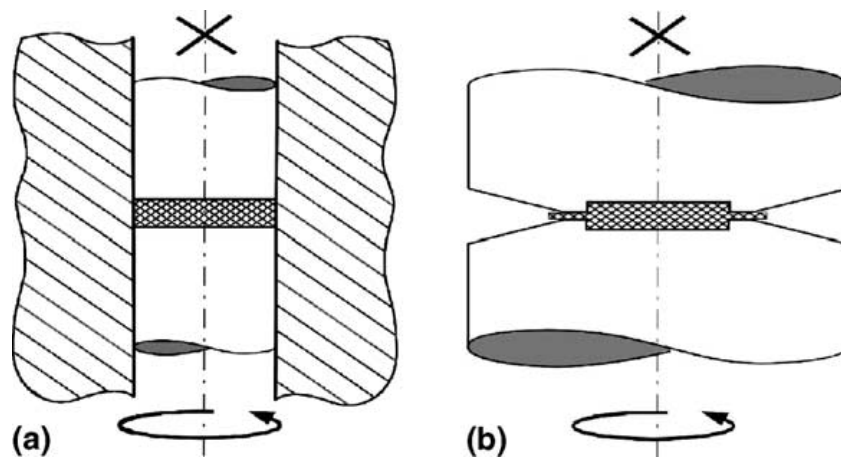
Fig. 2.12: Schematic of high-pressure torsion equipment: (a) Idealized and (b) practical set-up in current use [96].

2.2.2.2. Rolling and Folding

Rolling and folding (R&F) processes are often employed to produce bulk ultra-/nano-structured materials [103]. This is a slightly modified form of well-known ARB technique (accumulative roll bonding) [100] in which the stacking step in ARB is replaced by the folding step (see **Fig. 2.13**). At first the material is cold rolled to a desired thickness in multiple steps, then cut into two equal halves and folded one above another without any surface treatment and wire brushing (this step is an essential step in ARB). After that these folded strips are again subjected to rolling until the combined thickness reduced to half. The two strips of material join together by mechanical bonding during rolling. In principle this procedure can be repeated unlimitedly, so that a large amount of plastic strain can be applied to the material. Taking into consideration the von Mises yield criterion and assuming no lateral spreading of the rolled material, the von Mises strain ε can be expressed as follows [103]:

$$\varepsilon = \frac{2}{\sqrt{3}} \ln \left(\frac{t_0}{t_e}\right) \tag{2.12}$$

where t_0 and t_e are thickness of the material before and after rolling, respectively.
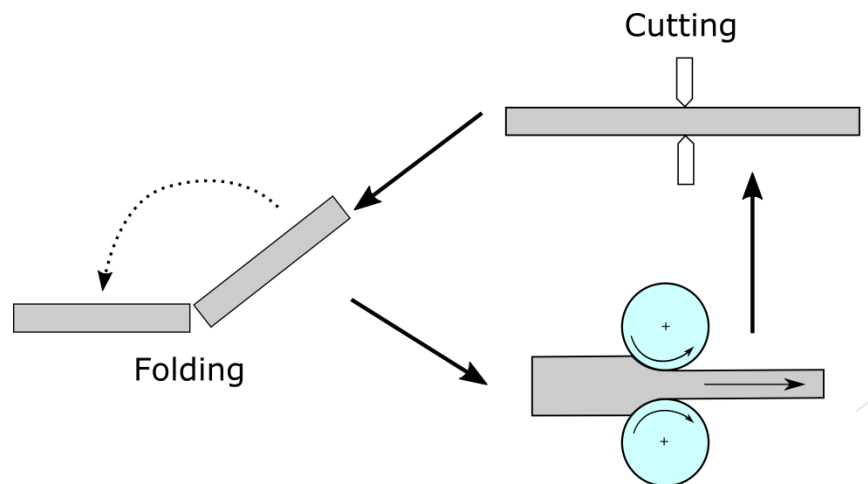
Fig. 2.13: Schematic of rolling and folding (R&F) process.

2.2.2.3. Hydrostatic extrusion

The method of hydrostatic extrusion (HE) was invented and patented by James Robertson [102]. The principle of HE process is depicted in **Fig. 2.14**. In this process the medium (e.g. oils, waxes, melted polymers, and molten glass) surrounds the work piece which is held in the sealed chamber. When the ram advances the medium is compressed and the hydrostatic pressure in the chamber builds up. When this pressure is sufficient enough the work piece starts to deform and extrudes out through the die. For HE, the von Mises strain ε is identical to true strain, can be calculated from the formula [102]:

$$\varepsilon = 2 \ln \left(\frac{D_s}{D_f} \right) \tag{2.13}$$

where D_s is the starting diameter and D_f is the final diameter of the work- piece.
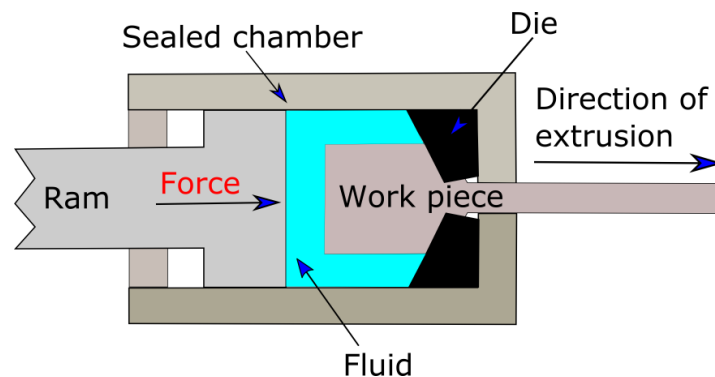
Fig. 2.14: Schematic of hydrostatic extrusion (HE) process, adopted from [104].

2.2.3. Stages of deformation and structural fragmentation during SPD

The hardening curves during deformation of the single crystals or polycrystalline samples must be represented by the resolved shear stress (τ) vs. ressolved shear strain (γ) curves. This way, the hardening effects arising from geometric and texture effects are eliminated. The τ and γ can be calculated for a polycrystal according to the relation $\tau = \sigma/<M>$ and $\gamma = \varepsilon<M>$, where σ is the true stress, ε = true strain and <M> is the average Taylor factor. For a non-textured polycrystalline fcc metal, M = 3.06 [105,106]. The hardening behavior of the material is the result of the increasing defect density e.g. dislocations and the grain refinement occurring during the deformation process. The accumulation of dislocations, their arrangements, and interactions along with the grain refinement in a polycrystalline

specimen exhibit a complex phenomenon as a consequence of grain-grain interaction caused by different material processing parameters like strain, strain rate, pressure, and temperature during a certain type of deformation process [107]. This refinement process can be framed via deformation induced dislocation boundaries [108–111] formed during different stages of the hardening curves.

The different stages of the hardening curve for a polycrystalline samples are clearly seen from **Fig. 2.15**. In this curve the stage I is not seen as this stage is limited to single slip activity in the single crystals. This stage is referred as the "easy glide regime". The onset of the stage II is caused by the activation of the secondary slip systems both in single and polycrystalline samples. The dislocations interaction leads to the linear work hardening [112]. The stage III also termed as "parabolic hardening stage" is characterized by the increase of the strength. However the rate of work hardening decreases due to the thermally activated cross-slip process of the screw dislocations which results the dynamic recovery [106]. The stage III is affected by the strain rate and temperature [113]. With strain during deformation the density of dislocations rises. These dislocations are not randomly stored in the microstructure; but assembled to form different kinds of dislocation boundaries. These boundaries subdivide an initial grain to sub-grains (cell-blocks) and ordinary dislocation cells. During stage II and III i.e. for small to medium strain ($\varepsilon = 0.06$–0.8), these boundaries are classified into two types such as geometrically necessary boundaries (GNBs) and incidental dislocation boundaries (IDBs) [109,110], see **Fig. 2.16**. The GNBs are formed between regions of different strain patterns due to individual geometric deformation conditions, separating the crystallites. IDBs are formed by statistical trapping of glide dislocations because of mutual interaction or interaction with dislocation forest. They divide cell-blocks further down to cells (**Fig. 2.16** and **Fig. 2.17**). The cells are separated by cell walls. At the end of the stage III the cell walls becomes thick containing dislocation dipoles/multi-poles enclosing cell interior regions with small dislocation density [112,114].

Still, there are no distinct misorientations between the cells. These only occur in the stages IV [114,115] and V when strains $\gamma > 1$ are imposed to the material. During stage IV the density of polarized dislocations within the cell walls start to dominated being the reason for the rising misorientation across the cell wall [114]. Thus, cell walls gradually develop to high angle boundaries during deformation. Further, coalescence of different dislocation boundaries might also evolve into lamellar boundaries (LBs), see **Fig. 2.17**.

In stage V, the saturation of the stress is achieved. The saturation comes from the occurrence of dynamic dislocation recovery which increases until the annihilation of edge dislocations balances its generation [88]. As this dynamic dislocation recovery depends on the processing temperature, strain rate, hydrostatic pressure, and the alloying content, stage V clearly depends on these parameters, too. The situation is analogous to that known from

steady-state creep where the dislocation density is constant. As the edge dislocations are part of the grain boundaries, the grain size gets saturated as well [107]. It should be noted that for some special cases of materials containing nanograins, grain coarsening might occur upon SPD when its parameters - due to dynamic recovery – achieve a grain size larger than that before SPD (see e.g., the case of electrodeposited Ni where SPD processing induced some grain coarsening [116]).
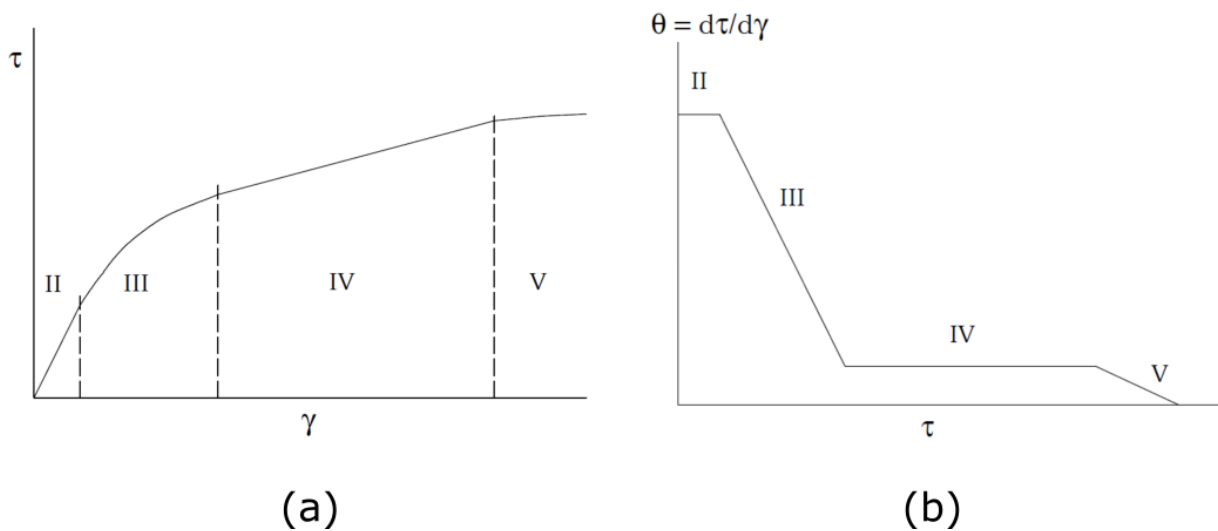
Fig. 2.15: (a) Scheme of stages in work hardening curve and (b) in work hardening rate plot for polycrystalline samples [117].
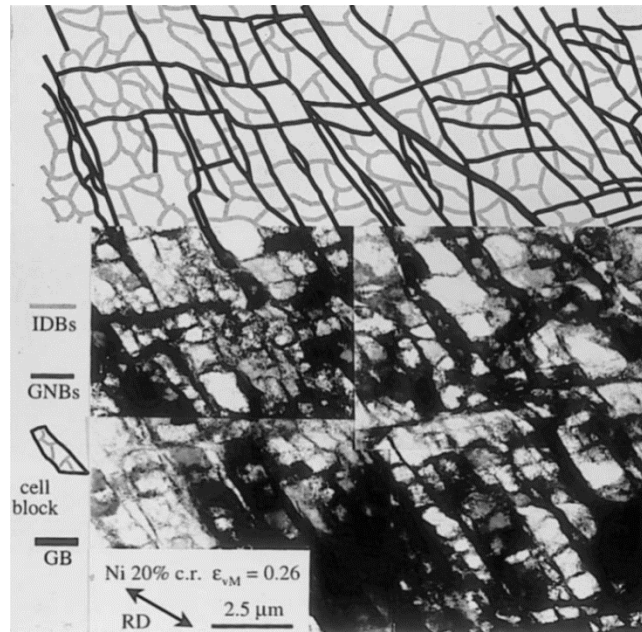
Fig. 2.16: Transmission electron micrograph of pure Ni (99.99%) cold rolled to a reduction of 20%. The top of the figure shows tracing of underlying and adjacent micrographs representing cell block structure composed of GNBs and IDBs. Long GNBs (i.e. microbands: MBs) are parallel to {111} slip planes and inclined to the rolling direction, taken from [110].
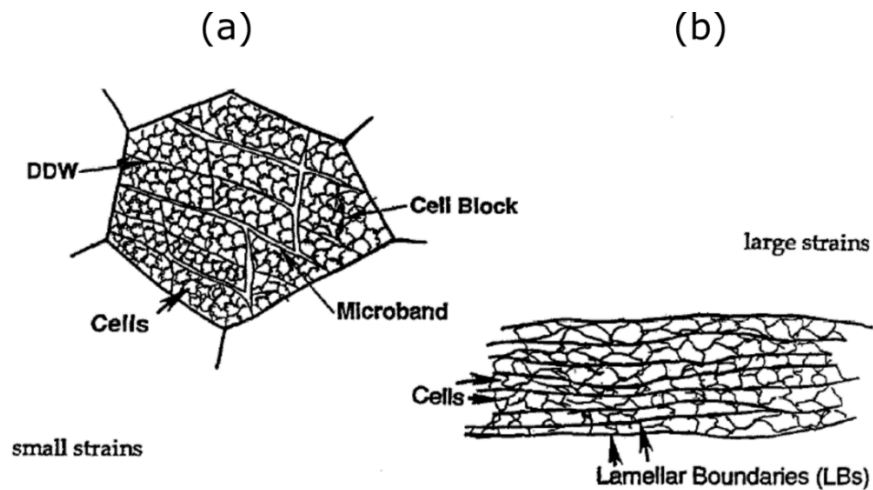
Fig. 2.17: Sketches of deformation induced dislocation boundaries: (a) for small to medium strain (γ = 0.06-0.8), dense dislocation walls (DDW) surrounding the cells in the cell blocks (its boundary is of the type GNBs) and long microbands form; (b) for large strain (γ > 1) deformation in the case of rolling, lamellar boundaries (LBs) parallel to deformation direction [109].

As shown by a series of papers by N. Hansen's group [109,110,118], for a quantitative description of the strength of SPD processed materials, one can simply consider the different structural elements which resist to dislocation motion, and sum up their individual strength contributions which can be taken from existing theories. These structural elements can be other dislocations, vacancy type defects, grain boundaries, solute atoms, particles, precipitates, etc. Then the total yield strength can be written as:

$$\sigma_{YS} = \left(\sigma_0 + \alpha MGb\sqrt{\rho}\right) + kd^{-0.5} \qquad (2.14)$$

where σ_0 denotes the strength of the undeformed single crystal and the second part the Taylor's relation [119] with ρ as the dislocation density, M the Taylor factor, G the shear modulus, b as the Burgers vector, and α as the interaction parameter representing the arrangement of the dislocations (varying from 0.2 to 0.5). The third part means the relation of Hall & Petch [120,121] with the dependence on grain size d; k is the materials speficic Hall-Petch coefficient. The misorientations between grains is thought to be 10° at minimum which cannot be overcome by the mobile dislocations).

The strength of the material including large plastic strains has been successfully simulated by fundamental constitutive models [72,112,122–124] in terms of fractions f_w of hard cell walls (areas of edge dislocations) and soft cell interior/channels f_c (areas of screw dislocations). The total resolved shear stress ($\hat{\tau}$) is given by:

$$\hat{\tau} = f_w\hat{\tau}_w + f_c\hat{\tau}_c \qquad (2.15)$$

where $\hat{\tau}_w$ and $\hat{\tau}_c$ corresponds to shear stress of edge and screw dislocation areas, respectively, with volume fractions related as $f_w + f_c = 1$. To maintain the coherency of the crystal, the total resolved shear strain has been assumed to be identical to both that of edge and that of screw areas, thus $\gamma = \gamma_w = \gamma_c$. Zehetbauer et al [94] have extended their model to the case of SPD by introducing the hydrostatic pressure and its restricting effect to diffusion i.e. to dynamic recovery/recrystallization and/or annihilation of edge dislocations. Sulkowski et al [72]showed how this concept can be used to predict the structural evolution during SPD as well.

2.2.4. Effect of SPD on mechanical properties in Ti and Ti-based alloys

This section gives an overview of the mechanical properties (strength and Young's modulus) of SPD processed ultra/nano-structured Ti and Ti-based alloys. Concerning the strength, this can be markedly increased due to the drastic decrease of the grain size and the marked increase of the dislocation density during SPD, see **eq. 2.14**. In contrast to the strength, the Young's modulus is rarely changed unless there is a phase transformation or a change of the texture. The increase of the strength can be affected by the deformation strain applied, the processing temperature and the strain rate, as well as by the hydrostatic pressure [94]. Also the type of SPD process plays some role in the resulting of micro/nanostructure and therefore the mechanical properties.

In the case of **pure Ti (α-phase)** E ~ 100 GPa [10] after application of ECAP (6 passes, route B$_C$) at 410°C the E value hardly changes, however the UTS value in the grade 2 Ti increases from 400 to 664 MPa [125,126]. Further rolling increases UTS to 985 MPa [127]. During the process the grain size reduced from 100 μm to 0.3 μm. In the case of HPT, however, there could occur an effect of hydrostatic pressure in addition to the shear strain. It was reported that there is no change of phase during HPT performed at pressures below 4 GPa [22]. The ultimate tensile strength (UTS) value increases to 900 MPa. When the HPT processing is performed at a pressure > 4 GPa the ω-phase appears showing a high strength (UTS=1170 MPa) [22] and E value (single phase ω-phase has E value of about 130 GPa [25] . The grain size refines to an average value of 150 nm. Similar values of strength and grain size were reported by various authors with slight scatter [23,24]. HE deformation of pure Ti with an accumulative strain of about 5.5 induces significant grain refinement in Ti down to 47 nm and a remarkable increase of UTS from 480 to 1320 MPa [128,129].

Recently more research works have been focused on **β-Ti–Nb based alloys** because of their intrinsically low E. With the aim to increase the strength of the binary [72,130], ternary [63,131,132], and quaternary β-type Ti–Nb-based alloys [70,71,76,133–137], they were subjected to different SPD techniques. Depending on the β-phase stability, SPD of β-Ti–Nb-based alloys may cause a pronounced change in the phase structure [64,71] or can yield only minor volume fractions of deformation induced phases such as of stress induced α"-martensite [133] or the ω-phase [137,138]. There is a large scatter in the observed data of E and strength depending on the alloy, heat treatment and type and parameters of the SPD deformation. Some examples are mentioned in the following. The lowest E value of 43 GPa was reported for the cold rolled (89% of thickness reduction) β-type titanium alloy Ti–35Nb–4Sn (in wt.%) [63]. The lowering of E value measured by tensile test was attributed to the texture of the parent β-phase and stress induced α"-martensite (($200)_{α''}$ $[010]_{α''}$ and $(001)_β$ $[110]_β$, respectively) The strength increases from a UTS value of about 500 MPa to 680 MPa [63]. In the case of Ti–36 Nb–2Ta–3Zr-0.3O (wt.%) alloy (known as "Gum Metal"),

the coarse-grained structure shows a E value of about 65 GPa and a UTS of about 750 MPa [139]. A cold-swaging processing causes an increase of the strength to a value of 1.2 GPa and E value decreases to around 40 GPa [139,140]. The HPT deformation at pressure of 6 GPa with N = 10 shows similar UTS values with an E value of 65 GPa [70,71]. The strength achieved is quite close to ideal strength of 1.7 to 1.9 GPa (calculated from the elastic constants [77,141]). Therefore it is argued that this high strength is due to the dislocation free mechanisms of plasticity such as macroscopic shear deformation termed as "giant faults" or the formation of nano-sized ω-precipitates [138,142]. However despite of many research works [75–77,134] the real potential deformation mechanism is not yet completely understood.

Near β or (α+β)- Ti–Nb alloy: The Ti–13Nb–13Zr (compositions in wt.%) alloy is studied more extensively in the literature. The properties like wear and corrosion resistance by tailoring of the microstructure by various thermo-mechanical processing have been reported [60,143,144]. However, the investigations of the mechanical properties with respect to SPD are limited. The effect of warm rolling on the UTS and E was reported in [145]. The E value after warm rolling is about 78 GPa nearly same to that of undeformed case and UTS increases from 900 to about 1030 MPa [145].

3. Experimental procedures

3.1. Materials

The two alloys: Ti–16.1 wt.% (~9.2 at.%) Nb and Ti–45 wt.% (~30 at.%) Nb were selected for the present dissertation work. In their coarse grained stage these binary alloys show an E value of about 65 GPa (see **Fig. 2.11**).

Samples of Ti–16.1 Nb alloy were obtained from IFW Dresden, Germany. High purity Ti (99.7 %) and Nb (99.8%) were used to prepare the ingots of Ti–16.1 Nb alloy in the arc melting furnace under Ar-atmosphere. These ingots were melted five times to ensure complete dissolution of Nb into Ti. After that these ingots were subjected to cold crucible casting method in order to obtain a rod of 10 mm in diameter. To achieve optimal chemical homogeneity, as-cast rod was homogenized in single β-phase field at a temperature of about 1000^0C for 24 hours followed by water quenching (WQ). Hereafter, these samples are denoted as WQ and treated as starting material.

The starting material for Ti–45.0 Nb alloy was a hot hydrostatic extruded bar received from ATI Wah Chang, Alabama, USA. Hereafter the starting material is denoted by INI. The chemical composition of INI is listed in **Table 3.1**

Table 3.1: Chemical composition of INI bar of Ti–45.0 Nb (wt.%).

Composition	Nb	Fe	Cr	Mn	Mg	Si	K	Na	O	N	Ti
	44.94	<0.03	<0.01	<0.01	<0.01	<0.1	<0.01	<0.01	0.095	0.007	balanced

3.2. Alloys subjected to SPD

3.2.1. High Pressure Torsion

From the rod of homogenized WQ Ti–16.1 Nb, the discs of about 0.85 mm in thickness and 8 mm in diameter were prepared by spark erosion and subjected to high pressure torsion (HPT) (see **Fig. 3.1**) applying a pressure P = 4 and 8 GPa and N = 1, 5, and 10 rotations (see **Table 3.2**). Similarly in the case of Ti–45 .0Nb, the samples were cut from INI sample as shown in **Fig. 3.2** and were subjected to HPT applying P = 4 GPa for N = 1, 5, and 10 rotations (see **Table 3.3**) These specimens are denoted as HPT-P-N, where P gives the value of the pressure in GPa and N the number of rotations. The rotation speed in all the cases is maintained to 0.2 rpm (revolutions per minute).

Table 3.2: Summary of HPT experiments carried out at room temperature (RT) in the case of Ti–16.1 Nb. The von Mises strain (ε) is calculated for edge of the HPT discs.

Specimens	Initial thickness (mm)	Finalthickness (mm)	ε
WQ	0.86	0.86	0
HPT-4-1	0.83	0.60	24
HPT-4-5	0.86	0.60	120
HPT-8-1	0.86	0.59	25
HPT-8-5	0.84	0.56	130
HPT-8-10	0.87	0.49	296

Table 3.3: Summary of HPT experiments carried out at RT in the case of Ti–45.0 Nb. The von Mises strain (ε) is calculated for edge of the HPT discs.

Specimens	Initial thickness (mm)	Final thickness (mm)	ε
Initial (INI)	0.81	0.81	0
HPT-4-1	0.82	0.49	30
HPT-4-5	0.82	0.44	165
HPT-4-10	0.81	0.43	337
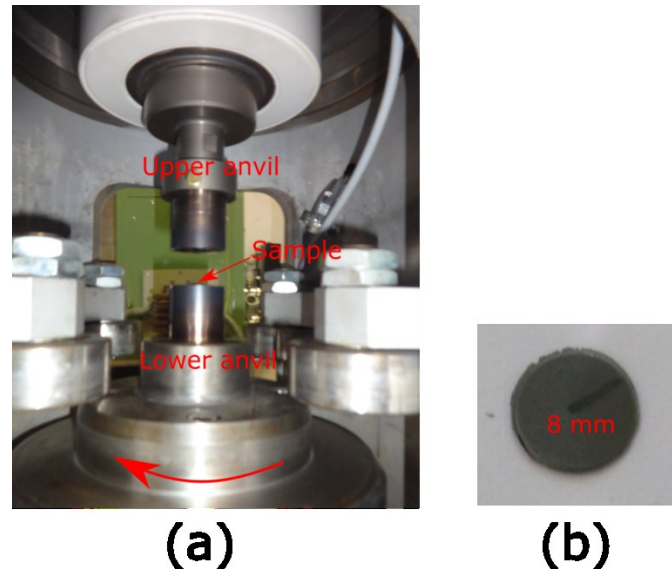
Fig. 3.1 (a) The high pressure torsion facility of the Research Group Physics of Nanosstructured materials, University of Vienna and (b) the specimens after processing.
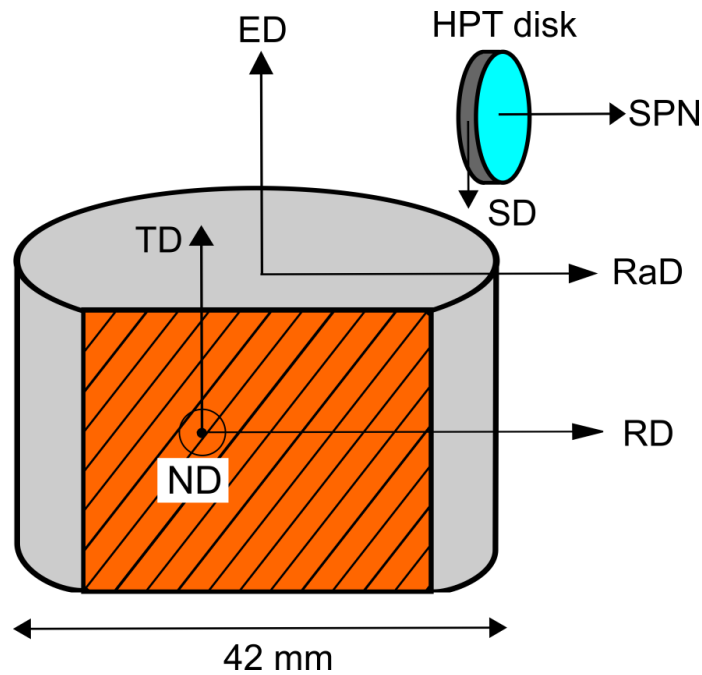
Fig. 3.2: Sketch showing samples taken from the INI bar for severe plastic deformation (SPD) processing. ED: extrusion direction, RaD: Radial direction, ND: normal direction, TD: transverse direction, RD: rolling direction, SPN: shear plane normal, and SD: shear direction.

3.2.2. Rolling and Folding

In the case of Ti–16.1 Nb alloys, the discs were subjected to rolling and initially reduced to 0.25 mm in multiple steps (it involves no folding (F) of the sample, counted as one effective rolling step, R). After that the strip was folded and rolled until the combined thickness reduced to half. This process is repeated to induce plastic strain into the material. These specimens were denoted by R&F-R, where R is the number of effective rolling steps and R = F+1. In the case of R = 1, 3, 5, and 7 (see **Fig. 3.3**), the von Mises strain ε was calculated using **eq. 2.13** and are 1.1, 3.3, 4.4, and 6.0, respectively. In the case of the Ti–45.0 Nb alloy, the rectangle shaped samples were cut from the initial bar with the rolling direction parallel to the radial direction of the INI sample (see **Fig. 3.2** and **Fig. 3.4**). In the case of R = 1, 3, and 5, samples were investigated further (the von Mises strain, ε is 1.5, 3.0, and 4.8 for R = 1, 3, and 5, respectively).

Fig. 3.3: Selected specimens of Ti–16.1 Nb processed by R&F.
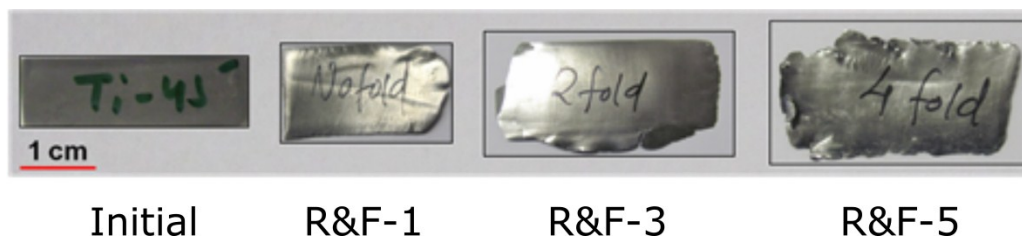
Fig. 3.4: Selected specimens of Ti–45.0 Nb alloy processed by R&F.

3.3. Ti–Nb based alloys subjected to hydrostatic compression

Specimens of the Ti–16.1 Nb and Ti–45.0 Nb alloys were subjected to hydrostatic compression at a constant pressure (see **Table 3.4**). This hydrostatic pressure is achieved by compressing the discs in the HPT anvils without rotating them. These samples are represented as HP-P (HP - hydrostatic pressure; P - value of the pressure). The true compressive strain $C = \ln\left(\frac{t_0}{t_e}\right)$ (indentical to von Mises strain ε for uniaxial compression) was calculated; where t_0 and t_e are initial and final thickness of the specimen, respectively.

Table 3.4: Ti–Nb alloys subjected to hydrostatic compression experiments.

	Specimens	Initial thickness (mm)	Final thickness (mm)	ε
Ti–16.1 Nb	HP-1	0.85	0.84	0.011
	HP-4	0.83	0.81	0.024
	HP-8	0.86	0.83	0.034
Ti–45.0 Nb	HP-4	0.83	0.81	0.024
	HP-8	0.84	0.82	0.023

3.4. X-ray diffraction

X-ray diffraction (XRD) technique is a non-destructive method, generally utilized to determine the structural parameters and to identify the crystalline phases by knowing the corresponding characteristic Bragg peaks in the diffractogram. This also extends to the Rietveld procedure to quantify the phase fractions in the multiphase systemand its applications include determination of the orientation (texture), of the crystallite size, and of dislocation density in the material, etc. These methods are described in the corresponding sections.

The structural investigations of both alloys were carried out by XRD using Cu-K$_\alpha$ radiation (λ = 0.15406 nm) with a spot size of 0.8 mm in an AXS BRUKER D8 diffractometer in reflection geometry. Also some of the samples were also subjected to synchrotron radiation with an energy of 50 KeV (λ = 0.0248 nm) at the PETRA–III facility, Hamburg, Germany. To know the thermal stability phases in HPT processed Ti–16.1 Nb (P = 8GPa, N =10) the samples were also subjected to in-situ diffraction experiments from RT to 800°C

with a rate of 10°C /min, respectively at the ID11 beam-line (energy of 60 keV i.e. $\lambda = 0.02068$ nm and spot size of 50 µm × 50 µm) at the European Synchrotron Radiation Facility (ESRF), Grenoble, France. In order to measure the rate of change of temperature of the heating stage "Linkam" was calibrated using melting points T_m of the standard samples such as Sn ($T_m = 232°C$, $T_{measured} = 263°C$), Zn ($T_m = 420°C$, $T_{measured} = 518°C$) and Al ($T_m = 660°C$, $T_{measured} = 838°C$) and allotropic transformation temperature of Ti ($T_{\alpha \to \beta} = 882°C$, $T_{(\alpha \to \beta)measured} = \sim 1000°C$). The obtained 2D diffraction patterns were processed and integrated through the FIT2D [146] software.

3.5. Rietveld refinement method

The Rietveld refinement technique was developed by Rietveld [147,148] and is usually applied to the neutron/X-ray/synchrotron diffraction data. The primary purpose of this method is to refine the structural parameters of individual phases and to quantify the phase fractions in the material by fitting the calculated intensity profile $y_{i,c}$ with measured/observed diffraction data $y_{i,o}$. The i refers to the points in the pattern. The equation of the calculated intensity can be written as

$$y_{i,c} = y_{i,b} + \sum_p \sum_{k=k_i^p}^{k_i^p} G_{i,k}^P I_k \qquad (3.1)$$

where $y_{i,b}$ is the background intensity, $G_{i,k}$ is a normalized peak profile shape function, I_k is the intensity of the kth Bragg reflections and the p corresponds to phase present in the sample.

The intensity I_k is given by the equation

$$I_k = SM_kL_k|F_k|^2P_kA_kE_k \qquad (3.2)$$

where S is the scale factor, M_k, L_k, P_k are the multiplicity factor, Lorentz polarization factor, preferred orientation parameter [149], respectively. A_k [150,151] and E_k [152] are the absorption and extinction correction factor. F_k is the structure factor.

Besides the background contribution, the calculated intensity value largely depends on the structure factor and multiplicity. The background contribution to the intensity is a significant factor and should be refined with care. The background level can be estimated either by linear interpolation of the base points between the peaks and then subtracted, or

can be modeled with different polynomial functions [153] depending on the complexity of the pattern. To get a satisfactory refinement the peak shape function has to be accurately described. The peak shape of a reflection is a function of material (crystallite size, lattice strain) and instrumental parameters (radiation, slit width, detector, etc.). Usually one applies the pseudo-Voigt peak shape function to the X-ray diffraction data.The peak profile shape function $G_{i,k}$ for the pseudo-Voigt can be written as

$$G_{i,k} = \gamma \frac{C_0^{1/2}}{H_k \pi}[1 + C_0(2\theta_i - 2\theta_k)^2]^{-1} + (1 - \gamma)\frac{C_1^{1/2}}{H_k \pi^{1/2}}\exp[-C_1(2\theta_i - 2\theta_k)^2] \qquad (3.3)$$

where $C_0 = 4$, $C_1 = 4\ln2$ and H_k is the full-width at half maxima (FWHM) of the kth reflections, γ = mixing parameter ($\gamma = 0$ and 1, for Gaussian and Lorentzian profile shape functions, respectively).

The variation of the peak FWHM is defined by the function described by Caglioti et al. [154]:

$$H_k = (U\tan^2\theta + V\tan\theta + W)^{1/2} \qquad (3.4)$$

These U, V, and W are the refinement parameters. It is worth to mention that these parameters could be refined and work well in the case of isotropic or random polycrystalline samples. However, these parameters may not be able to describe an anisotropic effect on line broadening (i.e. hkl dependence line broadening) [155]. In addition any peak asymmetry for the profile function can also be refined for the fit procedure [155,156].

In Rietveld analysis, the difference of the measured and calculated diffraction patterns is called as residual R, and is minimized by least square methods such as the Newton-Raphson or the Levenberg-Marquardt algorithm. This residual is best described in terms of agreement index, weighted-profile R value R_{wp}.

$$R_{wp} = \left[\sum_i \frac{w_i(y_{i,o} - y_{i,c})^2}{w_i(y_{i,o})^2}\right]^{1/2} \qquad (3.5)$$

where the weight w_i is expressed as $(\mathbf{w_i})^{-1} = \boldsymbol{\sigma_{i,g}^2} + \boldsymbol{\sigma_{i,b}^2}$, $\sigma_{i,g}$ is the standard uncertainty in the gross intensity and $\sigma_{i,b}$ is the standard uncertainty in background intensity.

Ideally, the R_{wp} will approach the statistically expected R-value, but it should never be below R_{exp}.

$$R_{exp} = \left[(N - P)/\sum_i^N w_i(y_{i,o})^2\right]^{1/2} \tag{3.6}$$

where N = number of data points, P = number of variable parameters. For a diffraction data N >> P and thus the subtraction can be safely ignored. The ratio of squares of R_{wp} and R_{exp} yields another parameter, generally described as goodness of fit (GOF).

The quantitative phase analysis can be performed in multiphase samples, generally expressed in weight fractions [157,158]. The weight fraction of the phase p can be written as

$$w_p = \frac{(SZMV)_p}{\sum_i(SZMV)_i} \tag{3.7}$$

where S, Z, M, V are Rietveld scale factor, number of formula units per unit cell, molecular weight of the formula unit, volume of the unit cell, respectively.

In order to obtain the phase fractions of the Ti–16.1 Nb alloy after SPD and heat treatment, the corresponding diffraction data were collected by the synchrotron radiation facility PETRA–III, Hamburg, Germany and the European Synchrotron Radiation Facility (ESRF), Grenoble, France. and AXS BRUKER D8 diffractometer. Further XRD data were subjected to Rietveld refinement using X'pert Highscore plus software. In the case of Ti–45.0 Nb alloy, Rietveld refinement procedure was not necessary since all peaks correspond to a single β-phase.

3.6. Measurement of X-ray crystallographic texture

In polycrystal each grain represents an individual orientation, and thus the orientation differs from grain to grain. At any stage of a recrystallization and/or deformation process, the distribution is rarely random; grains exhibit a certain propensity of the orientations. The latter is commonly termed as "preferred orientation", and a non-random orientation distribution is called "texture". In general, we are discussing here the distribution of the orientations in a polycrystalline aggregate with respect to a fixed reference system.

The texture has an influence on all physical properties which are sensitive to crystallographic directions and planes, such as Young's modulus, strength, electrical conductivity, magnetic susceptibility, and others. The orientation of the grain can be defined as the relation between positions of the crystal coordination system and the specimen coordinate system, represented by orientation matrix, Euler angles, Miller indices,

angle/axis pair, and Rodrigues vector. The distribution of orientation i.e. the texture is generally represented by pole figures, inverse pole figures, orientation distribution functions. A detailed description of these mathematical tools and the texture representation can be found elsewhere [159].

The X-ray texture measurements were not applied to Ti–16.1 Nb alloy before and after SPD as these samples show strong overlapping peaks of the various phases. Hoever, it is successfully applied to the all the cases of SPD processed β-bcc type Ti–45.0 Nb alloy in close collaboration with Prof. W. Skrotzki, TU Dresden, Germany. In the case of INI sample the measurements were carried out at the center of the cross-section. For HPT discs the analysis was performed at a distance of 2 mm from the center of the HPT disc. In the case of samples R&F the texture measurements were carried out rolling plane. In order to get the good quality in texture results, the samples were mechanically polished using 2400 grid SiC paper. The texture measurements were carried out with a HZG-4 texture goniometer with a spot size of 6 mm x 5 mm for the rolled samples. Cu K_α radiation with a wavelength of λ = 0.154 nm was generated at a voltage of 40 KV and current of 35 mA, using a point scintillation type detector. For HPT samples, AXS BRUKER D8 diffractometer equipped with a GADDS (General Area Diffraction Detection System) area detector was used. The Cu K_α beam was collimated achieving a spot size of 100 μm on the sample. The texture measurements were done in reflection mode.

To gain sufficient information about the texture from the pole figures and further construction of ODF, the distribution of the poles from a minimum of two or three reflections (ref. **Table 3.5**) are required in the case of highly crystal symmetric cubic systems. Therefore, the distribution of the diffraction intensities from three crystal planes {110}, {200} and {211} were collected for sample rotations ɸ (integral scanning - 0° to 360° in step of 5°) for each tilt χ of Eulerian cradle (90° to 25°, in step of 5°). The angles ɸ and (90°–χ) correspond to the azimuthal angle β and α in the pole figure, respectively (refer **Fig. 2.8 and 4.3** of [159]). The ODFs were calculated using Arbitrary Defined Cells (ADC) methods [160] using experimentally obtained pole figures as input for the LABOTEX software [161]. The textures have been represented by both pole figures and ODFs.

In the case of HZG-4 texture goniometer, the X-ray path is controlled by using a combination of vertical and horizontal slits. From X-ray tube to sample, the slit sizes were 0.4 mm (horizontal slit size) and 0.35 mm (vertical slit size). The beam between sample and detector was limited by using horizontal and vertical slits of 8.65 and 8 mm, respectively. The counting time of 5s for each particular χ and ɸ angle was maintained. In the case of AXS BRUKER D8 diffractometer, the GADDS area detector covers up to approximately 35° in 2θ range at a fixed position. Therefore to measure the distributions of all the three reflections two frames are required (ref. **Table 3.5**). Since the frame in the area detector at a fixed

position (ω and χ; e.g. 90°) covers a range of values of the α and the 2θ (running along horizontal) a large proportion of scans in the pole figure(s) measurement can be obtained. Additional scans for pole figures are achieved by further tilting and rotation of the sample. Thus in order to plan scans in the pole figure construction for measurement and further to generate the intensity data for β scans over each α ranging up to70° after the measurement. a special BRUKER software MULTEX –AREA was used (see **Fig. 3.5**).

Table 3.5: Bragg reflections and their positions in 2θ used for calculation of macrotexture (Cu Kα beam).

Reflections	Bragg's position in 2θ, °
{110}	38.83
{200}	56.00
{211}	76.15

In the next step, the data obtained were evaluated by LABOTEX software for more advanced texture analyses. At first, incomplete pole figures (α ranging up to70°) did result. As a next, 3D-ODFs were calculated by an iteration-based method [160] from three incomplete pole figures. Then complete pole figures (α ranging up to 90°) were derived by recalculation from the ODFs. In the case of R&F samples, the ODF symmetrization was performed from triclinic system to orthotropic sample symmetry, in order to enhance the component analyses. In the case of HPT, a monoclinic sample symmetry was applied.

(a)	(b)	(c)
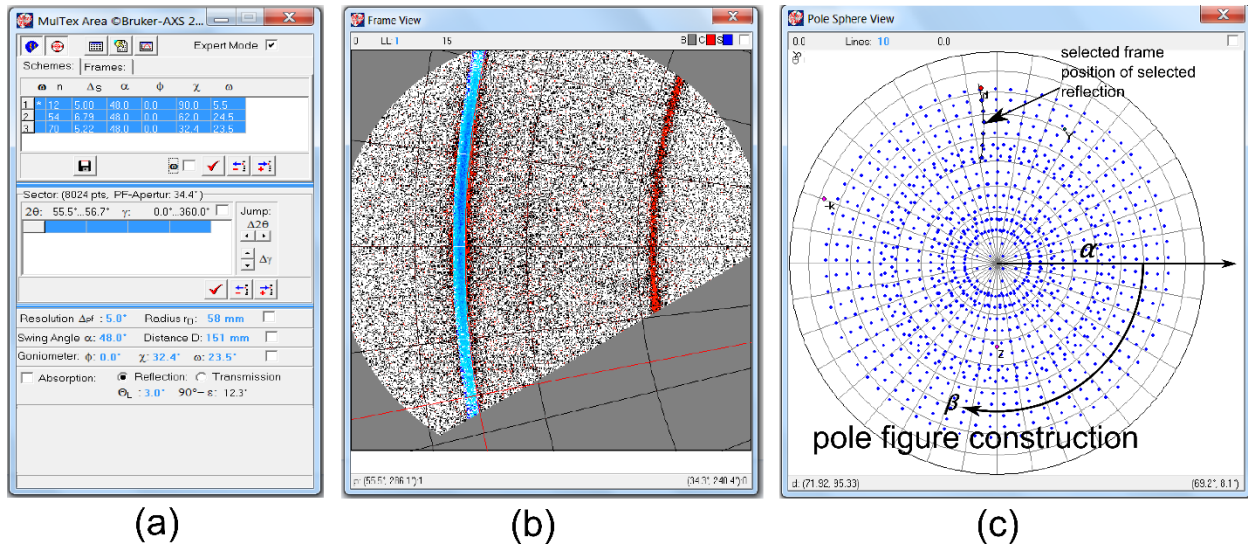
Fig. 3.5: *The main user interface of Multex Area software; (a) scheme plan for pole figure measurement considering high angle reflection {200} contained in the first frame, (b) selected reflection in the first frame, and (c) pole figure construction for both {110} and {200} reflections, contained in the first frame to obtain the intensity scans over β for each α ranging up to70°.*

3.7. X-ray Line Profile Analysis (XLPA)

X-ray diffraction peak profile analysis is a powerful technique to determine the density and arrangements of the dislocatios, and the CSD (crystallite) size. The crystallite sizes obtained by X-ray diffraction is equivalent to the mean size of domains which scatter X-rays coherently [162]. The CSD size is typically smaller than grain size obtained from TEM. In this work, the so called convolution multiple whole profile [163,164] (CMWP) fitting procedure was used. This is based on model utilizing Fourier transforms for size broadening (broadening of the peak is caused by smallness of CSD size) and strain broadening (broadening caused by lattice defects such as dislocations, stacking faults, twinning and others). In this procedure it is assumed that the spherical crystallites follow a log-normal size distribution. The strain in most cases is associated to dislocations unless the contrast factor follows another dependence on the diffraction vector (for details see below).

Diffraction measurements usually provide the intensity I vs 2θ profile. In the CMWP procedure, this diffraction pattern can be described by the convolution of (domain/crystallite-) size (s), and (defect-) distortion (D) intensity profiles and expressed as $I^{Net} = I^s * I^D + I^{BG}$, where I^{BG} is the background intensity.

This intensity profile I^{Net} can also be written in cosine Fourier function $F_c(s)$ as

$$F_c(s) = 2 \int_0^\infty A(L)\cos(2\pi Ls)dL \tag{3.8}$$

The Fourier coefficient of the peak profiles A(L) is the product of size Fourier coefficient $A^s(L)$ and distortion Fourier coefficient $A^D(L)$ [165,166]. The $A^s(L)$ coefficient is a function of the median m and variance σ of the log-normal distribution.

$$A(L) = A^s(L) * A^D(L) \tag{3.9}$$

where L is the Fourier length. Assuming the strain is represented by the dislocations, the distortion Fourier coefficient $A^D(L)$ can be expressed in the following form:

$$A^D(L) = \exp\left(-2\pi^2 g^2 L^2 < \varepsilon_{g,L} >^2\right) \tag{3.10}$$

where g is the absolute value of the diffraction vector, $<\varepsilon>^2$ is the mean square strain caused by the dislocations. Several researchers have worked on the determination of mean square strain value. Out of these, Wilkens' dislocation model [167] for estimation of $<\varepsilon>^2$ gives a satisfactory result. He introduced a length parameter, i.e. the effective outer cut-off radius of a dislocation (R_e^*), instead of crystal diameter. It is assumed that the crystal contains separate regions with a diameter of R_e^*, in which parallel screw dislocations are randomly distributed and within each of these regions the distribution of the dislocations with density of ρ is completely random. It can be written as

$$\varepsilon_{g,L} = \left(\frac{b}{2\pi}\right)^2 \pi\rho Cf\left(\frac{L}{R_e^*}\right) \tag{3.11}$$

where b is the absolute value of the Burgers vector, ρ is the dislocation density, C is the contrast factor [168–172] of the dislocations and f is the strain function. The values of C depend on the relative orientation of the line, burgers, and diffraction vectors. If all the possible slip systems in a crystal are equally populated or if the polycrystal is texture free, then C for a particular g and b can be weighted average to determine effective $\bar{C}$. For cubic crystals,

$$\bar{C} = \bar{C}_{h00} \, (1 - qH^2) \qquad (3.12)$$

where $\bar{C}_{h00}$ is the average dislocation contrast factor for h00 type reflections and $H^2 = (h^2k^2 + h^2l^2 + k^2l^2)/(h^2 + k^2 + l^2)^2$, q is the fitting parameter depending on the elastic constants of a crystal C_{11}, C_{12}, and C_{44}, the anisotropy factor $A_i = 2\,C_{44}/\,(C_{11}-C_{12})$, and the ratio of C_{11}/C_{12}. A detailed calculation can be read in [168].

In the present work, the CMWP procedure is applied to XRD patterns obtained from synchrotron radiation experiments at ESRF, Grenoble, France for all SPD processed Ti–45.0 Nb alloys. The size parameters (median m and variance σ) and strain parameters (ρ, q, and R_e^*) are varied for the profile fitting to determine the CSD size and dislocation density. This procedure can not be applied to SPD processed Ti–16.1 Nb alloy since it shows stong overlapping of peaks of various phases.

The graphical interface of the CMWP program is shown in **Fig. 3.6**. (for R&F-1 sample of Ti–45.0 Nb alloy) The fixed parameters such as The lattice parameter a_{bcc} = 0.3286 nm, Burgers vector b $= \left(\frac{\sqrt{3}}{2}\right) a$ = 0.2845 nm, wavelength λ = 0.020686 nm, the average contrast factor considering screw and edge dislocation for 200 reflection, $\bar{C}_{200}$ = 0.316 (using the numerical code program ANIZC, http://metal.elte.hu/anizc developed by Borbeley et al. [173] and using the elastic constants C_{11} =137 GPa, C_{12} = 109.6 GPa, and C_{44} = 33.17 GPa, calculated for a single crystal of Ti–45.0 Nb [9]) were introduced into the program. The starting values of fitting parameters (a, b, c, d, and e) are varied. The measured and calculated patterns are compared using the Marquardt-Levenberg nonlinear least square algorithm [174,175]. In this numerical procedure the weighted sum of squared residuals (WSSR) is minimized (default is 10^{-9}). The number of iterations was selected as 100. The fitting procedure is stopped if the specified number of iterations is reached or if the relative change of WSSR between two iterations is below the fit limit of 10^{-9}.

The fitting parameters a, b, c, d, and e are related to the physical quantities as follows:

$$\mathbf{q = a}, \qquad (3.13)$$
$$\mathbf{m = exp\,(b)}, \qquad (3.14)$$
$$\mathbf{\sigma = \frac{c}{\sqrt{2}}}, \qquad (3.15)$$
$$\mathbf{\rho = \frac{2}{\pi(b_{Burgers}d)^2}}, \qquad (3.16)$$

$$\mathbf{R_e^* = \frac{exp\,(-1/4)}{-2e}} \qquad (3.17)$$

The resulting physical quantities are q, m, σ, ρ, R_e^*, M^* are collected from the solution file and these are statistically averaged for low WSSR (within 10% variation). The CSD size (denoted by the area weighted crystallite size <X_area>) is calculated by the relation below:

$$< X_{area} > = m \, exp(2.5\sigma^2) \qquad (3.18)$$

In the case of R&F processed Ti–45.0 Nb alloy (the sample R&F-1) the resulting parameters; m, σ, <X$_{area}$> ρ, M, and q are obtained as (37$\pm$5) nm, 0.5 $\pm$ 0.1, (65 $\pm$ 7) nm, (1.61 $\pm$ 0.15) $\times$ 10^{15} m^{-2}, 1.0 $\pm$ 0.1, and 1.5, respectively.

Fig. 3.6: The graphical interface of the CMWP program applied to R&F processed Ti–45.0 Nb alloy (R&F-1). The fixed crystallographic parameters (crystal structure = cubic, lattice parameter a = 0.3286 nm, Burgers vector b = 0.2845 nm, average contrast factor for the 200 reflection C_{h00} = 0.316) and the experimental parameters (wavelength = 0.0206 nm, N_1 = 256, N_2 = 256, profile cutting parameter = 2.5) are introduced. The ellipticity is maintained as 1 representing spherical crystallites (init_epsilon = 1). The size parameters (b and c) and strain parameters (a, d, and e) are varied for profile fitting.
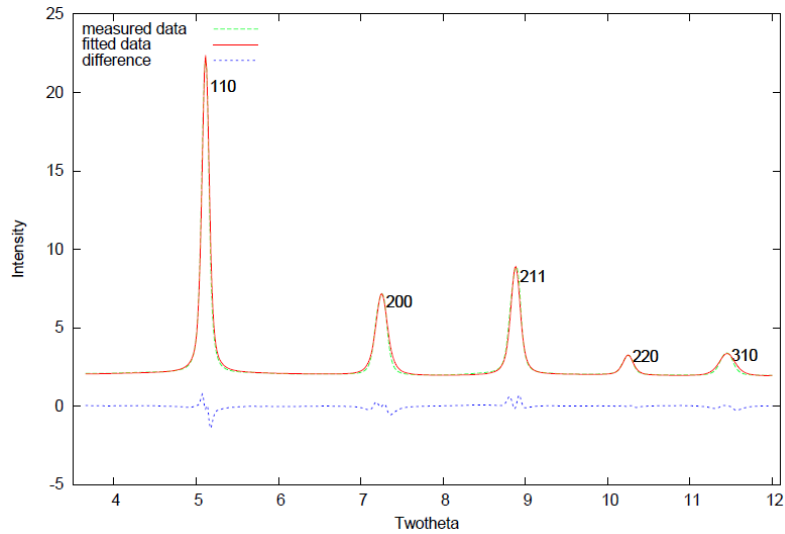
Fig. 3.7: A profile fitting for R&F processed Ti–45.0 Nb alloy (R&F-1): the measured data (green), fitted data (red) and the difference in the profiles (blue) as obtained from evaluate program.

3.8. Transmission Electron Microscopy (TEM)

In this technique a beam of high energy electrons is allowed to transmit through the thin specimen (<100 nm). The path and spread of the electron beam on to the specimen is controlled by condenser apertures and electromagnetic lenses such as condensr lens, and objective lens. Beyond the specimen the path and spread of the scatterings are controlled by the objective lens, diffraction aperture. The electrons interact with the specimen either produces the image with high resolution or diffraction pattern in the reciprocal space. These can be collected to an imaging device, such as a fluorescent screen, or to the CCD camera.

The formation of diffraction pattern (see **Fig. 3.8 (a)**) is achieved by removal of the objective aperture/contrast aperture (located back focal plane of the objective lens), inserting the selected area diffraction (SAD) aperture (at the image plane of the objective lens) as well as decreasing the strength of intermediate lens. The diffraction pattern (DP) without using SAD is not very useful because of two reasons; the specimen is more often buckled, so the DP will be distorted and the direct beam is also too intense for the CCD camera. Therefore, SAD aperture is used to limit the intensity and to select the region of interest. To form the image on the fluorescent screen reverse procedure is followed i.e. removal of the SAD aperture, insertion of the objective aperture and increase the strength of intermediate lens (see **Fig. 3.8 (b)**). In TEM equipment, the change of diffraction mode to

image mode is handled by a push button which actually changes the strength of intermediate lens. The objective aperture controls the collection angle of the beam. So when inserted it gives a very good contrast with a liitle reduction in resolution. Therefore, it is also called as contrast aperture. To image the bright field, the objective aperture is placed on to the direct beam and for the dark field image the objective aperture is placed on the diffracted beam.

For this thesis, microstructural investigations in SPD processed samples were carried out mainly in TEM, Philips CM 200 operated at 200 kV. In the case of Ti–16.1 Nb alloy, the specimens of 2.3 mm in diameter at a distance of 2.5 mm from the center of the HPT disc (HPT-8-10 i.e. processed at P = 8 GPa, N =10) were punched by spark erosion. Beforehand, the samples were dimpled and ion-milled. For HPT-8-10 after isochronal heat treatment in DSC, the microstructural investigations were also made. In the case of Ti–45.0 Nb the TEM investigations were made at the center of the INI sample on its cross-section, in the direction of the torsion axis for the HPT-4-10 sample at a radial distance of 1.5 mm from the center of the disc and on the rolling plane for the R&F-5 sample. TEM bright field and dark field image were taken in addition to selected area diffraction pattern (SADP). The SADPs were analyzed using the PASAD software package [176].
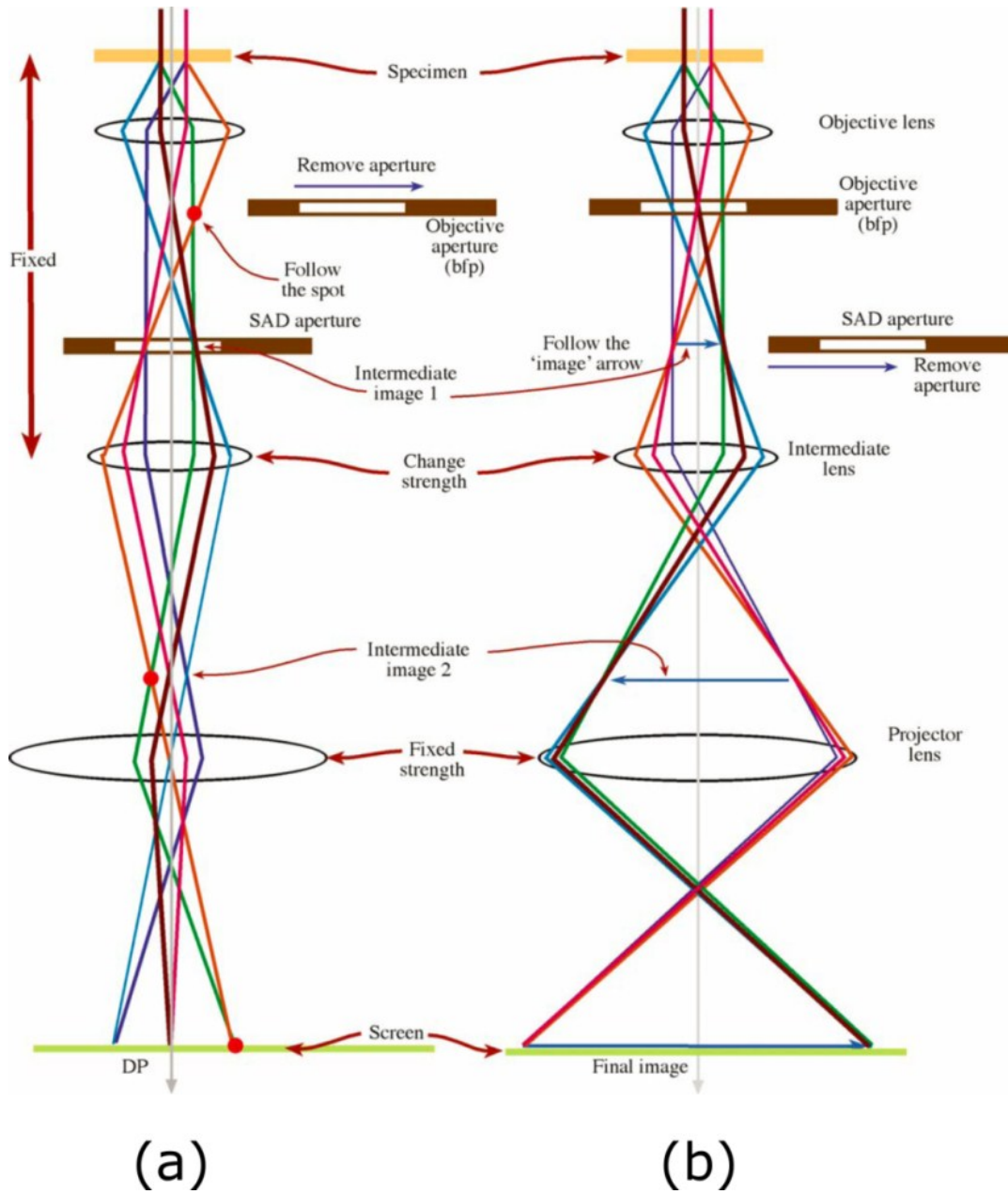
Fig. 3.8: (a) Diffraction mode and (b) imaging mode in TEM operation [177].

3.9. Microhardness

Hardness can be defined as the resistance of the material to the plastic deformation which gives an indication of the strength of the material. There are several types of indentation techniques available and Vickers microhardness technique is one of them. It uses a square-base diamond pyramid as the indenter with the opposite indenter faces are 136° angles apart. These are expressed in HV (Vickers hardness in MPa), which can be defined as the ratio of load to the surface area of the indentation. The area is calculated by measuring the lengths of the diagonals of the impression in the microscope. The HV is determined by using following relation

$$\mathbf{HV} = \frac{\mathbf{2Fsin(\theta/2)}}{\mathbf{d^2}} = \frac{\mathbf{1.854\,F}}{\mathbf{d^2}} \tag{3.19}$$

where F is the force in N, d is the length of the diagonal in mm.

The samples of Ti–16.1 Nb and Ti–45.0 Nb alloys before and after SPD were mechanically grinded up to 4000 grid paper and further cloth polishing using 0.05 μm alumina suspensions. Microhardness tests were performed using Vickers indenter. All indentations were carried out using a force of 1.96 N with a dwell time of 10s.

Fig. 3.9: Schematic of Vickers hardness test [178]*.*

3.10. Nanoindentation

Nanoindentation [179,180] has been most commonly used technique to measure the hardness H and elastic modulus E of the materials. They are determined from the single nanoindentation load-displacem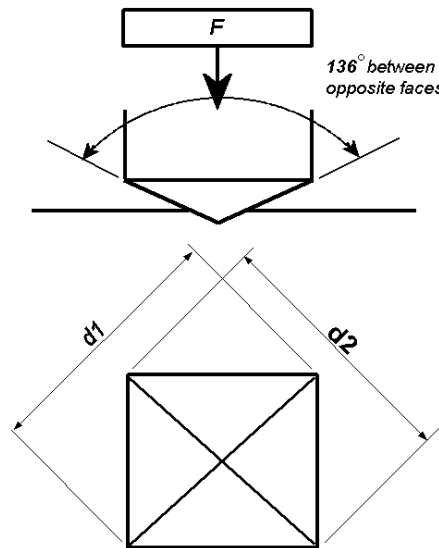ent measurement without need of imaging indent's imprint. A schematic of load vs displacement curve, obtained using Berkovich indenter is shown in **Fig. 3.10**, where P denotes the load and h is the displacement relative to the undeformed surface. Nanoindentation analysis is based on the unloading curve behavior. This curve is a non-liner one and can be modeled using the power law relationship as follows:

$$P = \alpha(h - h_f)^m \qquad (3.20)$$

where α and m are power law fitting parameters. In the case of Berkovich indenter it is 1.5 [180].

The loading and unloading condition of the indenter is schematically shown in **Fig. 3.11**. Here the behavior of the Berkovich indenter is modeled by a conical indenter with half included angle $\phi = 70.3°$ *and* the assumption is that the material adjacent to indenter sinks (no pile up). The sink in height can be expressed as

$$h_s = \varepsilon \frac{P_{max}}{S} \qquad (3.21)$$

where ε is indenter shape factor. For Berkovich indenter $\varepsilon = 0.7$ and for the flat punch this value is 1. The contact depth (h_c) along which contact is made between the indenter and the material can be written as

$$h_c = h_{max} - \varepsilon \frac{P_{max}}{S} \qquad (3.22)$$

Once the contact depth is known, the contact area *A* is can be calculated and hardness is estimated using the relation:

$$H = \frac{P_{max}}{A} \qquad (3.23)$$

where

$$A = F(h_c) = \sum_{n=0}^{8} C_n (h_c)^{2-n} = C_0 h^2 + C_1 h + C_2 h^{1/2} + C_3 h^{1/4} + \cdots + C_8 h^{1/128} \qquad (3.24)$$
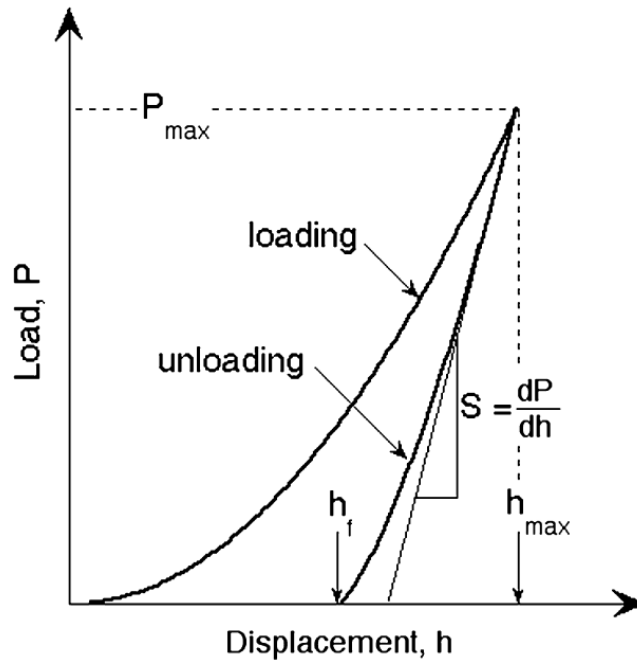
Fig. 3.10: Schematic of load (P)-displacement (h) curve obtained during one cycle of loading and unloading using a Berkovich indenter [180]. *h_{max} is the total displacement of the indent during at $P = P_{max}$, and h_f is the net plastic deformation after recovery of the elastic part during unloading.*
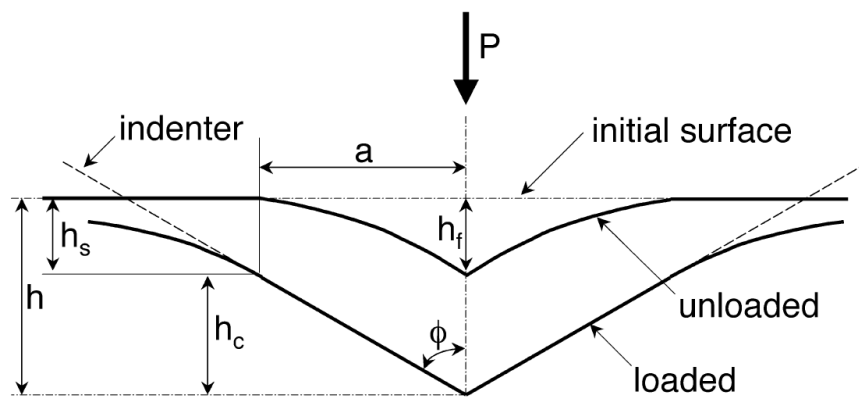
Fig. 3.11: Schematic of unloading process of the indentation [180]. *$h_{max} = h$ is the total depth of penetration, h_c, h_s correspond to contact depth and sink-in depth, respectively.*

The parameter elastic unloading stiffness S (commonly called as contact stiffness), is calculated as S = dp/dh from the upper portion of the unloading curve (see **Fig. 3.10**). The elastic modulus is also related to contact area A and the unloading stiffness S through the relation

$$S = \beta \frac{2}{\sqrt{\pi}} E_{eff} \sqrt{A} \qquad (3.25)$$

E_{eff} is the effective elastic modulus, given by

$$\frac{1}{E_{eff}} = \frac{1-\vartheta^2}{E} + \frac{1-v_i^2}{E_i} \qquad (3.26)$$

where E and E_i are the Young's moduli of the specimen and indenter, respectively and υ and υ_i are the corresponding Poisson's ratios, E_i = 1140 GPa, υ_i = 0.07.
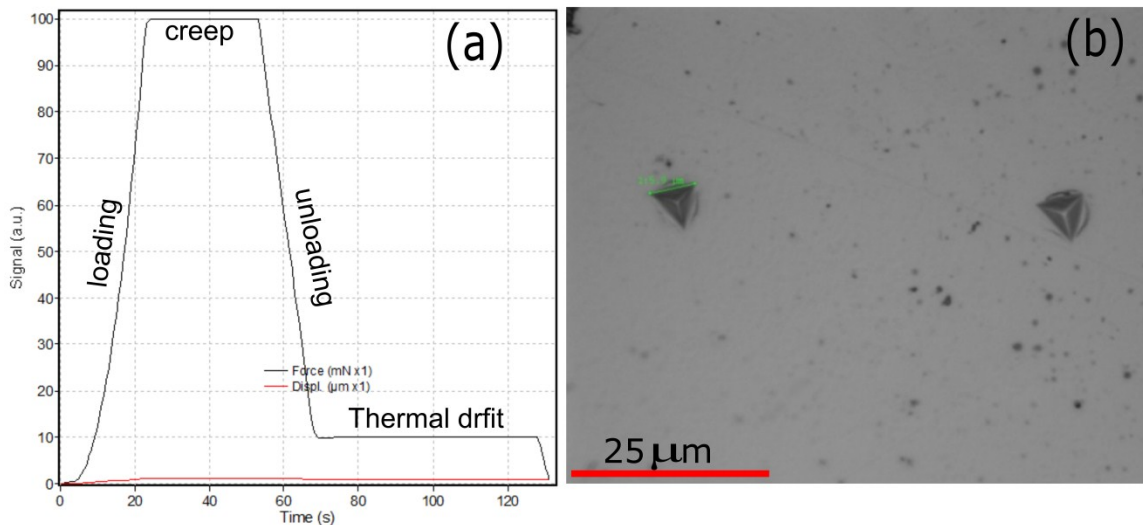
Fig. 3.12: (a)The ISO14577 standard module selected for hardness and Young's modulus measurements (Loading rate = 100 mN/20 s, Creep = 30s at maximum load of 100 mN, Unloading rate = 9 mN/s, thermal drift being 10 mN for 60s), (b) two residual impressions of Berkovich indenter on as-received Ti–45.0 Nb alloy.

The samples of Ti–161 Nb and Ti–45.0 Nb alloys before and after SPD were mechanically polished up to 4000 grid paper and further cloth polishing using 0.05 μm alumina suspensions. Nanoindentation experiments were carried out using a Berkovich indenter (maximum force of 100 mN) in UNAT equipment from ASMEC laboratories. The ISO14577 standard hardness and modulus measurement module was followed, shown in **Fig. 3.12**. The indents are spaced about a distance of 50 μm. Twenty five indentations were applied on each sample. The Poisson's ratio was assumed to be 0.31 and 0.41 for Ti–16.1 Nb and Ti–45.0 Nb, respectively. The Oliver and Pharr method [179] was used to determine the hardness and Young's modulus.

3.11. Micro-tensile tests

A tension test (stress-strain curves) offers most of the important properties of the materials such as Young's modulus E, Ultimate Tensile Strength (UTS), Yield stress, ductility. The conventional tensile test measurement involves large sized samples and therefore the strain is generally calculated by the movement of the crosshead. However, for the case of some material processing where the sample size is limited e.g. HPT, the measurement of the tensile properties is quite critical because of well-known size effect [181] which influences the mechanical properties largely. Hence the measurement requires the use of the non-contact optical strain sensors (in this work laser speckle strain sensor [182] based on the theoretical work of Yamaguchi [183]) to measure the strain with accuracy and also the sample size is too small for use of conventional strain sensors.
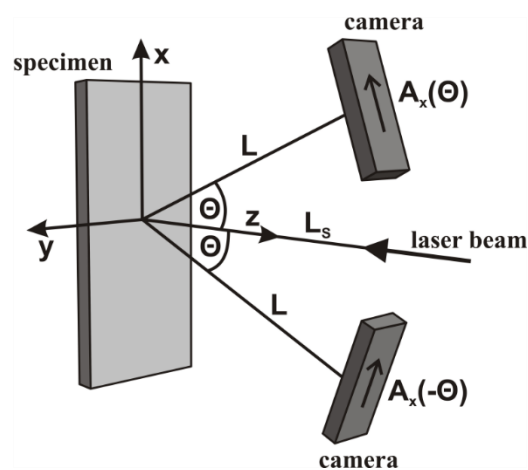

Fig. 3.13: Schematic of measurement set-up with laser beam, sample surface, and two line cameras [182].

When a slightly granual image is hit by the laser beam the light is dispersed in different directions and creates a granular looking called as speckle pattern. The principle of the strain calculation by the laser speckle method is based on the shift of the speckle pattern caused by displacement of the sample. The schematic of setup is depicted in **Fig. 3.13**. The laser beam is along z-axis is perpendicular to the sample surface (x-y plane). The line cameras are in x-z plane perpendicular to the incident light at a distance of L from the sample surface. A_x is the speckle displacement on the camera plane. Due to the fact that the video processor stores the initial speckle pattern as a reference, the shift of the speckle displacement (ΔA_x) during tension can be calculated by image correlation of the collected consecutive patterns. Then the strain value results as

$$\varepsilon_{xx} = \frac{\Delta A_x}{2L \tan \Theta} \qquad (3.27)$$

This strain calculation by laser speckle method is valid until the UTS is reached. These measured strain values are true strain (ε_T) type. The engineering strain is calculated by following the relation

$$\varepsilon = 1 - \exp(\varepsilon_T) \qquad (3.28)$$

where ε is the engineering strain.

After that necking starts leading to failure of the sample. At this particular point (during necking), the local measurement of the strain by laser speckle varies strongly as the focusing positions during necking changes randomly. Beyond the UTS, the true strain values are calculated from the crosshead movement. The engineering stress is estimated by the ratio of Force F and initial cross-sectional area A_0.
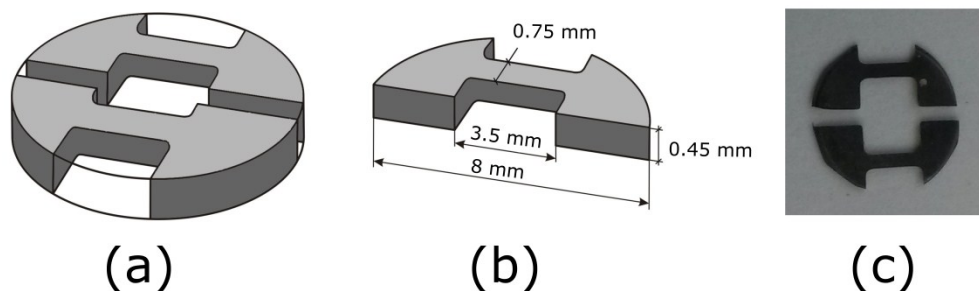

(a) (b) (c)

Fig. 3.14: Geometry of tensile test samples, adopted from [182]*: (a) schematic of two identical tensile test samples, (b) the sample dimension, and (c) HPT-4-10 tensile specimens (as an example) cut by spark erosion from the sample of 8 mm in diameter.*

In the case of Ti–45.0 Nb alloy, the micro-tensile specimens were prepared in dumbbell shaped (see **Fig. 3.14**) form by spark erosion with 0.75 mm width, ~0.45 mm thickness and a parallel gauge length of 2.5 mm. The tensile axis for the INI sample is parallel to extrusion direction ED (see **Fig. 3.2**). In the case of HPT, the tensile axis is parallel to shear direction SD. Tensile measurements were carried out at room temperature with a strain rate of 10^{-3} s^{-1}. For each of cases; INI sample and HPT three samples were tested and the average stress-strain curve was calculated. For R&F samples, tensile tests were not successful due to delamination of the sample.

3.12. Differential Scanning Calorimetry (DSC)

Differential scanning Calorimetry [184] (DSC) is a powerful technique widely used to study the thermal properties and phase transitions of the material in a controlled atmosphere. It measures the difference in the heat flow between the sample and a reference is recorded as a function of temperature. The reference sample is usually an inert material such as alumina (for experiments above temperature T > 600°C), or an empty aluminum pan (for T < 600°C). During the experiment, a sample is heated over a range of temperature and at some point the material may undergo a physical or chemical change that releases or absorbs the heat and this change is reflected in the heat flow curve. As the DSC is maintained at constant pressure, the time derivative of the heat flow is equal to the time derivative of the enthalpy and can be written as

$$\left(\frac{dq}{dt}\right)_p = \frac{dH}{dt} \tag{3.29}$$

where $H = M \times c_p \times \Delta T$, C_p is the specific heat in J/g K at constant pressure p, M is the mass of the sample in g, ΔT is the change in temperature in K.

On differentiation of **eq. 3.29**

$$\frac{1}{M}\left(\frac{dH}{dt}\right) = c_p \frac{dT}{dt} \tag{3.30}$$

Heat flow difference between the sample and the reference is

$$\Delta\left(\frac{dH}{dt}\right) = \left(\frac{dH}{dt}\right)_{sample} - \left(\frac{dH}{dt}\right)_{reference} \tag{3.31}$$

The heat flow can be positive or negative. For an endothermic process, the heat is absorbed. So the enthalpy of the sample is higher than the reference and hence the change in enthalpy becomes positive. For an exothermic process, the change in enthalpy becomes negative. In general crystallization, oxidation, decomposition reactions, and annihilation of defects are exothermic in nature.

Two types of DSCs are in common use [185]; heat-flux DSC and power compensated DSC. In heat-flux DSC, the sample and reference pan are connected by a low resistance heat-flow path and placed on a single furnace. The furnace is heated at a linear heating rate and the heat is transferred to the sample and reference pan. Because of different heat capacity of the sample and reference pan, there would be a temperature difference between them. This temperature difference are measured by using thermocouples and the heat flow is determined by the thermal equivalent of Ohm's law [185] (calibration using standard samples is necessary).

$$q = \frac{\Delta T}{R} \qquad (3.32)$$

where q is the sample heat flow, ΔT is the temperature difference between the sample and reference, R is the resistance of the heat path.

In a power compensated DSC [186] the sample and reference pans are placed on two separate heating furnaces. The temperature of the sample and the reference pans is maintained equal by varying the thermal power input between two furnaces. The equivalent energy difference is converted into the change in enthalpy and plotted as a function of temperature or time.

For this dissertation work, DSC measurements were carried out in Netzsch DSC204 (heat-flux DSC) and Perkin Elmer DSC 8500 (power compensated DSC) in the temperature range of RT to 550°C with standard heating rate of 10°C/min. In the case of Ti–16.1 Nb alloy, HPT processed samples were subjected to DSC to study the thermal stability of the HPT-induced phase and to determine the phase transition temperature. Additionally, partial isochronal heating experiments up to temperatures of 150, 250, 350, and 520°C were carried out and coupled with XRD diffraction experiment to determine the thermal stability of phases. The DSC measurements were not carried out for Ti–45.0 Nb, since the parent β-phase is stable upon SPD and up to an extended temperature.

4. Results

Parts of this chapter of "Results" mentioned are published in the international Journals. The details of these are found in the chapter "Bibliography" under the citations numbers [31,73,187].

4.1. Investigations of the alloy Ti–16.1 Nb

As shown in the **Fig. 2.11** [9,30] and **Fig. 8.1** the Ti–16.1 Nb alloy being close to the first lower minima in Young's modulus (about 65 GPa) it is selected for study aiming for suitability for biomedical applications. Now the goal is to enhance the mechanical strength Ti–16.1 Nb alloys. Therefore, this alloy was subjected to SPD methods such as HPT (application of severe plastic strain in combination with a high hydrostatic pressure) and R&F (application of severe plastic strain at a relatively low hydrostatic pressure). In addition, the samples were also subjected to hydrostatic pressure. The thermal stability of the HPT induced phases are studied with combination of DSC and XRD. To clarify the phase transition temperature in HPT processed alloy the samples were also subjected to in-situ heating experiments in the synchrotron facility at ESRF, Grenoble, France. In this work, the effect of hydrostatic pressure and SPD on the phase evolution and mechanical properties (E and H) are studied. The structural investigations were carried out by XRD, SEM, and TEM. The mechanical properties were investigated by nanoindentation and microhardness methods. The phase fractions in the alloys were determined by the Rietveld refinement technique.

4.1.1. Mechanical properties

The Young's modulus E and nanohardness H measured by nanoindentation, are summarized in **Table 4.1** and **Fig. 4.1**. The Ti–16.1 Nb alloy after water quenching (WQ) from the β-phase region at a temperature of about 1000°C shows the Young's modulus E = 66 GPa and nanohardness H = 1.9 GPa. With an application of hydrostatic pressure P of 4 GPa in HPT without rotating anvils the values H and E measured by nanoindentation increase by about 30% and 50%, respectively, than those of the WQ specimen. With increase of P from 4 to 8 GPa the values of E and H slightly increase to 93 GPa and 3.0 GPa, respectively. HPT-processed specimens exhibit rather high values of E and H. In the case of HPT-4-1 and HPT-4-5 (samples were denoted by HPT-P-N: P is the pressure in GPa and N is the number of rotations) the values of E = 106 and 129 GPa respectively and the values of H are 3.5 and 4.0

GPa respectively. A similar but less pronounced increase of E with strain is observed in the case of the specimens HPT-8-1, HPT-8-5 and HPT-8-10, whereas the value of H almost remains constant (about 3.8 GPa). Similar values of E (100 GPa) and H (3.3 GPa) were measured in the case of rolling and folding samples (R&F-5 and R&F-7). An isochronal annealing treatment to HPT-8-10 was carried out in DSC up to the temperature of 520°C (the sample is denoted HPT-8-10 + isochronal heating to 520°C). The measurement by nanoindentation shows E = 112 GPa and H = 3.2 GPa. The summary of the Vickers microhardness (HV) results is listed in **Table 4.1**. It is noticed that in the case of HPT samples the values obtained are 1.1–1.3 times higher than H values obtained from nanoindentation.

Table 4.1: Summary of the mechanical properties obtained from nanoindentation (E and H) for specimens WQ, HP, HPT, HPT + isochronal heating, and R&F. Values of were determined from 25 indents for each specimen as arithmetic averages including standard deviations. The values (Em) and (Hm) represent Young's modulus and Hardness, calculated by a rule of mixture using the values Ei and Hi values for pure phases (i.e. α, α', α", ω and β). The values of the Vickers microhardness (HV) were also presented (to compare with values of hardness H obtained from nanoindentation). The ε is the von Mises strain.

| Specimen	ε	E GPa	H GPa	E_m GPa	H_m GPa	HV GPa	HV/H
WQ	0	66 ± 4	1.9 ± 0.2	-	-	2.1 ± 0.1	1.1
HP-4	0.024	86 ± 5	2.8 ± 0.2	97	2.7	3.3 ± 0.1	1.1
HP-8	0.034	93 ± 11	3.0 ± 0.5	98	2.7	3.7 ± 0.1	1.2
HPT-4-1	24	106 ± 5	3.5 ± 0.3				
HPT-4-5	120	129 ± 4	4.0 ± 0.2	124	3.5	4.4 ± 0.2	1.1
HPT-8-1	25	118 ± 4	3.7 ± 0.2			4.6 ± 0.2	1.2
HPT-8-5	130	127 ± 7	3.7 ± 0.4			4.8 ± 0.2	1.3
HPT-8-10	296	130 ± 5	3.8 ± 0.3	-	-	4.8 ± 0.2	1.3
R&F-1	1.1	65 ± 11	2.3 ± 0.3	77	2.1	3.7 ± 0.2	1.7
R&F-3	3.3	72 ± 13	2.6 ± 0.4			3.8 ± 0.2	1.4
R&F-5	4.4	100 ± 7	3.3 ± 0.3			4.0 ± 0.2	1.2
R&F-7	6.0	99 ± 10	3.2 ± 0.5	110	3.1	4.4 ± 0.2	1.3
HPT-8-10+isochronal heating to 520°C	-	112 ± 3	3.2 ± 0.1	94	1.5	3.2 ± 0.2	1.0
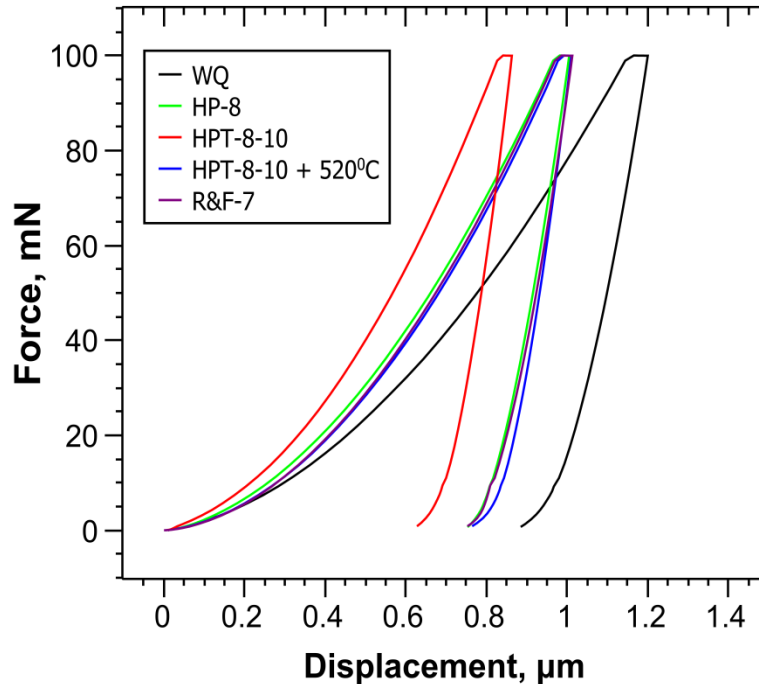
Fig. 4.1: Nanoindentation of specimens WQ, HP-8, HPT-8-10, HPT-8-10 + isochronal heating to 520°C and R&F-7. The force vs. displacement curve shows increasing values of H and E for specimens WQ to HP-8 to HPT-8-10 (qualitatively; the increase of E is evident from increase of the slope of the unloading curve increases and H increases as final displacement h_f decreases) while isochronal heating (HPT-8-10 + 520°C) causes a drop of both H and E.

4.1.2. Structural investigations

4.1.2.1. Standard diffraction patterns for phases

As already mentioned the Ti–Nb alloy system may exhibit four possible phases depending on stabilizing elements, heat treatments, quenching rate and deformation methods. The phases are α/α'-hexagonal, α"-orthorhombic, β-bcc and ω-hexagonal. To identify the presenting phase(s) in the Ti–16.1 Nb alloy before and after SPD standard diffraction patterns were constructed using literature values of the lattice parameters and atomic positions of the phases: α/α' (a = 0.2959 nm, c = 0.4703 nm [7], space group P6$_3$/mmc; the lattice structure of hcp α' is identical to that of α [32]), β (a = 0.3286 nm, space group Im$\bar{3}$m [34]), ω (a = 0.4647 nm, c = 0.2845 nm, space group P6/mmm; based on the (111) plane collapse model for the β → ω transformation $a_\omega = \sqrt{2}a_\beta$, $(c/a)_\omega = \sqrt{3/8}$ [19], α" (C-centered orthorhombic: a = 0.2989 nm, b = 0.5072 nm, c = 0.4698 nm, y parameter = 0.0181 nm, space group Cmcm [7,41]), depicted in **Fig. 4.2**.
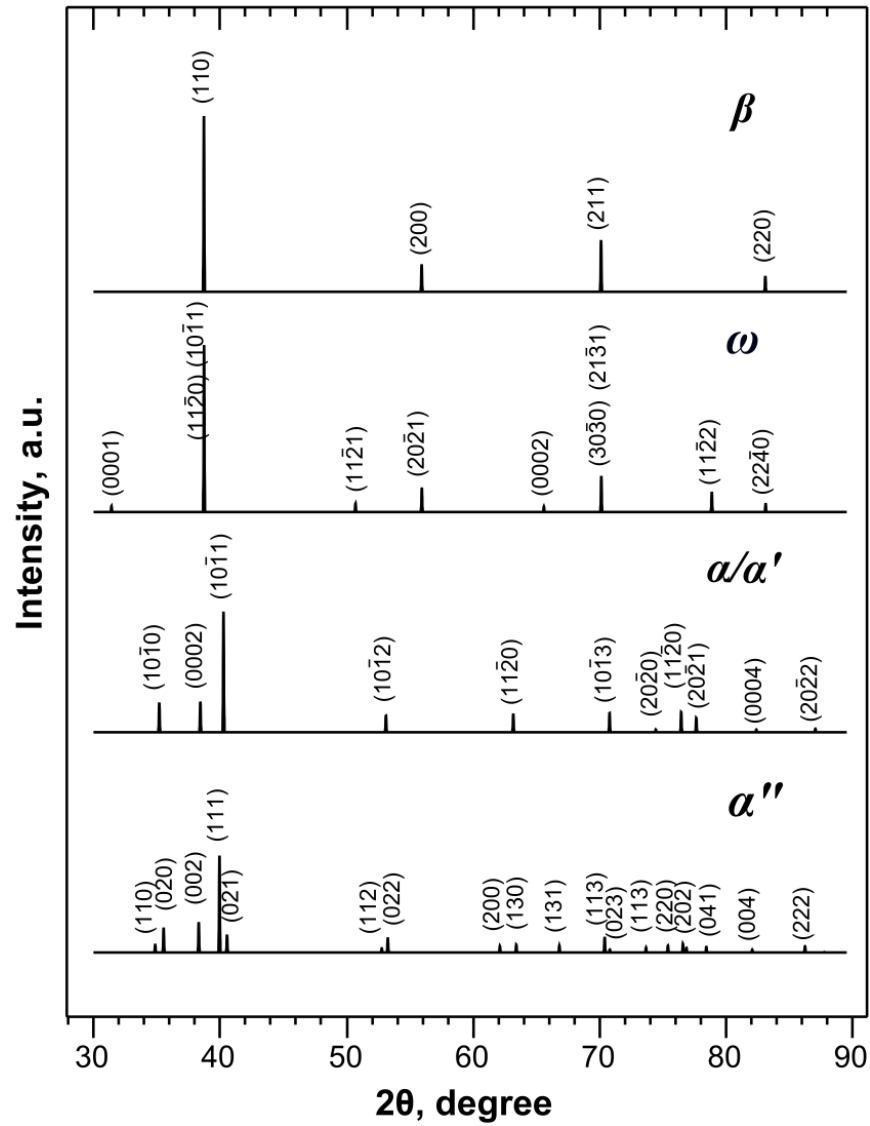
Fig. 4.2: Calculated XRD of Ti–16.1 Nb for bcc β, hexagonal ω, hcp α, hcp α' martensite, and orthorhombic α" martensite.

4.1.2.2. Ti–16.1 Nb before SPD

The phase analyses and microstructure of the WQ specimen were carried out by XRD and electron microscopy. The experimental XRD pattern of WQ specimen is illustrated in **Fig. 4.3**. Comparing the standard patterns shown in **Fig. 4.2**, the experimental pattern is indexed with orthorhombic α"- martensitic phase (it should be pointed out that there is a strong overlap between α/α' and α"-phases) as the splitting of reflections is seen, typical to α"-phase. As a splitting behavior, the doublets of the α"-phase such as $(110)_{\alpha"}$-$(020)_{\alpha"}$, $(111)_{\alpha"}$-$(021)_{\alpha"}$, $(112)_{\alpha"}$-$(022)_{\alpha"}$, $(200)_{\alpha"}$-$(130)_{\alpha"}$, as opposed to the single reflections $(10\text{-}10)_{\alpha}$, $(10\text{-}11)_{\alpha}$, $(10\text{-}12)_{\alpha}$, $(11\text{-}20)_{\alpha}$ of the α/α' phase is noticed because of lower symmetry in orthorhombic structure than hexagonal lattice structure, see **Fig. 4.2**. However, Rietveld refinement shows that the WQ alloy does not entirely contain α"-phase. A minor phase fraction of 9 wt.% of the α/α' phase (see **Table 4.2**). The SEM (FEG-SEM LEO1530 operated at 15 kV at IFW Dresden) investigations showed the within the range of 200–400 μm with acicular morphology of self-accommodated martensitic variants (see **Fig. 4.4(a)**). The analysis by TEM revealed a twinned morphology of the martensite (cf. **Fig. 4.4(b)**). The spot diffraction pattern agrees with a α"-martensitic structure (see **Fig. 4.4(c)**). However, a clear distinction of α" from the α/α'-phase is hardly achievable by TEM as the standard diffraction patterns of these lattice structures are very similar.

4.1.2.3. Ti–16.1 Nb subjected to hydrostatic compression and to SPD

A pure hydrostatic compression of P = 1 GPa without torsion in the HPT showed no phase change of α"-phase. While compression to P = 4 and 8 GPa caused the reflections corresponding to ω-phase (represented by open squares) to appear in addition to α"-phase (represented by solid reverse triangle), shown in **Fig. 4.3**. Some reflection's positions however could not be indexed unambiguously. These are indicated by a single asterisk in case they might correspond to either α" or α/α' lattice structure. Reflections that can arise by either the ω-phase, α" or α/α' lattice structures are indicated by a plus sign. Rietveld refinement of HP-4 sample yielded phase fractions of 36, 28 and 36 wt.% of the α"-, α/α'-, and ω- phase, respectively (see **Table 4.2**). With increase of P = 4 to 8 GPa intensity of α" reflections decrease and the phase fraction of the α" decreases to 20 wt.%.

Table 4.2: Phase fractions (wt.%) of selected specimens and corresponding value of agreement index R_{wp} obtained from Rietveld refinement.

Specimen	α"	α/α'	ω	β	R_{wp}
	wt.%				
WQ	91	9	-	-	17.3
HP-4	36	28	36	-	20.1
HP-8	20	30	38	12	21.9
HPT-4-5	-	9	86	5	8.1
HPT-8-10	-	1	99	-	7.2
HPT-8-10+isochronal heating to 520°C	-	78	-	22	7.2
R&F-1	62	16	20	2	22.7
R&F-7	22	9	65	4	22.3

XRD patterns after HPT processing at P = 4 GPa for N = 1 and 5 turns showed the presence of ω as major phase along with minor phase fraction of α/α' reflections, as illustrated in **Fig. 4.3** (for clarity XRD of HPT-4-5 is shown only). In the case of specimens processed by HPT with P = 8 GPa and N = 1, 5, 10 almost identical XRD patterns were obtained (the results of HPT-8-1 and HPT-8-10 are shown in **Fig. 4.3**) and almost all of the reflections correspond to the ω-phase. The Rietveld refinement yields the phase fraction of 99 wt.% for the ω-phase. However, the two peaks (indicated by arrows) cannot be identified in terms of the ω, β, α/α', α"-phases. From the present results it is concluded that HPT processing, with P ≥ 4 GPa and N ≥ 1 gives a complete transformation to ω-phase from α"-phase. **Fig. 4.4 (d)** and **(e)** show TEM micrographs after HPT-deformation (HPT-4-10). A complex contrast pattern is observed in the bright field image which is result of strongly fragmented grains and high dislocation density. Based on the analysis of several dark field images the heterogeneous microstructure was observed; larger fragments (average size of about 240 nm) containing subgrains with small misorientations (see e.g. A in **Fig. 4.4 (d)**) and small grains with an average size of about 70 nm were encountered (see e.g. B in **Fig. 4.4 (d)**). The small grains are leading to a ring-shaped diffraction pattern (shown in **Fig. 4.4 (f)**).

In order to examine the influence of the choice of the SPD-processing method R&F was carried out. **Fig. 4.5** shows the XRD patterns of R&F-processed specimens. The presence of corresponding to ω-phase can be seen even for R = 1 (ε =1.1) in addition to parent α"-phase. Rietveld analysis showed a fraction of about 62, 16, 20, and 2 wt.% of α", α/α', ω-phase and β , respectively, shown in **Table 4.2**. With increase of R to 3 (ε =3.3) the intensity of the ω-phase reflections arising increases and that of reflections corresponding to α" and

α/α' decreases. Further increase of the strain results almost no change in the XRD pattern. In the case of R&F-7 the ω-phase becomes the dominant phase (see **Table 4.2**).
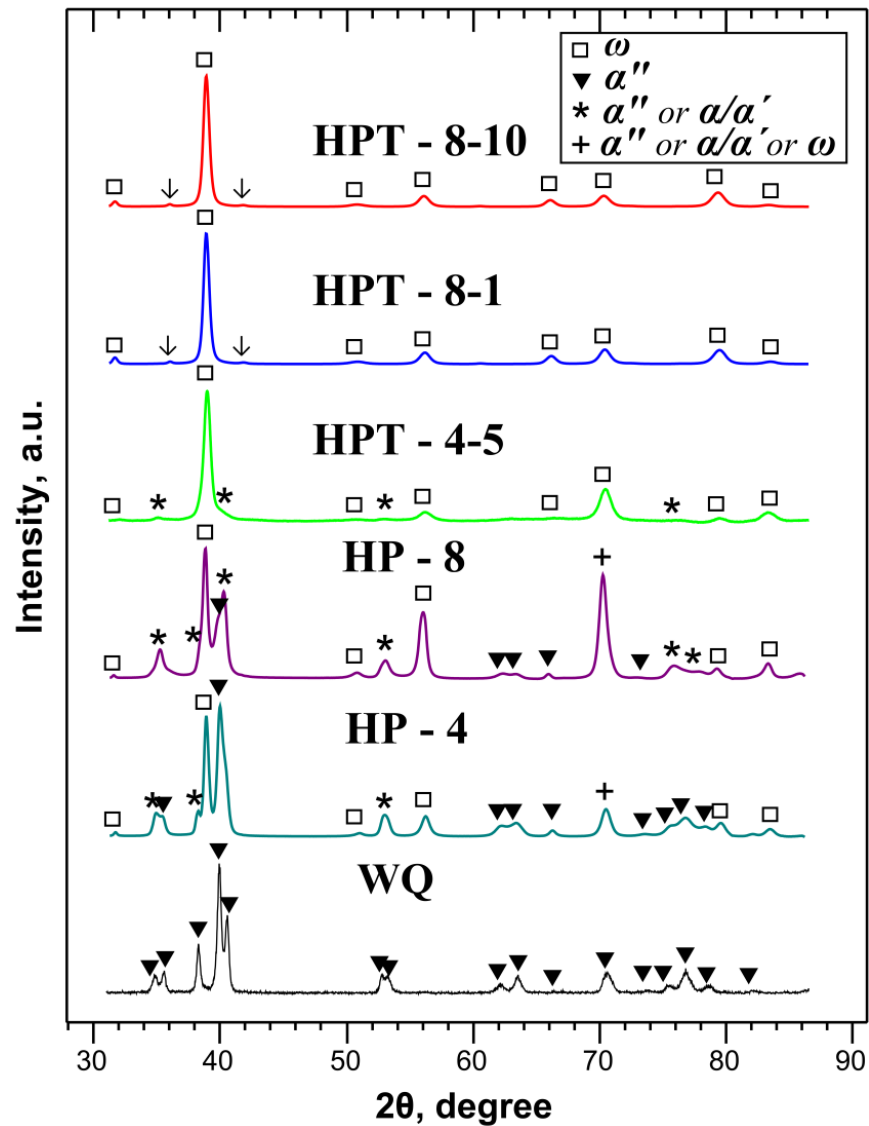

Fig. 4.3: XRD of specimens WQ, HP, and HPT. The WQ specimen contains the α" phase as the major phase. With application of hydrostatic pressure (HP-4, HP-8), the ω-phase starts to form. Shear strain in addition to hydrostatic pressure in HPT (HPT-4-5, HPT-8-1, HPT-8-10) results in the ω-phase as the single existent phase.
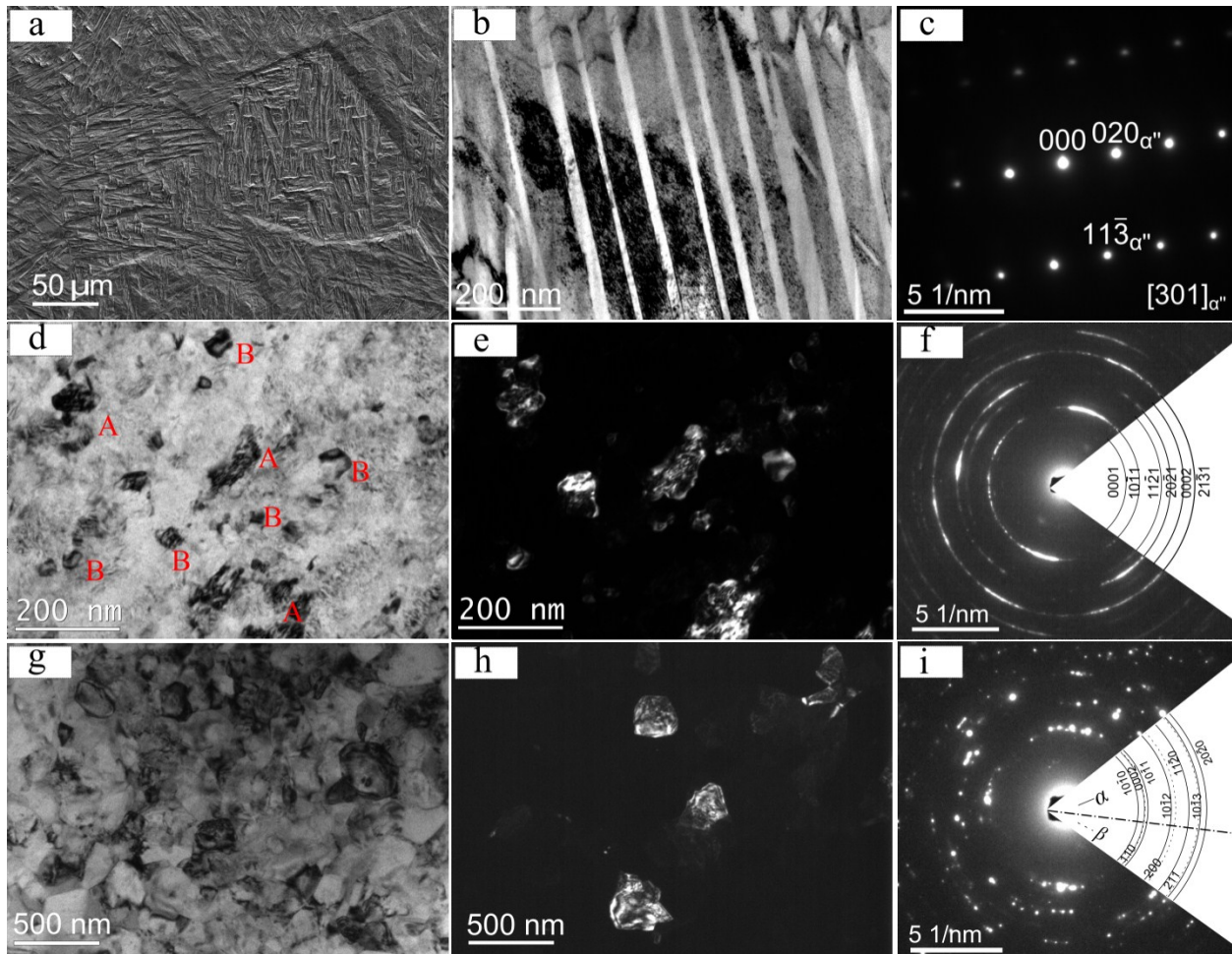
Fig. 4.4: Microstructure and corresponding diffraction patterns of specimens WQ ((a) – (c)), HPT-8-10 ((d)–(f)), and HPT-8-10 + isochronal heating to 520°C ((g)–(i)). SEM micrograph (a) shows coarse grains containing self-accommodated martensitic variants; BF image (b) shows martensitic twins; SADP shown in (c) agrees with that of α" phase. BF image (d) shows a complex contrast arising by overlapping grains and by strong lattice strains. Both larger grain fragments containing subgrains (e.g. A) and rather well defined nanograins (e.g. near B) are observed; the corresponding DF image (e); SADP shown as an in (f) agrees with that of the ω-phase. BF image (g) and corresponding DF image (h) shows ultrafine grains that frequently contain subgrain boundaries and isolated dislocations; the diffraction spots of the SADP shown as (i) agree with that of α+β phases.
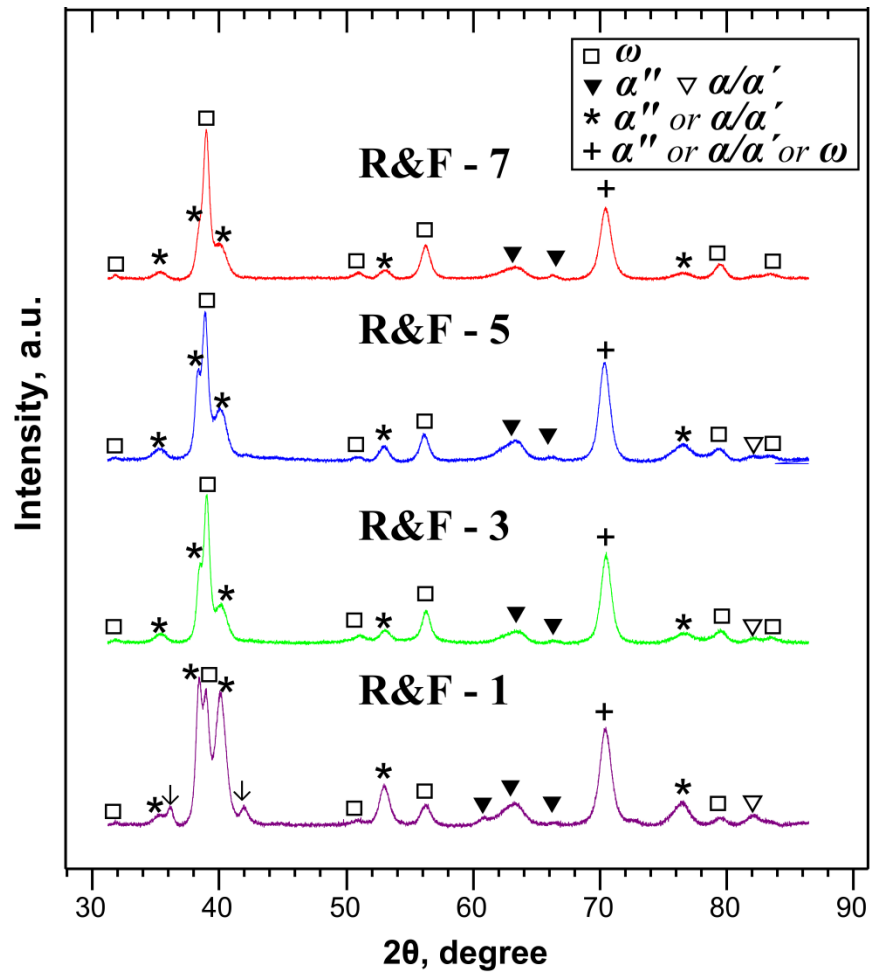
Fig. 4.5: XRD of specimens processed by R&F. The sample R&F-1 yields the formation of the ω-phase. Further increase of strain i.e. R&F-3 to R&F-7 the XRD patterns become almost identical and yields 65 wt.% of phase fraction of ω-phase.

In the case of R&F, it is noticed that even if the hydrostatic pressure is not larger than 1 GPa the formation of the ω-phase occurs. However, on contrary to HPT the ω-transformation is not complete in cases of R&F. Since the XRD of the HP-1-0 sample (hydrostatic compression P = 1 GPa) does not show any phase transformation, it can be concluded that in the case of R&F the ω-phase is induced by a combined effect of pressure and strain. Ti–16.1 Nb subjected to HPT followed by isochronal heating.

4.1.3. Thermal stability of HPT-induced ω-phase

To examine the thermal stability of the HPT-induced ω-phase the samples (HPT-8-10) were isochronally heat treated in DSC within a temperature range of RT to 550 °C utilizing heating and cooling rates of 10°C/min. This sample is denoted as HPT-8-10 + isochronal heating to 520°C. In the first heating run an endothermic reaction with a peak area of $\Delta H = 1.7 \pm 0.5$ J/g with an onset temperature of about 410°C and a peak temperature of about 455°C were observed (see **Fig. 4.6**). Further heating and cooling cycles did not show any peaks in DSC scans. Similar observations were noticed for all HPT-processed samples (in the case of HPT-4-5 and HPT-8-1 an endothermic peak of $\Delta H = 1.4$ J/g and 1.7 J/g at a temperature of about 450°C were observed, respectively).
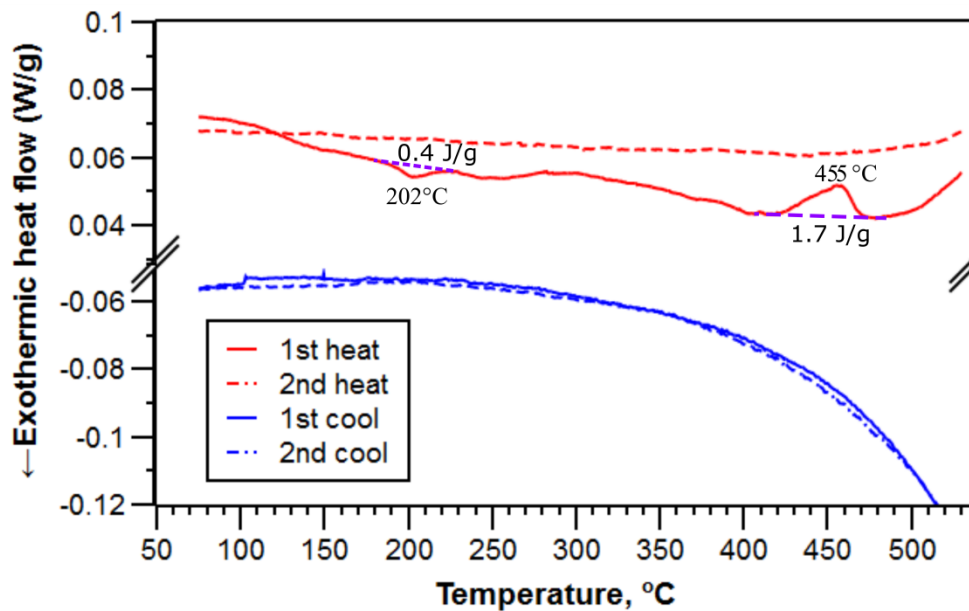

Fig. 4.6: Two heating and cooling scans of HPT-8-10 in DSC showing an exothermic peak at about 200°C (can be related to annihilation of defects) and an endothermic peak at about 455°C (related to phase transition of ω- to α+β- phase mixture).
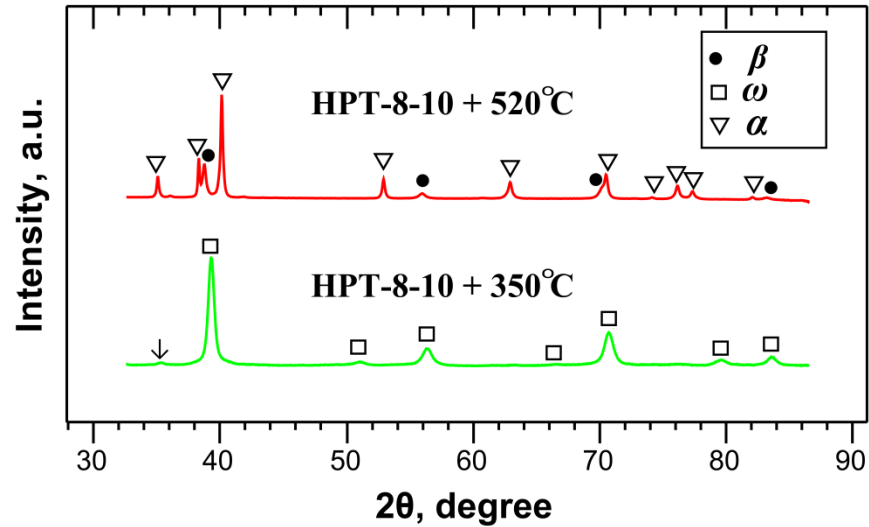
Fig. 4.7: XRD of HPT-8-10 subjected to isochronal heating. The isochronal heating to 350°C shows little changes as compared to the sample HPT-8-10 (see Fig. 4.3). Heating to 520°C (HPT-8-10 + isochronal heating to 520°C) causes the formation of equilibrium α and β phases.

The XRD measurements were carried out after partial isochronal heating to 150, 200, 250, 350 and 520°C in DSC. It was observed that the high pressure ω-phase is retained until 350°C, shown in **Fig. 4.7**. In contrast, isochronal heating to 520°C (i.e. above the finish temperature of the endothermic peak observed by DSC), results in disappearance of reflections of the ω-phase and the appearance of reflections from both α and β lattice structure. Analysis of the XRD pattern with Rietveld methods yielded a phase fraction of 78 wt.% α and 22 wt.% β. This indicates that the reverse transformation from metastable ω to equilibrium α and β phase occurs at around 410°C.

4.1.3.1. In-situ heating experiment at ESRF

To predict the exact starting temperature for the decomposition of the ω-phase in α- and β-phases a sample of HPT-8-10 was in-situ heat treated with synchrotron radiation from RT to 800°C with a heating rate of 10°C/min at ESRF facility. Some of the corresponding XRD profiles are shown in **Fig.** 4.7. It is observed that the ω-phase is stable until 300°C. XRD patterns in terms of phase fractions obtained by Rietveld analyses (see **Table 4.1**) and were compared to values obtained from the equilibrium phase diagram using Lever rule.

Exceeding a temperature of 300°C, the phase fraction of the ω-phase drastically drops (by about 40 wt.% in the temperature interval from 300°C to 320°C). However, the decomposition of the metastable ω-phase into equilibrium α-and β-phase mixture is complete at a temperature of about 460˚C (see **Table 4.1** and **Fig. 4.9**). With further heating the phase fraction of the β-phase gradually increases and is in good agreement with that of obtained from the phase diagram [28]. The α-phase fraction increases strongly up to a temperature of about 500°C opposing the trend expected from the phase diagram. These results suggest that most of the ω-phase fraction is consumed by α-phase up to a temperature of 500°C while the phase fraction of β is already close to its equilibrium value. At 500°C the ω-phase completely decomposed into α- and β-phase. At this point the phase fractions of α-and β-phases were estimated by Rietveld refinement and by equilibrium phase diagram show the similar values. Increasing the temperature up to 800˚C, the intensities of α-peaks continue to reduce and that of β-phase increases. This observation is also reflected in the phase fraction estimations (see **Table 4.1**). However, at temperatures > 500°C the phase fractions determined by Rietveld analysis deviate from their corresponding equilibrium values obtained from phase diagram i.e. the phase fraction of β gets lower while that of α is increasing than their equilibrium values.

TEM of HPT-processed sample after isochronal heating to 520°C reveals that the bulk nanocrystalline ω-phase transformed into an ultrafine equiaxed α/β microstructure (see **Fig. 4.4 (g)** and **(h)**). The SADP patterns shown in **Fig. 4.4 (i)** can be indexed in terms of α and β lattice structures.
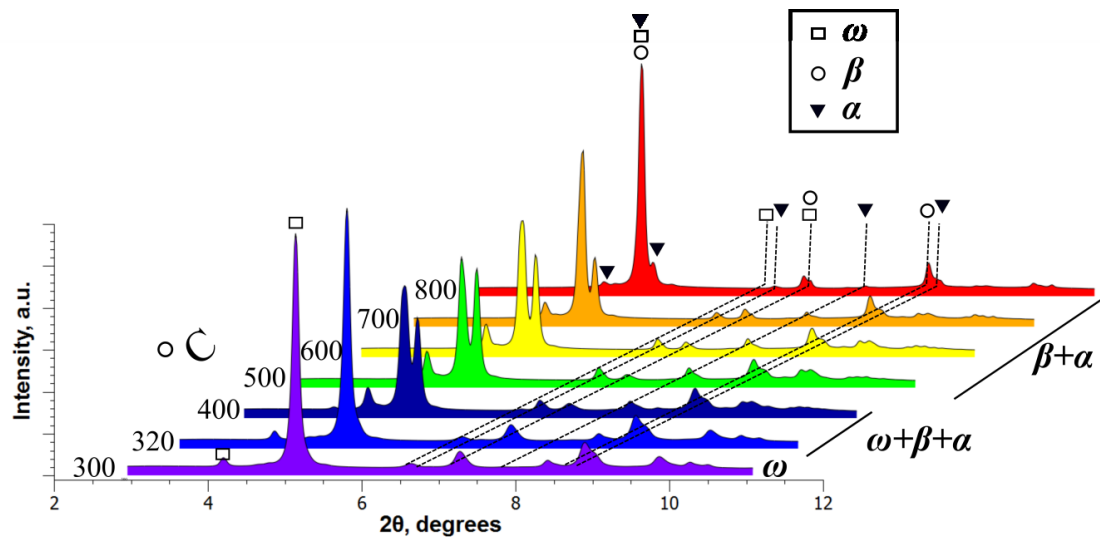
Fig. 4.8: XRD profiles of a HPT-8-10 obtained from in-situ heating synchrotron experiments. The symbols □, ○, and ▼ indicate reflections of the ω-, β-, and α-phase, respectively.
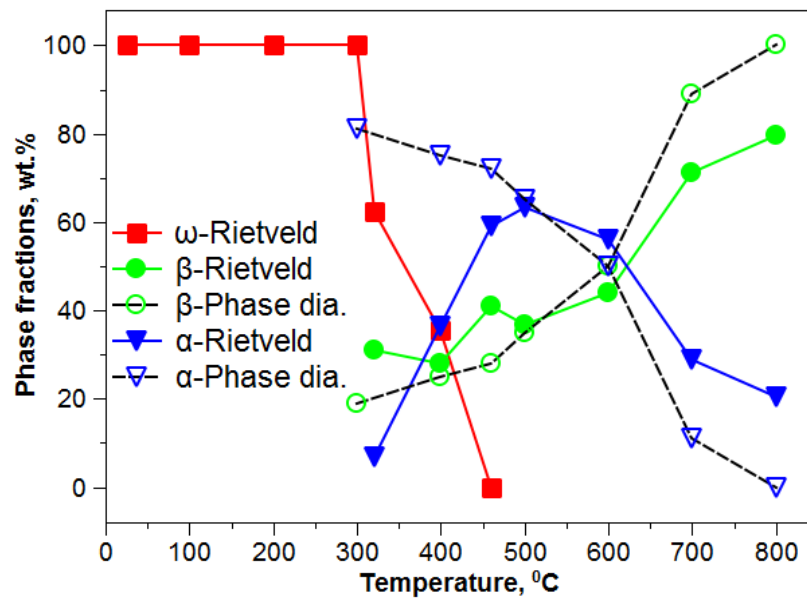
Fig. 4.9: ω-, α-, and β-phase fractions obtained from the experiment by Rietveld refinement (indicated by open symbols and full lines) and taken from the equilibrium phase diagram (indicated by full symbols and dotted lines).

Table 4.3: Phase fractions (wt.%) obtained using the Rietveld refinement procedure for HPT-8-10 in Ti–16.1 Nb alloy during in-situ heating. The quality of the Rietveld fit is given by the parameters R_{wp}.

Temperature (°C)	ω (wt.%)	β (wt.%)	α (wt.%)	R_{wp}
RT	100	-	-	7.21
300	100	-	-	5.68
320	62	32	6	6.55
400	36	28	36	8.01
460	-	42	58	9.04
500	-	36	64	7.28
600	-	44	56	9.93
700	-	72	28	9.32
800	-	80	20	11.47

4.2. Investigations of the alloy Ti–45.0 Nb

In this study, β- Ti–45.0 Nb was selected as its Young's modulus lies close to the local minimum of 65 GPa (see **Fig. 2.11** [9,30] and **Fig. 8.1**) in the Ti–Nb binary alloy system. The samples were taken for SPD processing as shown in **Fig. 3.2.** This work presents a detailed and systematic study of the mechanical properties (measured by nanoindentation, tensile test, microhardness), microstructure (carried out by optical microscope and TEM) and texture (by X-ray texture) of Ti–45.0 Nb alloy prior and after SPD (R&F and HPT) aiming to improve the mechanical properties by enhancing strength while maintaining a low Young's modulus. The CSD size and dislocation densities were measured by Convolution of Multiple Whole Profile method (CMWP) [163,164].

4.2.1. Mechanical properties

Table 4.4 and **Fig. 4.10** summarize the E measurements by nanoindentation, hardness measurements by Vickers microhardness tests. The value of E in the case of initial as-received sample (denoted by INI) was measured as 65 ± 3 GPa The R&F processed Ti–45.0 Nb samples showed a drop in the values of E from 63 ± 2 GPa down to 50 ± 2 GPa for R&F-1 to R&F-5, respectively. In the case of HPT processed samples, E remained within the range of 60–63 GPa, independent of degree of deformation.

The stress-strain curves of the INI and HPT processed specimens obtained from microtensile tests are shown in **Fig. 4.11**. The microtensile tests were not successful in the case of R&F samples due to delamination problem. The value of E of INI is 68 ± 3 GPa while in the case of HPT, the value of E is 66 ± 3 GPa. The values of E obtained from microtensile tests show a very good agreement with those of the nanoindentation measurements. The ultimate tensile strength (UTS) increased substantially from INI to HPT sample, from 446 ± 14 to 986 ± 7 MPa (almost twice the value of the UTS of samples prior to HPT processing). In the case of INI sample, the fracture strain is about 24 ± 2 %. The total elongation to failure is 14.0 % and 8.5% for HPT-4-1 and HPT-4-10 samples, respectively.

The INI sample shows the microhardness (H) value of 1.50 ± 0.04 GPa. In the case of R&F, the value increased to 1.88 ± 0.07 GPa for R&F-1 and increases only slightly with further increase of the strain (see **Fig. 4.10**). The most pronouncing hardening effect (65% increase compared to starting material) is seen in the case of HPT samples and the value gets saturated after N = 1.

Table 4.4: Summary of mechanical properties; Vickers microhardness H, Young's modulus E from nanoindentation as a function of von Mises strain ε and the calculated values of Young's modulus Ecalc obtained from the texture data (taken from [73]).

Samples	ε	Vickers Microhardness	Nanoindentation	Mechanical Compatibility	E-Calculation
		H, GPa	E, GPa	(H/E) x 100	E_{calc}, GPa
INI	0	1.50 ± 0.04	65 ± 3	2.3 ± 0.1	64
R&F-1	1.5	1.88 ± 0.07	63 ± 2	2.9 ± 0.4	60
R&F-3	3.0	1.89 ± 0.05	58 ± 3	3.2 ± 0.2	51
R&F-5	4.8	1.97 ± 0.11	50 ± 2	3.9 ± 0.3	52
HPT-4-1	15	2.40 ± 0.05	60 ± 2	4.0 ± 0.2	62
HPT-4-5	85	2.48 ± 0.09	62 ± 2	4.0 ± 0.2	63
HPT-4-10	170	2.47 ± 0.09	63 ± 2	3.9 ± 0.2	63

4.2.2. Structural investigations

4.2.2.1. Ti−45.0 Nb before SPD

XRD pattern taken from the INI sample is shown in **Fig. 4.12 (a)**. The diffractogram of the initial material shows the reflections corresponding to a single phase β matrix. The optical microscopy on the INI sample revealed equiaxed grains with an average grain size of 25 μm (see **Fig. 4.13 (a)**). The TEM BF image showed remained the dislocation structures after the hot hydrostatic extrusion (**Fig. 4.13 (b)**). The SAD pattern shows strong diffraction spots which agree well with that expected from β-phase with BD = [110] (see **Fig. 4.13 (c)**). In addition diffuse streaks running along the <112> directions as well as weak spots arising at the positions n/3<112> (with n=1, 2) elongated along <112> were observed, which corresponds to the ω-phase reflections.
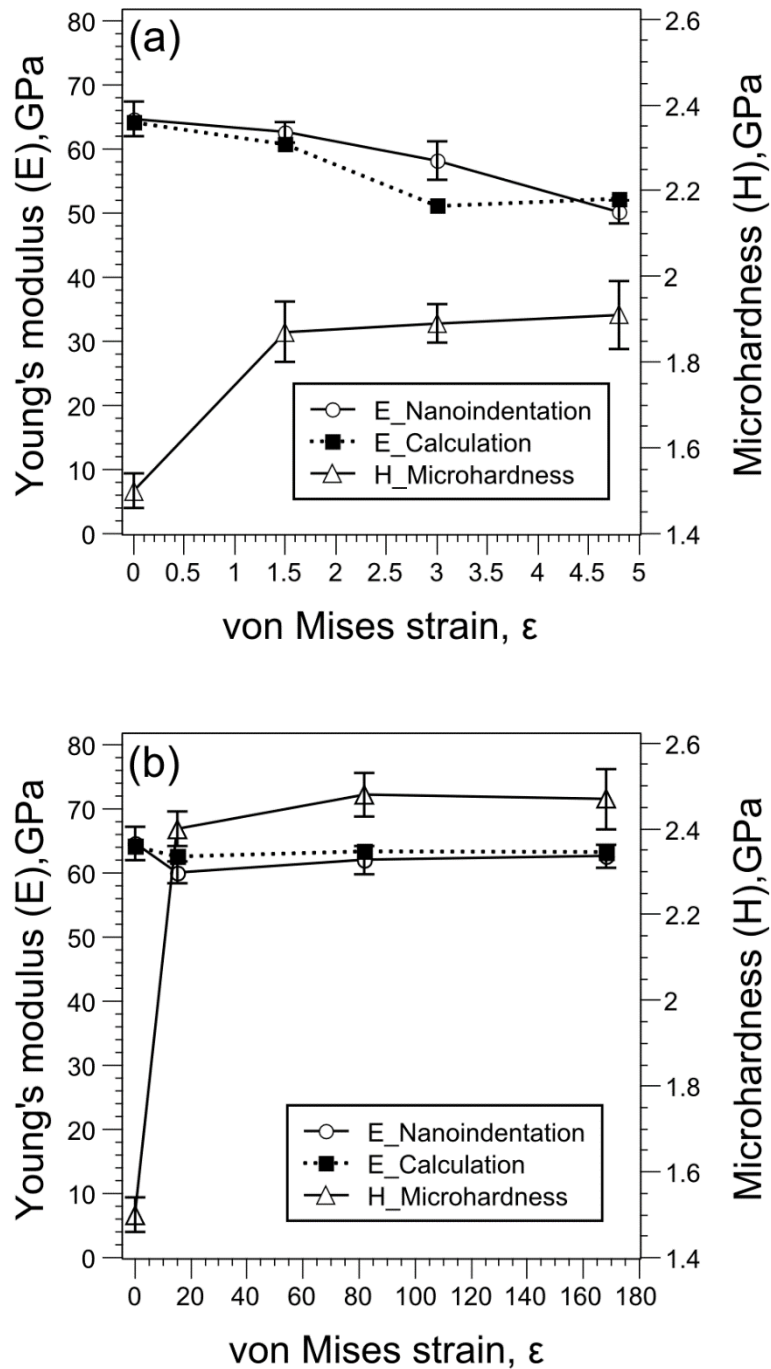
Fig. 4.10: Values of Young's modulus (E) and microhardness (H) obtained from nanoindentation and Vickers microhardness methods, plotted as a function of von Mises strain ε for (a) R&F, and (b) HPT samples. Based on texture data the Young's moduli (E_calculation) were calculated in [73], presented here for a comparison with measurements.
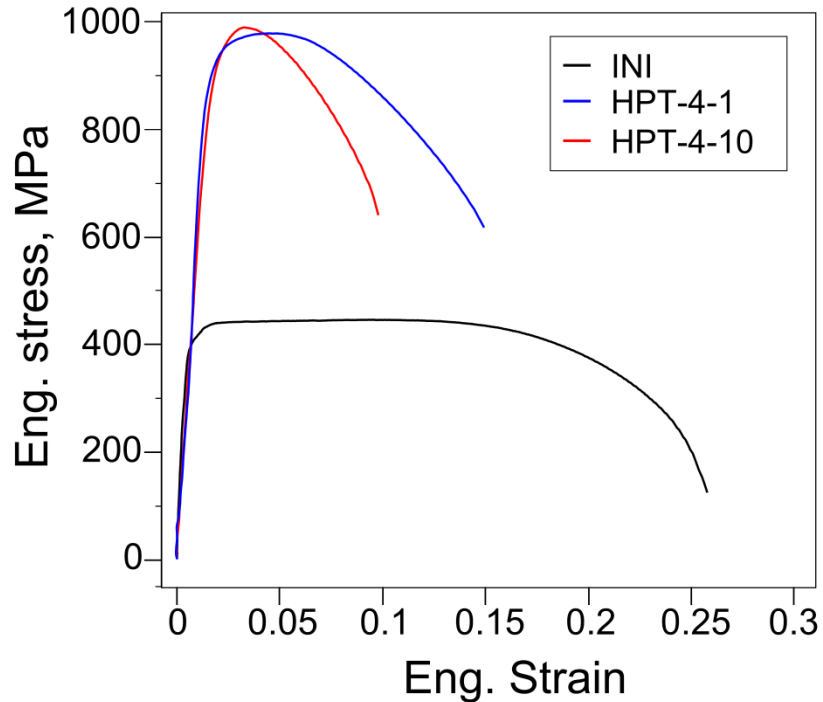
Fig. 4.11: Stress-strain curves for INI and HPT processed samples: UTS value increased from 445 (initial) to about 980 MPa (HPT-4-1: von Mises strain ε=15 & HPT-4-10: ε=170). Fracture strain decreases with increase of strain during SPD process.

4.2.2.2. Ti−45.0 Nb subjected to SPD

XRD patterns corresponding R&F and HPT processed samples are depicted in **Fig. 4.12**. All the reflections correspond to the β-phase. In the case of samples R&F-5, a heterogeneous microstructure is observed shown in **Fig. 4.14**: i.e. microcrystalline (top row) and ultrafine grained (bottom row). In the microcrystalline regions; grains exceeding a size of several microns are observed (see **Fig. 4.14 (a)**). The complex contrasts in TEM BF image are caused by lattice strains, Moiré fringes (indicated by M) and bend contours. **Fig. 4.14 (b)** shows a high density of SPD induced dislocations frequently forming tangles. Based on the SADP shown in **Fig. 4.14 (c)** it is concluded that the grains contain the β-phase. However, streaks running along <110> are a strong indication for a lattice modulation related to an inherent instability of the β-phase. In the ultrafine grained regions a lamellar structure of elongated grains (having an average width of about 150 nm and a length in the range of 0.5–1.5 µm) is observed. They are separated from each other by large angle grain boundaries (the grains are elongated along the dashed lines marked in the TEM DF image of **Fig. 4.14 (e)**). Each of the elongated grains contains subgrains with rather small relative misorientations. These lead to ring-like diffraction pattern in the SADP (see **Fig. 4.14 (f)**).

Fig. 4.15 shows TEM images corresponding to HPT-processed sample - HPT-4-10. The complex contrast pattern in (see **Fig. 4.15 (a)** and **(b)**) seen is caused by the severely deformed nanocrystalline grains. The grain sizes vary within range of 70–170 nm with an average of 90 nm. The nanocrystalline aggregate leads to a ring shaped diffraction pattern (see **Fig. 4.15 (c)**). The analysis of the SADP of HPT-4-10 by PASAD revealed that the peaks on the diffraction rings can be indexed in terms of the β-phase. However, some very weak diffraction spots were also encountered which correspond to the ω-phase.
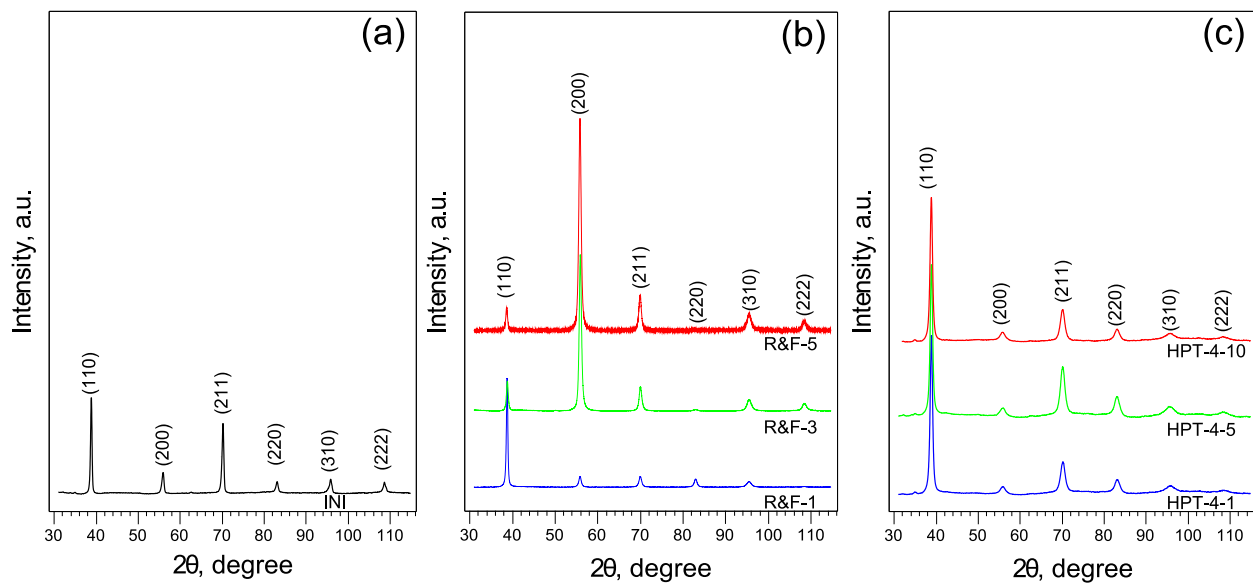
Fig. 4.12: XRD patterns of (a) INI, (b) R&F, (c) HPT processed samples: all the peaks correspond to β-phase representing the major phase.
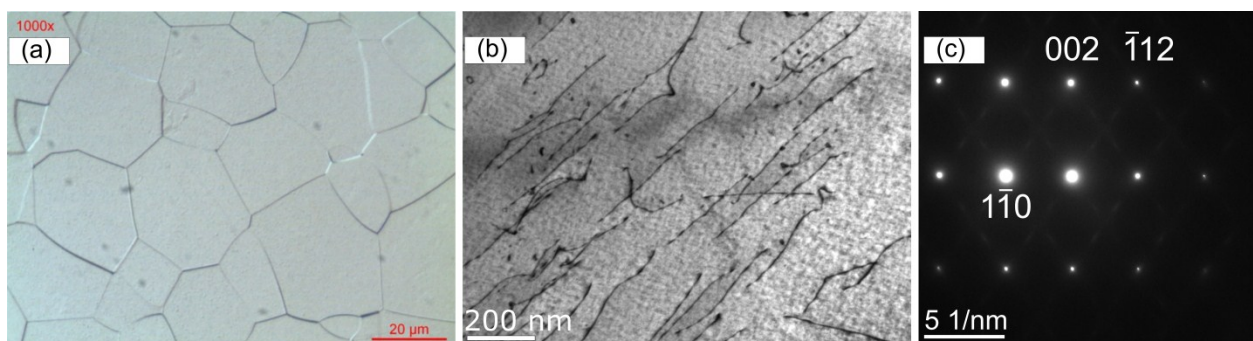
Fig. 4.13: INI sample: (a) Optical microscopy showing the equiaxed grains with average grain size of 25 µm, (b) TEM BF image showing dislocations, and (c) corresponding SADP pattern (BD = [110]), additional diffuse spots refer to the ω-phase.
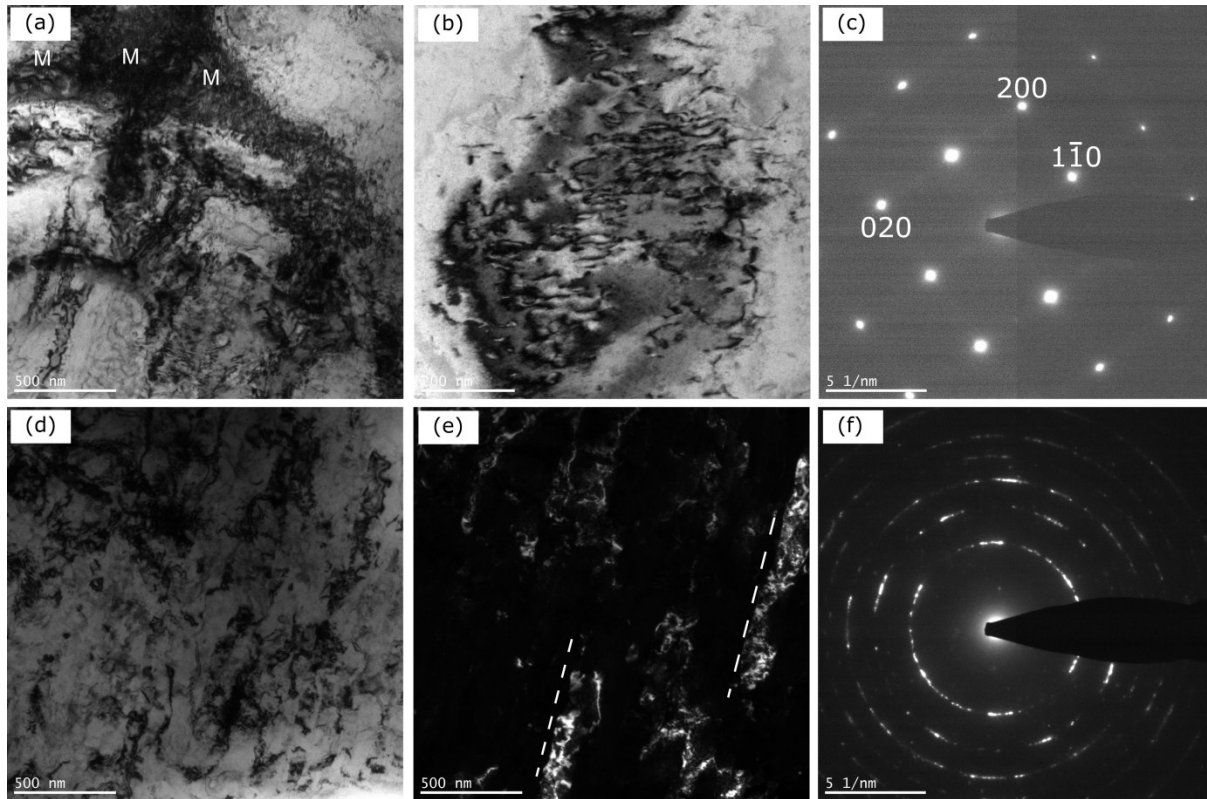
Fig. 4.14: The microstructure of samples R&F-5: microcrystalline region (top row) and ultrafine grained region (bottom row). (a) TEM BF image showing a rather complex contrast arising from bend contours, lattice strains and Moiré fringes (indicated by M). (b) TEM BF image of dislocation tangles. (c) SADP showing bright spots belonging to the β-phase; in addition, diffuse streaks are observed that run along <110> directions. **BD** = [001]. (d) TEM BF and (f) corresponding DF image showing elongated ultrafine grains. (f) Corresponding SADP: Strong rings correspond to the β-phase. However, some weak additional reflections are observed. Most of them can be indexed in terms of the ω-phase.
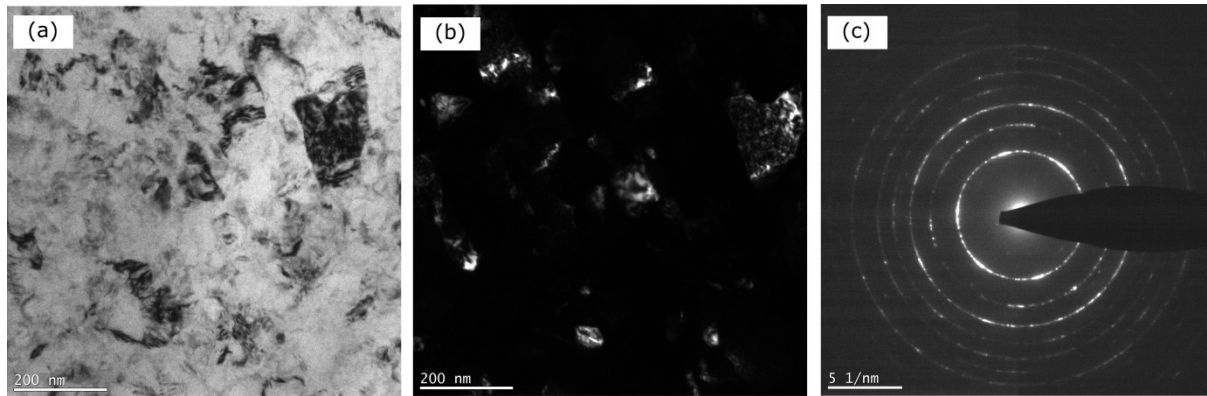
Fig. 4.15: Microstructure of sample HPT-4-10. (a) TEM BF image, (b) corresponding DF image showing nanocrystalline grains. (c) SADP showing strong diffraction rings that can be indexed in terms of β-phase. Some very weak reflections of the ω phase are also encountered.

4.2.3. Evolution of texture upon SPD

The variation in the relative peak intensities in the XRD patterns (see **Fig. 4.12**) can be attributed to changes in the crystallographic texture arising during SPD. In the case of R&F, the intensity ratio $I_{\{110\}}/I_{\{200\}}$ decreases substantially from about 9 to 0.1 with increasing number of rolling cycles R from 1 to 5. This indicates that {200} planes align preferentially parallel to the rolling plane. However, no specific trend in the relative intensities of diffraction peaks with the degree of deformation is seen for the samples subjected to HPT.

The texture of the INI sample shows a <110> fiber texture (**Fig. 4.16**), typical of bcc metals [188]. The corresponding pole figures are shown in **Appendix** section (cf **Fig. 8.2**). In the case of the starting material, <110> fiber also exists, however it is not complete as the sample was taken from the outer edge of the extrudate and therefore, locally it experienced a plane strain deformation similar to the case of rolling (known as cyclic fiber texture [189]. The texture intensity of the INI is 6.0 mrd (multiple of random distribution).
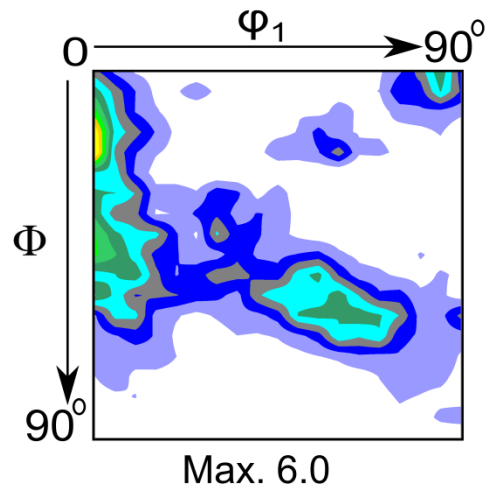
Fig. 4.16: $\varphi_2=45°$ ODF sections for INI sample The intensities are given in mrd. The Euler angle Φ is running across ED.

In the case of R&F samples, a rotated cube component {001} <110> developed, i.e. {001} planes and <110> directions are preferentially aligned parallel to ND and RD, respectively, together with a very weak γ-fiber texture (<111> parallel to ND), **Fig. 4.17**. The {001} <110> component gets strengthened with increase in R from 1 to 5 (i.e. with increase in strain from 1.5 to 4.8) while the intensity of the γ-fiber decreases. The corresponding pole figures are shown in the **Appendix** section (cf **Fig. 8.3**). The {001} <110> component gets strengthened with increase in R from 1 to 5 (i.e. with increase in strain from 1.5 to 4.8) while the intensity of the γ-fiber decreases.
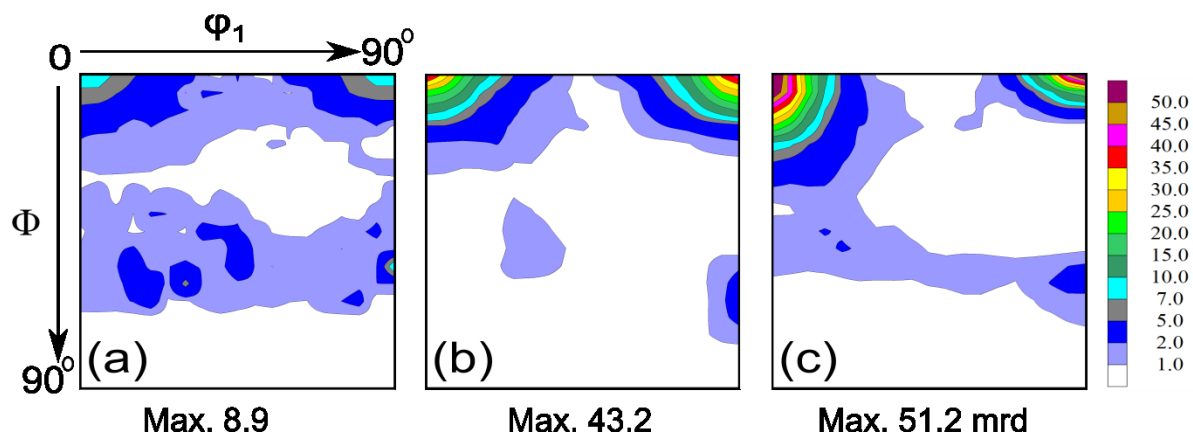
Fig. 4.17: $\varphi_2=45°$ ODF sections for R&F samples (a) R=1, (b) R=3, and (c) R=5. The Euler angles Φ and φ_1 are running across RD and ND, respectively.
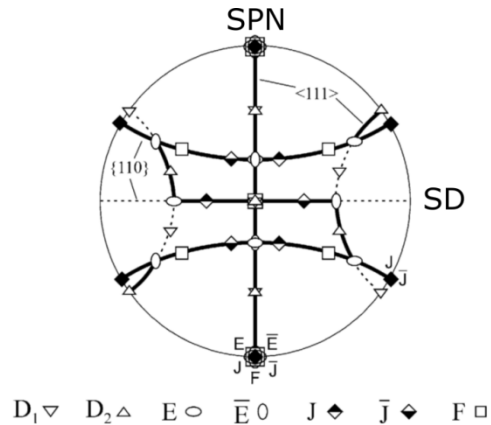
Fig. 4.18: {110} pole figure showing the main ideal orientations and fiber textures associated with the simple shear deformation of bcc materials, adopted from [190].

The texture measurements conducted at a radius of 2 mm of the HPT discs show a change from the initial extrusion fiber texture to a rather weak shear texture. The ideal orientations in simple shear deformation of bcc metals are shown in **Table 4.5** [191] and standard {110} pole figure (cf **Fig. 4.18**). From the ODF sections $\varphi_2=0°$ and $\varphi_2=45°$ it is clearly noticed that with increasing strain, the D_2 component, $\{\bar{1}\bar{1}2\}$ <111>, dominates (notation: {shear plane} <shear direction>). This fact corresponds to the alignment of the slip plane $\{\bar{1}\bar{1}2\}$ parallel to the shear plane and the Burgers vector <111> lies parallel to the shear direction. The intensity of this shear texture increased slightly with increasing strain while the intensity of F and $\bar{J}$ components decreased **(Fig. 4.19)**. The corresponding pole figures are shown in **Fig. 8.4.**
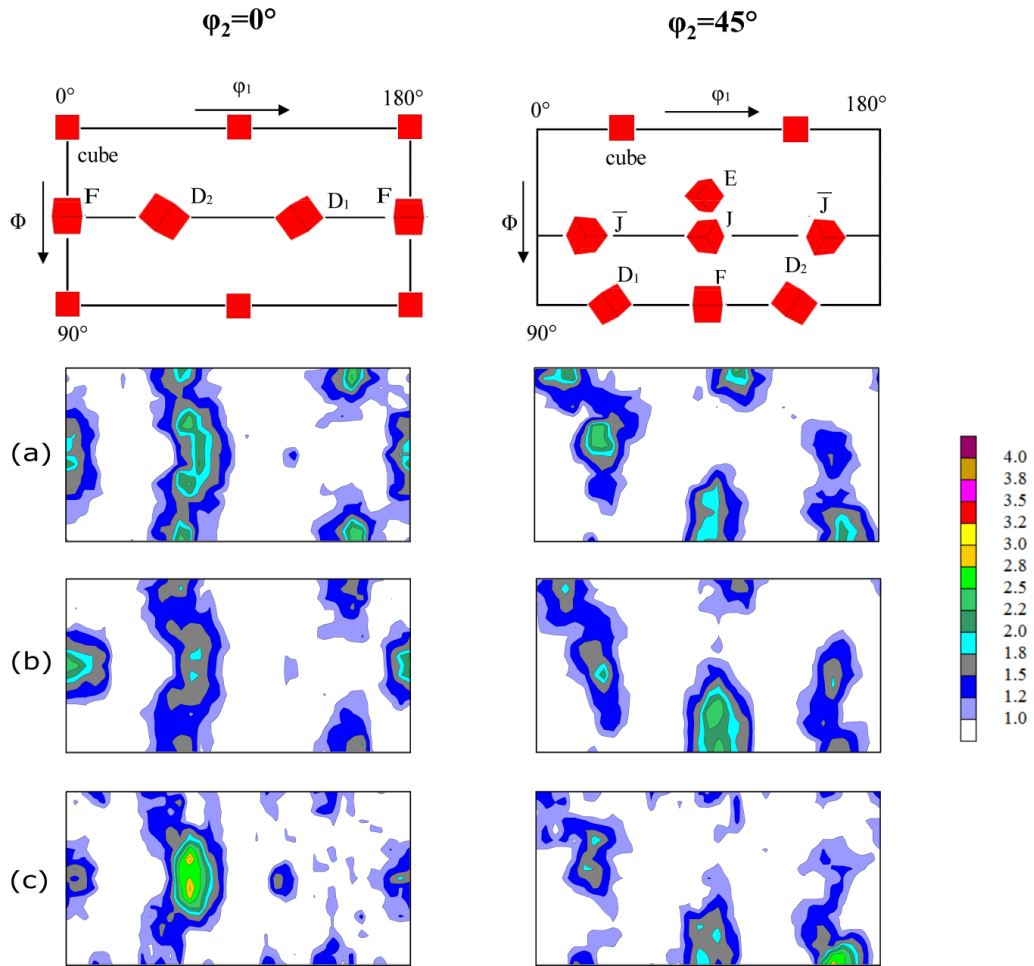
Fig. 4.19: φ_2=0° and φ_2=45° ODF sections for HPT processed samples (a) HPT-4-1, (b) HPT-4-5, and (c) HPT-4-10. The key figure above gives the ideal components of simple shear of bcc metals. The Euler angles Φ and φ_1 are running across SD and SPN, respectively.

Table 4.5: Main ideal orientations in simple shear deformation of bcc metals [191].

Component	Miller indices		Euler angles (°)		
	Shear plane	Shear direction	φ_1	Φ	φ_2
D_2	$\{\bar{1}\bar{1}2\}$	$[111]$	54.74	45	0
			144.74	90	45
D_1	$\{11\bar{2}\}$	$[111]$	125.26	45	0
			35.26	90	45
E	$\{110\}$	$[1\bar{1}1]$	90	35.26	45
J	$\{110\}$	$[1\bar{1}2]$	90	54.74	45
$\bar{J}$	$\{\bar{1}\bar{1}0\}$	$[\bar{1}1\bar{2}]$	30	54.74	45
			150	54.74	45
F	$\{110\}$	$[001]$	0/180	45	0
			90	90	45

4.2.4. Determination of the dislocation density from XLPA

It is observed that with increase of the von Mises strain ε there is a significant increase of the dislocation density as well as reduction in CSD sizes. (see **Table 4.6**). The high amount of the dislocation desnity is noticed for HPT-processed Ti–45.0 Nb alloy , however, the rate of increase of the dislocation density is higher in case of R&F compared to those of HPT. Also the severe grain refinement occurs during HPT because of high hydrostatic pressure in addition to high amount of torsional strain.

Table 4.6: Dislocation densities and CSD sizes measured by X-ray line profile analysis (CMWP-program) for SPD processed samples.

Samples	ε	Dislocation density ($10^{15}/m^2$)	CSD size (nm)
R&F-1	1.5	1.61 ± 0.15	65 ± 7
R&F-3	3.0	2.96 ± 0.28	63 ± 5
R&F-5	4.8	5.11 ± 0.61	53 ± 7
HPT-4-1	15	4.70 ± 0.44	55 ± 8
HPT-4-5	85	5.62 ± 1.29	33 ± 9
HPT-4-10	170	5.41 ± 0.71	27 ± 6

5. Discussion

Parts of this chapter of "Disscussion" mentioned are published in the international Journals. The details of these publications are found in the chapter "Bibliography" under citation numbers [31,73,187].

5.1. Discussion of the results of Ti–16.1 Nb

The SEM and TEM micrographs of WQ Ti–16.1 Nb presented in **Fig. 4.4** show groups of self-accommodated martensitic variants and martensitic twins, respectively. The TEM SADP agrees with that expected in the case of the α''-orthorhombic martensite. The XRD of WQ Ti–16.1 Nb (see **Fig. 4.3**) confirms the martensite corresponding to the α''-orthorhombic lattice structure. This result is in good agreement with the observations reported in the literature. It is known that the stability of the martensitic phases (α' and α'') in Ti–Nb alloys depends upon the Nb-content; lower Nb content promotes the formation of α'-martensite whereas α''-martensite formation is seen with relatively higher Nb-content. Moffat et al. mentioned that the transition boundary between α'/α'' occurs at 13.3 wt. % Nb [32]. A recent systematic study of Ti–Nb alloys also revealed that α'' is the main phase in Ti–16.1 Nb quenched from the single β-phase field down to room temperature [7,8,192]. As outlined in [31], Ti–13.7 Nb water quenched from the β-phase region shows almost entirely hexagonal α' martensitic phase. Based on these results it can be concluded that the transition of α' to α''-phase lies between 13.7 wt.% Nb and 16.1 w.% Nb.

The effect of hydrostatic pressure (1, 4, and 8 GPa) on the α''-orthorhombic martensitic structure of WQ Ti–16.1 Nb alloy is discussed as follows: Based on the results in **Table 4.2** the threshold pressure for inducing a phase transformation of the α'' martensite is in the range of 1 to 4 GPa. While the application of a pressure of 1 GPa does not affect the observed phase fraction of the α''-martensite, the increase of the pressure from 4 to 8 GPa the stability of α''-phase gets lowered (36 wt.% to 20 wt.%), and the formation of the ω-phase occurs at the expense of α''-phase (cf. **Fig. 4.3** and **Table 4.2**). This result also suggests that a hydrostatic pressure solely is sufficient to trigger the formation of the ω-phase. Also the presence of α/α'-phase indicates that a pressure induced α'' to α' transformation occurring either concomitantly or as a precursor for the formation of the ω-phase (see **Table 4.2**). A pressure induced ω-phase formation from α''-phase was reported previously [43,44]. Afonikova et al. mentioned that in the case of Ti–18 wt.% Nb alloy (exhibiting a mixture of α' and α''-phases) the threshold value of the pressure required for the onset and the completion of the ω-phase

is 3–5 GPa and >10 GPa, respectively [44]. The formation of ω-phase was also reported for α"-Ti–16.4 to 26.4 wt.% Nb with application of hydrostatic pressure of 8 GPa [43].

The present investigation, however, showed that a complete transformation to the ω-phase is also possible at lower hydrostatic pressure with the aid of a shear deformation, i.e. occurring by HPT, when P ≥ 4 GPa and N ≥ 1 (cf. **Fig. 4.3** and **Table 4.2**). In detail, the shear deformation decreases the necessary hydrostatic pressure for a complete ω-phase transformation from >10 [44] to 4 GPa. It is known that the presence of local stress concentrations can lower the pressure required for a pressure-induced phase transformation [193]. The martensitic structures in the initial WQ state may act as potential site for stress concentrators. Furthermore, the defects produced by HPT straining of the WQ specimen offer favorable nucleation sites along with the martensitic structures and thereby reduce the pressure required for the α"→ω transformation. As a main result, the combination of the HPT induced grain refinement and the HPT induced phase transformation can be used to obtain bulk nanocrystalline ω-Ti-Nb. Similar results on the formation of bulk submicrocrystlline ω-Ti [23,25] and ω-Zr [194,195] are reported. However, in the present case the thermal stability of the ω-phase (about 300°C, cf. **Table 4.3**) is considerably higher than that of reported in bulk ω-Ti (about 130°C [23,25]) and ω-Zr (about 210°C [194,195]).

R&F has been shown to promote the formation of ω-phase at hydrostatic pressure of about 1 GPa. This estimation has been based on (i) the measured value of the nanohardness H =3.2 GPa obtained by R&F process (see **Table 4.1**), and (ii) the relation UTS =1/3 H, and the relations P~URS~UTS [196], where URS and UTS denote the ultimate flow stress for rolling and ultimate tensile stress, respectively. Since a pure hydrostatic pressure of 1 GPa yields no phase change of the parent α"-martensitic phase, the occurrence of ω-phase in the case of R&F suggests that the ω-phase formation is affected by a combined effect of pressure and strain (cf. **Table 4.2**). However, contrary to the case of HPT the transformation is not complete. Mantani et al. reported the effect of cold rolling up to von Mises strain ε = 0.5 on Ti–15 and 20 wt.% Nb (containing pure α' and α", respectively) and observed no phase transformation [197]. Therefore it is concluded that rolling strains greater than 0.5 (in the present case ε ≥ 1.1) are necessary for the formation of the ω-phase. This means that there exists a threshold strain for the ω-phase formation at which a sufficiently high number density of the nucleation sites for the formation of the ω-phase is provided [198].

The DSC scans of HPT-8-10 results in the formation of an endothermic peak in first heating cycle (RT to 550°C with heat rate of 10°C/min) while further heating and cooling cycles did not show any signals (**see Fig. 4.6**). This is explained as follows: The HPT induced metastable ω-phase transforms to α and β-equilibrium phases during the first heating run. Since these are the equilibrium phases (cf. the α+β two-phase region of the equilibrium phase diagram [28,192]), no reactions were observed with further heating and cooling

cycles. The phase fractions obtained by the Rietveld analyses from the measured XRD patterns during in-situ heating experiment (RT to 800°C with heat rate of 10°C/min) on HPT-8-10 at ESRF show that most of the ω-phase fraction is consumed by the α-phase up to a temperature of 500°C while the phase fraction of β is already close to its equilibrium value after 400°C (see **Fig. 4.9** and **Table 4.3**). In the temperature interval from 300 to 320°C, the phase fraction of the ω-phase drops strongly (the rate is about 2%/°C that is ~40 wt.% with 20°C of heating). In this temperature interval, the β-phase strongly increases (with a rate of about 1.6%/°C). Contrary to that, the rate of the formation of the α-phase is rather low (about 0.3 %/°C). This picture changes for the temperature interval from 320 to 460°C. The disappearance of the ω-phase fraction (rate of 0.45%/°C) is almost equal to the formation of α-phase (rate of ~0.4%/°C). At 500°C the ω-phase has completely decomposed into α- and β-phase. Further heating to a temperature of 800°C shows that the phase fractions determined by Rietveld analysis deviate from their corresponding equilibrium values obtained from phase diagram i.e. the phase fraction of β gets lower while that of α is increasing than their equilibrium values (cf. **Table 4.3**). This result might indicate that applying a heating rate of 10°C/min during the in-situ experiment, the kinetics of the phase separation is not sufficient to achieve the thermodynamic equilibrium.

HPT-processing followed by isochronal heating to 520°C results in an ultrafine mixture of α and β-equilibrium phases (see **Fig. 4.4**). It should be noted that in the case of α/β Ti-based alloys like Ti–6Al–4V, various thermomechanical treatments were applied to obtain tailored morphologies (including lamellar, basketweave, globular, or Widmanstätten) in order to optimize mechanical properties; typical length scales of the these phase structures are in the range of several microns [199,200]. In the present case of Ti-Nb, the pathway via an intermediate nanocrystalline ω-phase provides a new processing route for the production of a bulk material with an ultrafine and equiaxed α/β phase structure.

The mechanical properties obtained are results of the phase fractions, microstructure, and dislocation density. It should be noted that the values of the mechanical properties can also depend on the way they are measured. For an example, the mechanical strength obtained by microhardness (HV) and nanohardness (H) differ. This discrepancy is clearly observed in the **Table 4.1**, which can be related to the mode of indent's area measurements. In the case of nanoindentation estimation of hardness is based on the contact area measurement under load while in microhardness indent's area is measured from residual imprints after unloading [180] (calculating diagonal lengths of the indent in optical microscope). The indent area relaxes during unloading in the microhardness case and therefore causes an increase in hardness value. In the case of R&F-1 the ratio of HV/H is 1.7 and it drops to the 1.3 (same as that of HPT) with increase of strain. In the case of HPT-8-10+isochronal heating case this ratio is found to be 1.

Based on the present results summarized in **Table 4.1**, both elastic and plastic hardening occur with increasing hydrostatic pressure. Hardening is further improved by strain applied in addition to hydrostatic pressure. However, for the samples HPT-8-N, the value of the Young's modulus already shows a strong tendency to stabilization since there is only a weak dependence on deformation strain. Based on the analysis of the XRD diffractograms by Rietveld refinement methods (cf. **Table 4.2**) a clear dependence of the measured values of E on the phase fractions is observed. A similar phase fraction dependence of H is also encountered. However, for H, in addition to the phase fractions also effects of strain hardening and Hall-Petch hardening have to be considered. This is outlined comparing the experimental values of E and H with those obtained applying a rule of mixture: $E_m = \sum_i f_i E_i$

and $H_m = \sum_i f_i H_i$ where E_i and H_i denote the Young's modulus and hardness, respectively, of a pure phase (i.e. either α, α', α", ω or β). The f_i denote the volume fraction of a pure phase in a mixture of phases with average Young's modulus and hardness given by E_m and H_m, respectively. It should be noted that in the case of E the rule of mixture corresponds to the Voigt average and therefore, to an upper limit [201]. Reference values of E and H were taken for pure phases. In the case of the ω-phase E_ω = 130 GPa and H_ω = 3.7 GPa were obtained from the alloy HPT-8-10 containing single phase ω. It is worth to notice that similar values were also reported in the case of CP Ti subjected to HPT (P = 5 GPa and N = 10) containing bulk single ω-phase [24,25]. Values for the pure α"-martensite ($E_{\alpha"}$ = 63 GPa and $H_{\alpha"}$ = 1.8 GPa) were calculated. Taking the experimental values of E and H of the initial Ti–16.1 wt.% Nb WQ alloy (containing a mixture of α" and α'-martensite), the calculation was carried out using E_m = 66 GPa, H_m = 1.9 GPa of the phase mixture with $f_{\alpha"}$ = 0.91, $f_{\alpha'}$ = 0.09 ($E_{\alpha'}$ = 97 GPa, $H_{\alpha'}$ = 2.5 GPa were taken from the Ti–13.7 wt.% Nb reference alloy containing single phase α'-martensite [192], see Appendix chapter, **Fig. 8.1**). Reference values for pure α taken from the literature were E_α = 100 GPa [6,10] and H_α = 1.56 GPa [71] (measured for CP Ti) [9,66] and that of β were E_β= 65.5 GPa and H_β = 1.45 GPa [29] (measured for Ti–40 wt.% Nb).

Based on the nanoindentation results (cf. **Table 4.1** and **Table 4.2**) a clear dependence of the values of E on the phase fractions is observed. A similar dependence in H is also encountered. For H, in addition to phase fraction the effects of strain hardening and Hall-Petch hardening can also be realized. Applying the rule of mixture, E_m and H_m were calculated for HP-4, HP-8, HPT-4-5, HPT-8-10 + isochronal heating to 520°C, and R&F-7 (cf. **Table 4.1**). In the case of E_m a good agreement between calculation and experiment is obtained. As a general trend an increase of E with increasing pressure and strain is noticed. This is attributed to the increasing phase fraction of the ω-phase on the expense of α"-phase. The sample HPT-8-10 + isochronal heating to 520°C containing a α/β phase shows a similar value of E as that of ELI-Ti–6Al–4V alloy [6,10].

In the case of H, the values obtained by the calculation are in good agreement with those obtained by the experiment. However, it should be noted that the reference value H_ω = 3.7 GPa of the pure ω-phase was measured for the alloy processed by HPT and therefore is expected to include effects of high defect density and grain-refinement. This is not the case for the reference values of H for the pure phases α, α', α", and β obtained from undeformed materials. A special case seems to arise in the case of the hardness of HPT-8-10 + isochronal heating to 520°C since the measured value (3.2 GPa) is more than twice as large as the calculated value. This is explained by a Hall-Petch type hardening arising from the ultrafine α/β phase mixture obtained after HPT followed by isochronal heating and presence of non-annihilated defects.

In the current work Ti–16.1 Nb in WQ state showed the values E = 66 GPa and H = 1.9 GPa. Processing the material through SPD enhances the strength quite substantially; however, E also increases because of ω-phase formation (eg. applying HPT the E value increased by two times). Therefore, it affects the mechanical biocompatibility adversely and limits the use of SPD processed T–16.1 Nb for load-bearing orthopaedic applications. On the other hand HPT followed by isochronal heating results in the formation of an ultrafine α/β phase mixture with an E value quite close to that of Ti–6Al–4V [6,10,71] and commercial pure Ti [71] while showing similar ($H_{Ti-6Al-4V}$ = 3.3 GPa [84]) or superior hardness (H_{Ti} = 1.5 GPa [71]) . Thus ultrafine α/β Ti–16.1 Nb alloy shows some potential to be used as substitute for CP-Ti and Ti–6Al–4V.

5.2. Discussion of the results of Ti–45.0 Nb

Based on the XRD patterns (see **Fig. 4.12**) taken from INI, R&F, and HPT processed samples, it is concluded that Ti–45.0 Nb shows a single-phase β structure. However, using the results of the TEM SADP diffraction experiments a more complex situation arises. Firstly, the presence of a minor volume fraction of the ω-phase is evident from the SADP of the samples INI (**Fig. 4.13(c)**) that show streak like diffuse scattering running along <112> directions as well as weak spots arising at the positions n/3<112> (with n = 1, 2) in addition to strong reflections of the β-phase. Both of them represent the presence of nanoscale domains of the ω-phase resulting from the short-range-correlated displacements during the collapse of (111) planes [19,202]. Secondly, streaks running along cubic <110> directions observed in samples R&F (c.f **Fig. 4.14(f)**) are a strong indication for a lattice modulation related to an inherent instability of the β-phase [203]. Thirdly, in the case of the sample HPT some weak fundamental reflections of the ω-phase were observed. Recently many investigation works have been carried out in coarse grained β Ti–Nb binary alloys that allow to determine the critical concentration of Nb up to which diffuse scattering related to formation of the ω-phase arises [30,203,204]. Todai et al. observed the ω-phase-scattering for Ti–43.5 wt.% Nb whereas for Ti–44.7 wt.% Nb it was not encountered even by cooling to a temperature of –173℃. In the present case a slightly higher amount of 45.0 % Nb, the ω-phase related diffuse scattering occurs even at RT. Similarly, Hanada et al. reported diffuse ω-phase scattering in Ti–45.0 wt.% Nb while it almost completely disappears for a Ti–52 wt.% Nb alloy.

It is well known that SPD affects the phase stability. E.g. in the case of coarse grained Ti–16.1 Nb containing the α" martensite at RT, a pronounced SPD induced transformation to a nanocrystalline ω-phase was observed [31]. Samples of Ti–16.1 Nb subjected to similar conditions of R&F and HPT as in the present case of Ti–45.0 Nb showed a substantial amount of the ω-phase after SPD (e.g. phase fraction of 65 and 86 wt.% ω-phase was obtained in R&F-7 and HPT-4-5 samples of Ti–16.1 Nb). However, in the Ti–45.0 Nb alloy changes in the phase structures are hardly detected using methods of XRD and TEM. This is due to the presence of high amount of Nb stabilizing the β-phase and therefore, suppressing the deformation induced formation of the ω-phase [205].

With respect to the Young's modulus it was reported that in the case of Ti–V alloys the minimum of E occurs for a composition at which already weak scattering (using XRD, TEM) of the ω-phase is observed [81]. Similarly in the case of Ti–45.0 wt.% Nb the weakly scattered intensity corresponding to the ω-phase are indications of a minimum of E in the Ti–Nb alloys (see **Fig. 2.11**). Based on the calculations of the Young's modulus from the texture data (taken from [73]) it is noticed that the measured values of apparent Young's modulus show a very good agreement (see **Table 4.4**). The INI sample shows a <110> fiber

texture. In the case of R&F a strong rotated cube texture {001} <110> is seen. This texture component {001}<110> is commonly observed in bcc β-Ti alloys after rolling [62,206,207]. Besides this, {112} <110> and {111}<112> components can also be seen as a result of high cold rolling strain or recrystallization [132,208–210]. The type of texture evolution is strongly dependent on the stability of the β-phase. It has been reported that Ti alloys with relatively low β-phase stability subjected to rolling show {112}<110> and {111}<112> textures while in Ti alloys with higher stability {001}<110> becomes the main rolling component [210]. Based on $\overline{Bo}$ (bond order) - $\overline{Md}$ (metal d-orbital energy) diagrams [211], the value of $\overline{Bo} = 2.88$ and $\overline{Md} = 2.46$ for the Ti–45.0 Nb alloy suggests that the alloy lies in the stable β-phase region [211,212]. Thus, the main texture component is the rotated cube component. The calculation of Young's modulus from the texture data [73] also show a very good in agreement with measured values. Therefore it is concluded that the drop in apparent Young's modulus from 64 to 50 GPa is a result of texture. In the case of the β-phase in Ti alloys, the elastic modulus $E_{<hkl>}$ is lowest measured along the [001] direction; its value increases in the order of $E_{<001>} < E_{<011>} < E_{<111>}$ [62,77,132]. As the nanoindentation measurements were carried out on the strongly textured R&F alloys with a rolling plane preferentially orientated along {001} crystallographic planes of the grains, this also explains a drop of apparent Young's modulus by nanoindentation. A similar effect of decreasing Young's modulus with high rolling reduction in the range of 50–89% was also observed in Ti–35Nb–4Sn alloy [213]. This decrease was, however, explained by the development of stress induced α" orthorhombic martensite showing a {200}$_{α"}$ <010>$_{α"}$ rolling texture. This rolling texture of the α" crystal structure corresponds to a rolling texture of {001} <110> in the β-phase. In the present case of HPT a relatively strong extrusion texture changes to rather weak shear texture. Textures in torsion are generally weaker than those in axisymmetric or plane strain deformation, because in torsion there are no stable orientations. As the grains continuously rotate, they slow down in rotation speed towards stationary positions in orientation space, whereas they strongly accelerate after they have passed these positions [188,214]. However, the particularly weak texture observed here seems to be a consequence of the pronounced HPT grain refinement down to the nanometer scale which leads to smoothing of the texture [215], but most importantly due to a larger contribution of grain boundary mediated processes, e.g. grain boundary sliding [216]. Since in the case of HPT, the texture is quite weak and so the contributions of texture towards the value of E is seemingly less, the values of E is almost identical to those expected from the isotropic polycrystals of Ti–45.0 wt.% Nb (about 65 GPa, [9]).

The increase of the UTS value from the INI sample to HPT (P= 4 GPa, N=1 & 10) (see **Fig. 4.11**) can be explained by Hall-Petch hardening which results from severe grain refinement and work hardening which occurs by the increase in dislocation density (see **Table 4.6**). Total elongation to failure in the case of INI sample is 24 ± 2 %. In the case of HPT, the values of total elongation to failure are 13 % and 8 ± 2 % for HPT-4-1 and HPT-4-10 samples,

respectively. Recently, a UTS value of 1020 MPa and a Young's modulus of 56 GPa were reported in the case of Ti–38 wt.% Nb subjected to cold rolling (von Mises strain $\varepsilon = 2.4$) and annealing at 400°C [217]. In comparison to the present case of samples processed by HPT, this UTS value is slightly higher and the Young's modulus is lower. The lower Young's modulus may arise from the rolling texture as it is noticed in the present case. Also, the fracture strain in cold rolled and annealed Ti–38 wt.% Nb alloy is considerably lower (about 4.6 %) in comparison to the present case of Ti–45.0 wt.% Nb alloys subjected to HPT (≥ 8 %). This demonstrates that almost the same high strength at a markedly larger ductility in combination with a moderate value E can be achieved by HPT, in comparison with the results of [217]. This considerable ductility acieved by HPT can be attributed to low-strain rearrangements and/or annihilation of dislocations upon the release of the high hydrostatic pressure [212, 213].

Finally, the mechanical biocompatibility of the alloy was determined by percentage of strength (i.e. microhardness) over Young's modulus ((H/E) $\times$ 100). The higher this ratio, the more suitable the material is for biomedical applications. From **Table 4.4** it is noticed that in the case of INI sample this ratio in percentage is 2.30 ± 0.12 %. In the case of the R&F samples, the ratio increases from 2.98 ± 0.14 to 3.94 ± 0.27 % with increasing strain because of a decrease of the apparent value of E as result of a strongly rotated cube texture and a slight increase of strength from 1.88 ± 0.07 to 1.97 ± 0.11 GPa. In the case of HPT, the ratio percentage increases because of strengthening effects due to grain refinement and work hardening. Comparing the value of H for the different SPD methods, a strong strengthening effect (65% increase with respect to the INI sample) is observed in the case of HPT processed samples. While keeping the Young's modulus almost the same, the H/E ratio increases to about 4.0 %, i.e. to a very high value as compared to the other SPD methods. The H/E ratio for commercially used orthopaedic materials such as pure Ti and Ti–6Al–4V (Ti64) is $\sim$2.0 % and 3.1%, respectively, using corresponding values of H and E ($H_{Ti} = 2$ GPa and $H_{Ti64} = 3.4$ GPa [84], $E_{Ti} = 102$ GPa, $E_{Ti64} = 110$ GPa [10]). In the present case of R&F and HPT processed Ti–45.0 Nb, the values of H/E are markedly higher than those of the already commercially used orthopaedic alloys. Thus, it can be concluded that HPT and R&F processing provide an excellent combination of high strength and low Young's modulus and therefore have a great potential for application as biomaterials.

6. Summary and Conclusions

This thesis investigated the impact of the hydrostatic pressure and SPD on the phase stability and mechanical properties of biocompatible Ti–Nb alloys. In particular, the Young's modulus E of the alloys was of considerable interest since a low value of E close to that of cortical bone suggests the application of Ti–Nb as a material for orthopaedic implants. Since the value of E strongly depends on the Nb content, two different compositions were selected showing minimum values of E: Ti–16.1 Nb and Ti–45.0 Nb. The phase structure and fractions of the alloys induced by different thermo-mechanical treatments were analysed by TEM and XRD applying Rietveld refinement methods. The thermal stability and the phase decomposition of the HPT induced structures were analyzed in detail by in-situ heating experiments using synchrotron radiation. In addition, the texture evolutions in Ti–45.0 Nb with respect to SPD were studied and the effects of the texture on the Young's modulus E were investigated. Dislocation density and coherent domain size were measured by X-ray line profile analysis (XLPA). In the following the results and conclusions of the thesis are summarized.

(i) Ti–16.1 Nb

Water quenched sample showed peaks corresponding to the α''-orthorhombic martensitic structure. The grain sizeof these samples was in the range of 200-400 μm, containing a fine structure corresponding to groups of self-accommodated martensitic variants. Upon application of hydrostatic pressure P of 4 and 8 GPa the ω-phase and α'-phase form at the expense of the parent α'' lattice structure. Applying HPT, a complete transformation to the ω-phase occurs at a pressure P≥4 GPa. The ω-phase formed is stable at room temperature. Applying R&F, reflections corresponding to the ω-phase arise in addition to reflections of those of the parent α''-lattice structure. However, the phase transformation to the ω-phase is not complete even for rather high strains (R=7, von Mises strain ε of 6.0).

TEM of HPT processed samples subjected to N=10 rotations at pressure P = 8 GPa (von Mises strain ε=296) showed a heterogeneous microstructure with an average grain size of 70 nm. In agreement with the XRD measurements, TEM selected area diffraction pattern (SADP) also revealed that the samples entirely contain the ω-phase. Therefore, bulk nanocrystalline single phase ω-TiNb alloys were obtained by HPT.

To determine the thermal stability of the HPT–induced bulk ω-phase, in-situ heating experiments of HPT-processed samples (P = 8 GPa, N = 10) were carried out using synchrotron radiation. During heating from RT to 800°C. the ω-phase is stable until a

temperature of 300°C. Afterwards the ω-phase starts to decompose into α- and β-equilibrium phases. The decomposition is complete at a temperature of 460°C. It is seen that in the temperature range of 320 to 500°C, the weight fraction of the α-phase increases at the almost the same rate as ω-phase decreases while the phase fraction of the β-phase to the equilibrium values is constant as expected from phase diagram. At a temperature of 500°C, the ω-phase has completely decomposed into the α- and β-phase. The phase fractions of the latter are in good agreement with those indicated by the the phase diagram. With further heating, the phase fraction of the α-phase decreases and that of the β-phase increases, again in qualitative accordance with the phase diagram. Quantitatively, however, as compared to the equilibrium phase fractions, the increases of β and decreases of α with increasing temperature are smaller, thus representing an increasing difference to the equilibrium values. This result indicates that applying a heating rate of 10°C/min during the in-situ experiment, the kinetics of the phase separation is not sufficient to achieve the thermodynamic equilibrium. All these results obtained with the HPT processed and isochronically heated samples were confirmed by SADP patterns done within TEM investigations. The latter also exhibited equiaxed ultrafine grains.

Nanoindentation measurements on water quenched Ti–16.1 Nb alloy yielded the Young's modulus E and nanohardness H, as equal to 66 GPa and 1.9 GPa, respectively. The low value of E is due to the presence of an almost entire volume fraction of α"-phase in agreement with the results in the literature. The HPT-processed specimens exhibit rather high values of E and hardness. In the case of HPT-8-10 (P=8 GPa, N=10), an E of 130 GPa and a nanohardness of 4.0 GPa was observed. As compared to the undeformed alloy containing the elastically soft α"-martensite, the deformation induced increase of the Young's modulus is caused by a complete phase transformation to the ω-phase. A part of the increase of strength can be attributed to microstructural changes induced by severe grain refinement, according to corresponding Hall-Petch strengthening, and to work hardening by an increased defect density. In the case of the sample HPT followed by isochronal heating to 520°C, measurements of E and H by nanoindentation yielded values of E = 112 GPa and H = 3.2 GPa. Almost identical values of E (about 100 GPa) and H (about 3.3 GPa) were measured in the case of R&F-5 and R&F-7. The Young's modulus of the alloy processed by the different thermomechanical treatments was successfully modeled in terms of phase fractions applying a rule of mixture.

As a main result, HPT induces the formation of bulk nanocrystalline ω-phase in Ti–16.1 Nb alloy. High hydrostatic pressure (P >10 GPa) and HPT at relatively low pressure (P =4 GPa) causes the complete phase transformation from α" to ω-phase. Therefore, it can be concluded that a part of sufficient hydrostatic pressure required for a complete phase transformation is replaced by the shear strain in HPT. HPT followed by isochronal heating at 520°C yields a bulk Ti–Nb alloy with an ultrafine α/β phase structure. Upon the application of HPT the Young's modulus E increases to 130 GPa (almost twice to that of the initial water quenched alloy) because of the formation of the high modulus ω-phase. Therefore, it adversely affects the mechanical biocompatibility for the implant applications (the maximum of the Young's modulus of the bone is 40 GPa). Hence HPT is not suitable for obtadisng load bearing orthopaedic applications in Ti–16.1 Nb aloy. On the other hand, R&F and HPT followed by isochronal heating show an E value of 100 and 112 GPa, respectively, close to that of conventional orthopaedic alloy Ti–6Al–4V (E =110 GPa) and commercial pure Ti (E = 100 GPa) while exhibiting similar or superior strength H of 3.3 GPa in comparison with Ti–6Al–4V (H= 3.3 GPa) and CP Ti (H= 1.5 GPa). Thus ultrafine α/β Ti–16.1 Nb alloy or R&F- Ti–16.1 Nb show some potential to be used as substitute for CP-Ti and Ti–6Al–4V in orthopaedic applications.

(ii) Ti–45.0 Nb

The initial coarse grained Ti–45.0 Nb containing equiaxed grains with an average size of 25 μm shows values of the Young's modulus E = 65 GPa and microhardness H =1.5 GPa, pertaining to β-phase with a minor volume fraction of the ω-phase. Upon severe plastic deformation, a major phase fraction is still remained as β-phase. However diffuse streaks in TEM selected area diffraction pattern suggest that minor volume fraction of the ω-phase exists also with application of SPD.

The Young's modulus of samples is almost unaffected by HPT. Contrary to that, in the case of R&F samples, the E value drops from 65 to 50 GPa with increasing strain, i.e. number of rolling cycles R from 1 to 5. As SPD does not induce a phase change in this Ti–45.0 Nb alloy, the drop of E is suggested to arise from R&F specific texture changes which has been confirmed by simulations based on measured textures [73] The initial undeformed sample shows a <110> fiber texture. In the case of samples subjected to R&F, a strong rotated cube component {001} <110> develops, and the strength of this texture component increases with increase of von Mises strain ε from 1.5 to 4.8. In the case of HPT, only a rather weak texture develops. The D_2 component {$\bar{1}\bar{1}2$} <111> becomes stronger with shear strain, while J {110} <1$\bar{1}$2> and F {110} <001> components get weaker.

Nevertheless, the HPT processed sample showed the most pronounced strength increase (100%) paired with considerable ductility of 8 %. The strength increase is caused by significant grain refinement and increase of dislocation density, and gets saturated already after one rotation N=1 (ε =15). Comparing the mechanical biocompatibility (given by the percentage ratio of H/E) it is seen that final stage of R&F (R&F-5) and all HPT samples exhibit similar values of about 4.0. This indicates that these SPD processed samples have great potential to become a new candidate for biomedical applications.

7. Outlook

In this work, the effect to SPD processing on biomedical Ti–Nb alloys (Ti–16.1 Nb and Ti–45.0 Nb) was analyzed with the aim to enhance the mechanical properties i.e. maintaining the already rather low Young's modulus while substantially increasing the hardness. In the case of the Ti–16.1 Nb, this aim could not be achieved due to the inherent instability of the material with respect to a pressure and strain induced formation of high modulus ω-phase However, severe plastic deformation was applied at room temperature only. It would be interesting to investigate systematically the effect of temperature and the SPD instrinsic strain rate on the phase stability and the mechanical properties. Also the thermo-mechanical treatments prior to SPD and their effects need to be studied. Recently, it has been reported in the β Ti-alloy Ti–36Nb–2.2Ta–3.7Zr–0.3O that with sufficiently high torsional strain in HPT the ω-phase can be completely be suppressed, because of severe grain refinement [137]. Therefore, experiments should be undertaken to decide whether or not a similar effect could be found in the case of Ti-Nb alloys with torsional strains being much higher as those applied within the present work.

8. Appendix

8.1. Mechanical properties as a function of Nb content

The Ti–Nb alloys with nominal Nb contents (14, 16.5, 19, 21.5, 24, 26.5, 29, 31.5, 36 and 45) wt.% were received from IFW Dresden as a part of collaboration work with Mag. M. Bönisch, IFW Dresden. These alloys were prepared using a cold-crucible casting device. Afterwards these were subjected to homogenization in the single β-phase field at a temperature of about 1000^0C for 24 hours followed by water quenching (WQ). Nanoindentation experiments were performedwith a Berkvoich indenter using ISO14577 standard module (mentioned in "Nanoindentaion" section).
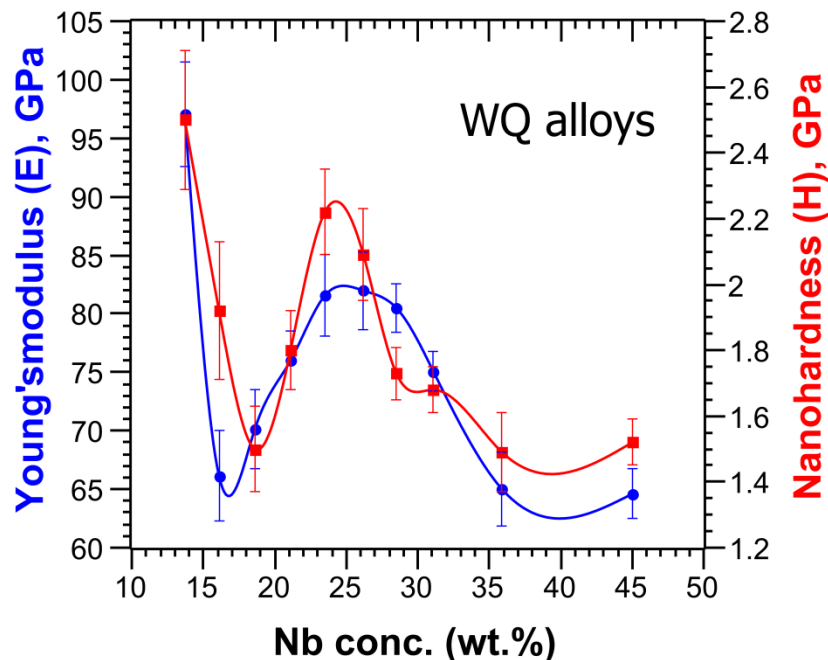

Fig. 8.1: Compositional dependence of Young's modulus E and Nanohardness H in several Ti– Nb binary alloys.

It is observed that the E and H values follow a w-shaped curve. The maximum value of E = 97 GPa is observed for Ti–14.0 Nb alloy at which the main phase is found to be hexagonal α'-martensite. The next maximum in E is observed in the range of 24–29 wt.% Nb (the main phase is α"-orthorhombic martensitic phase [192]). The minimum value of E ~ 65 GPa is found at about 16.5 wt.% (α"-phase) and 45 wt.% Nb (β-phase). The increase of the Young's modulus in the region of 26–30 wt.% Nb was reported to be caused by the presence of some

fraction of high modulus ω-phase in addition to α"-phase or metastable β-phase [4,80]. Beyond 31 wt.% the Young's modulus decreases as the phase fraction of metastable β increases [80]. The β-phase gets stabilized with Nb content >37 wt.% [80]. Afterwards up to 45 wt.% the E shows minimum values owing to low values of elastic constants and beyond that the E increases as the Nb content increases approaching to the Young's modulus of Nb (E=104 Nb [30]). Almost similar trend in the case of H as result of the existing phases can be explained analogously to Young's modulus.

8.2. Pole figures obtained from X-ray texture measurements
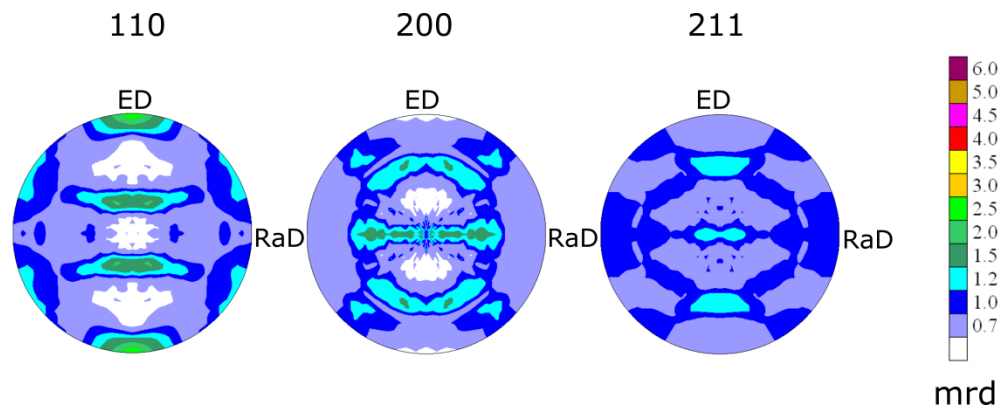
Fig. 8.2: {110}, {200}, {211} pole figures of INI sample of Ti–45.0 Nb alloy in the extrusion system (ED = extrusion direction, RaD = radial direction).
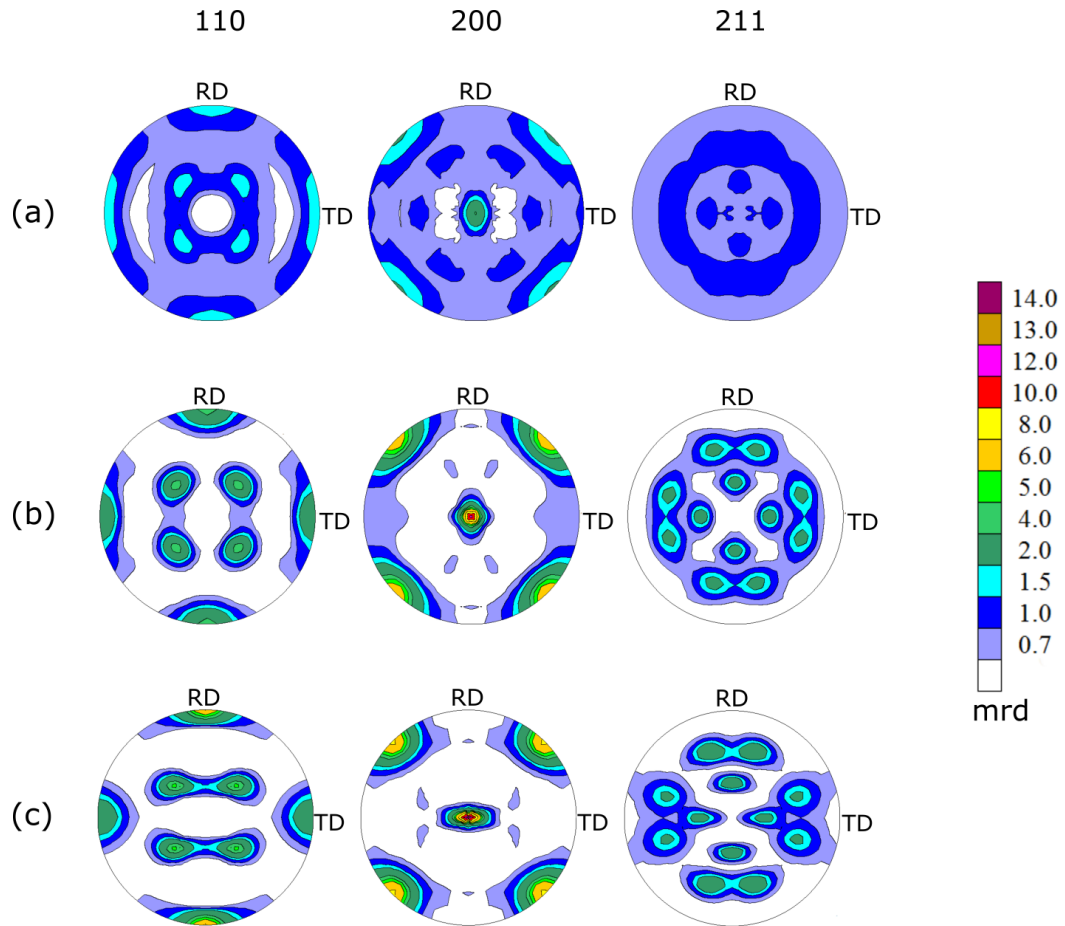
Fig. 8.3: {110}, {200}, {211} pole figures of Ti–45 alloys upon rolling and folding (a) R&F-1 (max. = 5.2 mrd), (b) R&F-3 (max. = 12.3 mrd), and (c) R&F-5 (max. = 13.6 mrd). RD = rolling direction, TD = transverse direction.

Fig. 8.4: {110}, {200}, {211} pole figures of Ti–45 alloys upon simple shear deformation in HPT(a) HPT-4-1 (max. = 1.70 mrd), (b) HPT-4-5 (max. = 1.55 mrd), and (c) HPT-4-10 (max. = 1.77 mrd). SPN = Shear plane normal, SD= Shear direction.

9. Acknowledgments

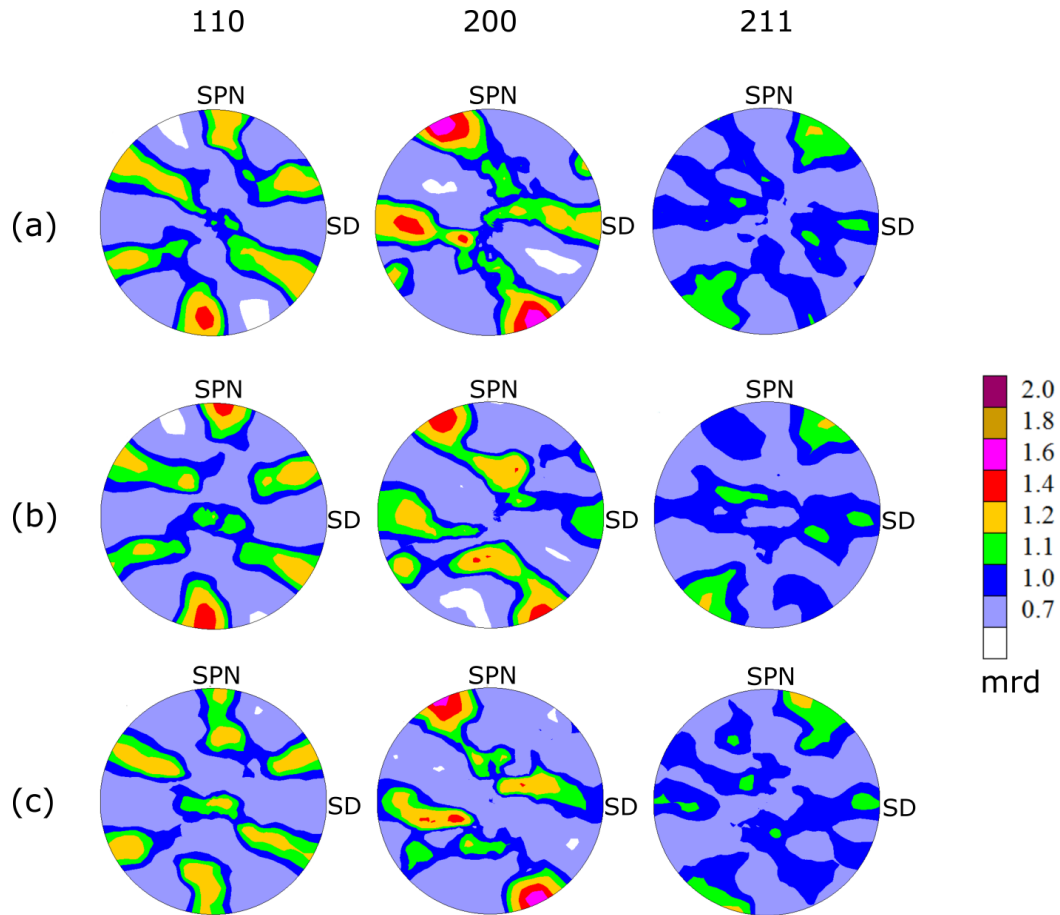The long journey of PhD student consists of an incredible satisfaction and accomplished achievements in one hand and sincere hard work and perseverance on the the other hand. When I look back the path which have been covered, the people whom I met, the amicable scientific environment I was in, I am feeling extremely fortunate and glad to have had these under the roof of Faculty of Physics, University of Vienna and under the EU-Marie Curie Project "BioTiNet". I would like to acknowledge all of them from the bottom of the heart, without their assistance this work would not be possible.

First and foremost, I would like to express my sincere gratitude and indebtedness to my supervisors Prof. M. Zehetbauer and Prof. T. Waitz, Physics of Nanostructured Materials, Faculty of Physics, University of Vienna, for their constant encouragement allowing me to grow as a research scientist and for their scholastic guidance throughout the work. Their profound knowledge on materials science, their innovative ideas and stimulating discussions were the pillars of this success. I would also like to express my special appreciation to them as they never ignored the importance of human aspects in the science and in the life.

In this context, I would also like to acknowledge gratefully the financial support provided by EU-Initial Training Network, "BioTiNet" within framework of FP7/2007-13 project (under grant agreement No. 264635). It not only focused various scientific aspects through many dedicated workshops under different interdisciplinary themes related to the fundamental research areas in the search and the development of the novel load bearing orthopaedics but also offered a special care towards the development of personal skills which helped me to grow as a researcher.

I am very thankful to Mag. M. Bönisch, Prof. M. Calin, and Prof. J. Eckert from IFW-Dresden, Germany for the collaboration work. Their suggestions helped me to unravel the new aspects of the experiments which always led to stimulating scientific discussions and publications.

I would like to express my sincere gratitude to Prof. W. Skrotzki, TU-Dresden whose scientific help and inspiration throughout the project was immense, without his motivating words the thesis could not be reached to this stage. Part of the thesis work was carried out in a close collaboration with him to investigate the texture. In this context I thank to Mag. A. Pukenas for his help in texture experiments.

I express my cordial gratitude to Dr. B. Sulkowski, AGH-University of Science and Technology who is a good friend, always helped me to understand the fundamentals of materials science. To Mag. K. Ozaltin and Prof. M. Lewandowska, Warsaw University of

10. Bibliography

[1]   R.Z. Valiev, Y. Estrin, Z. Horita, T.G. Langdon, M.J. Zehetbauer, Y.T. Zhu, Producing bulk ultrafine-grained materials by severe plastic deformation, JOM. 58 (2006) 33–39.

[2]   R.Z. Valiev, R.K. Islamgaliev, I.V. Alexandrov, Bulk nanostructured materials from severe plastic deformation, Prog. Mater. Sci. 45 (2000) 103–189.

[3]   M.J. Zehetbauer, Y.T. Zhu, eds., Bulk Nanostructured Materials, WILEY VCH, Weinheim, Germany, 2009.

[4]   C.M. Lee, C.P. Ju, J.H.C. Lin, Structure-property relationship of cast Ti–Nb alloys, J. Oral Rehabil. 29 (2002) 314–322.

[5]   D.R. Sumner, T.M. Turner, R. Igloria, R.M. Urban, J.O. Galante, Functional adaptation and ingrowth of bone vary as a function of hip implant stiffness, J. Biomech. 31 (1998) 909–917.

[6]   M. Geetha, A.K. Singh, R. Asokamani, A.K. Gogia, Ti based biomaterials, the ultimate choice for orthopaedic implants-A review, Prog. Mater. Sci. 54 (2009) 397–425.

[7]   M. Bönisch, M. Calin, L. Giebeler, A. Helth, A. Gebert, W. Skrotzki, J. Eckert, Composition-dependent magnitude of atomic shuffles in Ti–Nb martensites, J. Appl. Crystallogr. 47 (2014) 1374–1379.

[8]   M. Bönisch, M. Calin, J. van Humbeeck, W. Skrotzki, J. Eckert, Factors influencing the elastic moduli, reversible strains and hysteresis loops in martensitic Ti–Nb alloys, Mater. Sci. Eng. C. 48 (2015) 511–520.

[9]   R. Hermann, H. Hermann, M. Calin, B. Büchner, J. Eckert, Elastic constants of single crystalline β-Ti70Nb30, Scr. Mater. 66 (2012) 198–201.

[10]   M. Niinomi, Mechanical properties of biomedical titanium alloys, Mater. Sci. Eng. A. 243 (1998) 231–236.

[11]   M. Niinomi, Mechanical biocompatibilities of titanium alloys for biomedical applications, J. Mech. Behav. Biomed. Mater. 1 (2008) 30–42.

[12]   R. Godley, D. Starosvetsky, I. Gotman, Corrosion behavior of a low modulus β-Ti-45 % Nb alloy for use in medical implants, J. Mater. Scince Med. 17 (2006) 63–67.

[13]   Y. Okazaki, Y. Ito, K. Kyo, T. Tateishi, Corrosion resistance and corrosion fatigue strength of new titanium alloys for medical implants without V and Al, Mater. Sci. Eng. A. 213 (1996) 138–147.

[14]   S. Banerjee, P. Mukhopadhyay, Phase Transformations: Examples from Titanium and Zirconium alloys, First Edit, Pergamon Materials Series, Elsevier, Oxford, UK, 2007.

[15]   M. Harold, F. Paul, The physical metallurgy of titanium alloys, Ocean Eng. 1 (1969) 329–345.

[16]   G.A. Sargent, H. Conrad, Formation of omega phase in titanium by hydrostatic pressure soaking, Mater. Sci. Eng. 7 (1971) 220–223.

[17]   A. Jayaraman, W. Klement, G.C. Kennedy, Solid-solid transitions in titanium and zirconium at high pressures, Phys. Rev. 131 (1963) 644–649.

[18]   M.P. Usikov, V.A. Zilbershtein, The orientation relationship between the α- and ω-phases of Titanium and Zirconium, 53 (1973) 53–58.

[19]   S.K. Sikka, Y.K. Vohra, R. Chidambaram, Omega phase in materials, Prog. Mater. Sci. 27 (1982) 245–310.

[20]   D.A. Young, Phase diagrams of the elements, 1975. doi:10.2172/4010212.

[21]   D.L. Moffat, U.R. Kattner, The stable and metastable Ti-Nb phase diagrams, Metall. Trans. A. 19 (1988) 2389–2397.

[22]   K. Edalati, E. Matsubara, Z. Horita, Processing pure Ti by high-pressure torsion in wide ranges of pressures and strain, Metall. Mater. Trans. A Phys. Metall. Mater. Sci. 40 (2009) 2079–2086.

[23]   Y. Ivanisenko, A. Kilmametov, H. Rösner, R.Z. Valiev, Evidence of α → ω phase transition in titanium after high pressure torsion, Int. J. Mater. Res. 99 (2008) 36–41.

[24]   Y. Todaka, J. Sasaki, T. Moto, M. Umemoto, Bulk submicrocrystalline ω-Ti produced by high-pressure torsion straining, Scr. Mater. 59 (2008) 615–618.

[25]   M. Tane, Y. Okuda, Y. Todaka, H. Ogi, A. Nagakubo, Elastic properties of single-crystalline ω phase in titanium, Acta Mater. 61 (2013) 7543–7554.

[26]   D. Banerjee, J.C. Williams, Perspectives on titanium science and technology, Acta Mater. 61 (2013) 844–879.

[27]   M. Long, H.J. Rack, Titanium alloys in total joint replacement--a materials science perspective., Biomaterials. 19 (1998) 1621–1639.

[28]   Y. Zhang, H. Liu, Z. Jin, Thermodynamic assessment of the Nb-Ti system, Calphad Comput. Coupling Phase Diagrams Thermochem. 25 (2001) 305–317.

[29]   S. Hanada, T. Ozaki, E. Takahashi, S. Watanabe, K. Yoshimi, T. Abumiya, Composition dependence of young's modulus in beta titanium binary alloys, Mater. Sci. Forum. 426-432 (2003) 3103–3108.

[30]   S. Hanada, H. Matsumoto, S. Watanabe, Mechanical compatibility of titanium implants in hard tissues, Int. Congr. Ser. 1284 (2005) 239–247.

[31]   A. Panigrahi, M. Bönisch, T. Waitz, E. Schafler, M. Calin, J. Eckert, W. Skrotzki, M. Zehetbauer, Phase transformations and mechanical properties of biocompatible Ti–16.1Nb processed by severe plastic deformation, J. Alloys Compd. 628 (2015) 434–441.

[32]   D.L. Moffat, D.C. Larbalestier, The competition between martensite and omega in quenched Ti–Nb alloys, Metall. Trans. A. 19 (1988) 1677–1686.

[33]   K. Zhuravleva, M. Bönisch, S. Scudino, M. Calin, L. Schultz, J. Eckert, A. Gebert, Phase transformations in ball-milled Ti–40Nb and Ti–45Nb powders upon quenching from the β-phase region, Powder Technol. 253 (2014) 166–171.

[34]   H.Y. Kim, Y. Ikehara, J.I. Kim, H. Hosoda, S. Miyazaki, Martensitic transformation, shape memory effect and superelasticity of Ti–Nb binary alloys, Acta Mater. 54 (2006) 2419–2429.

[35]   X. Chen, V. Srivastava, V. Dabade, R.D. James, Study of the cofactor conditions: Conditions of supercompatibility between phases, J. Mech. Phys. Solids. 61 (2013) 2566–2587.

[36]   C.J. McHargue, S.E. jr. Adair, J.P. Hammond, Effects of solid solution alloying on the cold rolled texture of Titanium, Trans. Am. Inst. Mining, Metall. Pet. 199 (1953) 1199–1203.

[37]   W.G. Burgers, On the process of transition of the cubic-body-centered modification into the hexagonal-close-packed modification of zirconium, Physica. 1 (1934) 561–586.

[38]   A.R.G. Brown, D. Clark, J. Eastabrook, K.S. Jepson, The Titanium-Niobium System, Nature. 201 (1964) 914–915.

[39]   Y.A. Bagariatskii, G.I. Nosova, T.V. Tagunova., Factors in the formation of metastable phases in Titanium-base alloys, Sov. Phys. Dokl. 3 (1958) 1014–1018.

[40] T. Hahn, International Tables for Crystallography: Volume A - Space Group Symmetry, 4th Editio, International Union Of Crystallography, Kluwer Academic Publishers, Dordrecht, 1996.

[41] S. Banumathy, R.K. Mandal, A.K. Singh, Structure of orthorhombic martensitic phase in binary Ti-Nb alloys, J. Appl. Phys. 106 (2009) 3–8.

[42] R. Ahuja, J.M. Wills, B. Johansson, O. Eriksson, Crystal structures of Ti, Zr, and Hf under compression: Theory, Phys. Rev. B. 48 (1993) 16269–16279.

[43] A.V. Dobromyslov, G.V. Dolgikh, A.N. Martem'yanov, Pressure induced α" to ω phase transition in Titanium-Niobium alloys, Phys. Met. Met. 81 (1996) 200–205.

[44] N.S. Afonikova, V.F. Degtyareva, Y.A. Litvin, A.G. Rabinkin, Y.A. Skakov, Superconductivity and structure of Ti-Nb alloys subjected to hydrostatic pressure up to 120 Kbar, Sov. Phys. Solid. State. 15 (1973) 746–749.

[45] G.K. Dey, R. Tewari, S. Banerjee, G. Jyoti, S.C. Gupta, K.D. Joshi, S.K. Sikka, Formation of a shock deformation induced ω phase in Zr–20 Nb alloy, Acta Mater. 52 (2004) 5243–5254.

[46] Y.K. Vohra, S.K. Sikka, R. Chidambaram, Structural aspects of alpha-omega transformation in group IV transition metals and alloys, Bull. Mater. Sci. 3 (1981) 109–117.

[47] R. Ahuja, L. Dubrovinsky, N. Dubrovinskaia, J.M.O. Guillen, M. Mattesini, B. Johansson, T. Le Bihan, Titanium metal at high pressure: Synchrotron experiments and ab initio calculations, Phys. Rev. B - Condens. Matter Mater. Phys. 69 (2004) 2–5.

[48] S. Banerjee, R. Tewari, G.K. Dey, Omega phase transfomration - morphologies and mechanisms, Int. J. Mater. Res. 97 (2006) 963–977.

[49] B.S. Hickman, The formation of omega phase in titanium and zirconium alloys: A review, J. Mater. Sci. 4 (1969) 554–563.

[50] J.C. Williams, D. de Fontaine, N.E. Paton, The ω-phase as an example of an unusual shear transformation, Metall. Trans. 4 (1973) 2701–2708.

[51] D. De Fontaine, N.E. Paton, J.C. Williams, The omega phase transformation in titanium alloys as an example of displacement controlled reactions, Acta Metall. 19 (1971) 1153–1162.

[52] S.L. Sass, The structure and decomposition of Zr and Ti b.c.c. solid solutions, J. Less Common Met. 28 (1972) 157–173.

[53] J.M. Silcock, An X-ray examination of the to phase in TiV, TiMo and TiCr alloys, Acta Metall. 6 (1958) 481–493.

[54] Y.K. Vohra, S.K. Sikka, E.S.K. Menon, R. Krishnan, Direct evidence of intermediate state during alpha-omega transformation in Ti-V alloy, Acta Metall. 28 (1980) 683–685.

[55] D.R. Trinkle, R.G. Hennig, S.G. Srinivasan, D.M. Hatch, M.D. Jones, H.T. Stokes, R.C. Albers, J.W. Wilkins, New mechanism for the alpha to omega martensitic transformation in pure titanium, Phys. Rev. Lett. 91 (2003) 025701.

[56] D. Kuroda, M. Niinomi, M. Morinaga, Y. Kato, T. Yashiro, Design and mechanical properties of new β type titanium alloys for implant materials, Mater. Sci. Eng. A. 243 (1998) 244–249.

[57] M. Niinomi, Biologically and Mechanically Biocompatible Titanium Alloys, Mater. Trans. 49 (2008) 2170–2178.

[58] A. Biesiekierski, J. Wang, M. Abdel-Hady Gepreel, C. Wen, A new look at biomedical Ti-based shape memory alloys, Acta Biomater. 8 (2012) 1661–1669.

[59]   M. Niinomi, Recent metallic materials for biomedical applications, Metall. Mater. Trans. A. 33 (2002) 477–486.

[60]   T.C. Niemeyer, C.R. Grandini, L.M.C. Pinto, A.C.D. Angelo, S.G. Schneider, Corrosion behavior of Ti-13Nb-13Zr alloy used as a biomaterial, J. Alloys Compd. 476 (2009) 172–175.

[61]   J.Y. Rho, T.Y. Tsui, G.M. Pharr, Elastic properties of human cortical and trabecular lamellar bone measured by nanoindentation, Biomaterials. 18 (1997) 1325–1330.

[62]   H.Y. Kim, T. Sasaki, K. Okutsu, J.I. Kim, T. Inamura, H. Hosoda, S. Miyazaki, Texture and shape memory behavior of Ti–22Nb–6Ta alloy, Acta Mater. 54 (2006) 423–433.

[63]   H. Matsumoto, S. Watanabe, S. Hanada, Beta TiNbSn Alloys with Low Young's Modulus and High Strength, Mater. Trans. 46 (2005) 1070–1078.

[64]   H. Yilmazer, M. Niinomi, M. Nakai, K. Cho, J. Hieda, Y. Todaka, T. Miyazaki, Mechanical properties of a medical β-type titanium alloy with specific microstructural evolution through high-pressure torsion, Mater. Sci. Eng. C. 33 (2013) 2499–2507.

[65]   O.M. Ivasishin, P.E. Markovsky, Y. V. Matviychuk, S.L. Semiatin, C.H. Ward, S. Fox, A comparative study of the mechanical properties of high-strength β-titanium alloys, J. Alloys Compd. 457 (2008) 296–309.

[66]   H. Matsumoto, S. Watanabe, N. Masahashi, S. Hanada, Composition dependence of Young's modulus in Ti-V, Ti-Nb, and Ti-V-Sn alloys, Metall. Mater. Trans. A. 37 (2006) 3239–3249.

[67]   Y.L. Hao, S.J. Li, S.Y. Sun, C.Y. Zheng, R. Yang, Elastic deformation behaviour of Ti-24Nb-4Zr-7.9Sn for biomedical applications, Acta Biomater. 3 (2007) 277–286.

[68]   P. Laheurte, F. Prima, A. Eberhardt, T. Gloriant, M. Wary, E. Patoor, Mechanical properties of low modulus β-titanium alloys designed from the electronic approach, J. Mech. Behav. Biomed. Mater. 3 (2010) 565–573.

[69]   T. Furuta, S. Kuramoto, N. Nagasako, Z. Horita, Shear Strength Measurement of Gum Metal during High-Pressure Torsion, Mater. Sci. Forum. 706-709 (2012) 1769–1774.

[70]   T. Furuta, M. Hara, Z. Horita, S. Kuramoto, Severe plastic deformation in Gum Metal with composition at the structural stability limit, Int. J. Mater. Res. 100 (2009) 1217–1221.

[71]   K.Y. Xie, Y. Wang, Y. Zhao, L. Chang, G. Wang, Z. Chen, Y. Cao, X. Liao, E.J. Lavernia, R.Z. Valiev, B. Sarrafpour, H. Zoellner, S.P. Ringer, Nanocrystalline β-Ti alloy with high hardness, low Young's modulus and excellent in vitro biocompatibility for biomedical applications, Mater. Sci. Eng. C. 33 (2013) 3530–3536.

[72]   B. Sulkowski, A. Panigrahi, K. Ozaltin, M. Lewandowska, B. Mikułowski, M. Zehetbauer, Evolution of strength and structure during SPD processing of Ti–45Nb alloys: experiments and simulations, J. Mater. Sci. 49 (2014) 6648–6655.

[73]   A. Panigrahi, B. Sulkowski, T. Waitz, K. Ozaltin, W. Chrominski, A. Pukenas, J. Horky, M. Lewandowska, W. Skrotzki, M. Zehetbauer, Mechanical properties, structural and texture evolution of biocompatible Ti–45Nb alloy processed by severe plastic deformation, J. Mech. Behav. Biomed. Mater. 62 (2016) 93–105.

[74]   C. Zener, Contributions to the theory of beta-phase alloys, Phys. Rev. 71 (1947) 846–851.

[75]   H. Ikehata, N. Nagasako, T. Furuta, A. Fukumoto, K. Miwa, T. Saito, First-principles calculations for development of low elastic modulus Ti alloys, Phys. Rev. B. 70 (2004) 1–8.

[76]   M.Y. Gutkin, T. Ishizaki, S. Kuramoto, I.A. Ovid'ko, Nanodisturbances in deformed Gum Metal, Acta Mater. 54 (2006) 2489–2499.

[77]   R.J. Talling, R.J. Dashwood, M. Jackson, S. Kuramoto, D. Dye, Determination of (C11 - C12) in Ti-36Nb-2Ta-3Zr-0.3O (wt.%) (Gum metal), Scr. Mater. 59 (2008) 669–672.

[78]   K. Enami, J. Hasunuma, A. Nagasawa, S. Nenno, Elastic constants and electron diffraction anomalies prior to the matensitic transformation in a Ni–Al β1 alloy, Scr. Metall. I (1976) 879–884.

[79]   T. Nakano, Metallic properties of metallic biomaterials, in: M. Niinomi (Ed.), Met. Biomed. Devices, Woodhead Publishing Ltd., Cambridge, UK, 2010: pp. 71–98.

[80]   S.G. Fedotov, P.K. Belousov, Elastic constants of alloys of the system titanium–niobium, Fiz. Met. Met. 17 (1964) 83–86.

[81]   T. Ozaki, H. Matsumoto, S. Watanabe, S. Hanada, Beta Ti Alloys with Low Young's Modulus, Mater. Trans. 45 (2004) 2776–2779.

[82]   G.T. Burstein, I.M. Hutchings, K. Sasaki, Electrochemically induced annealing of stainless-steel surfaces., Nature. 407 (2000) 885–887.

[83]   T. Matković, P. Matković, J. Malina, Effects of Ni and Mo on the microstructure and some other properties of Co-Cr dental alloys, J. Alloys Compd. 366 (2004) 293–297.

[84]   S.S. Da Rocha, G.L. Adabo, G.E.P. Henriques, M.A.D.A. Nóbilo, Vickers hardness of cast commercially pure titanium and Ti-6Al-4V alloy submitted to heat treatments, Braz. Dent. J. 17 (2006) 126–129.

[85]   Y. Ohmori, T. Ogo, K. Nakai, S. Kobayashi, Effects of ω-phase precipitation on β → α, α″ transformations in a metastable β titanium alloy, Mater. Sci. Eng. A. 312 (2001) 182–188.

[86]   H.Y. Kim, J.I. Kim, T. Inamura, H. Hosoda, S. Miyazaki, Effect of thermo-mechanical treatment on mechanical properties and shape memory behavior of Ti–(26–28)at.% Nb alloys, Mater. Sci. Eng. A. 438-440 (2006) 839–843.

[87]   A.V. Sergueeva, V.V. Stolyarov, R.Z. Valiev, A.K. Mukherjee, Advanced mechanical properties of pure titanium with ultrafine grained structure, Scr. Mater. 45 (2001) 747–752.

[88]   M. Zehetbauer, V. Seumer, Cold work hardening in stages IV and V of F.C.C. metals—I. Experiments and interpretation, Acta Metall. Mater. 41 (1993) 577–588.

[89]   H. Gleiter, Nanostructured materials: basic concepts and microstructure, Acta Mater. 48 (2000) 1–29.

[90]   C.C. Koch, Top-Down synthesis of nanoestructured materialas, mechanical and thermal processing methods., Rev. Adv. Mater. Sci. 5 (2003) 91–99.

[91]   H. Gleiter, Nanocrystalline Materials, Prog. Mater. Sci. 33 (1989) 223–315.

[92]   U. Erb, Electrodeposited Nanocrystals: synthesis, properties and industrial applications, NanoStrcutured Mater. 6 (1995) 533–538.

[93]   R.Z. Valiev, T.G. Langdon, Principles of equal-channel angular pressing as a processing tool for grain refinement, Prog. Mater. Sci. 51 (2006) 881–981.

[94]   M.J. Zehetbauer, H.P. Stüwe, A. Vorhauer, E. Schafler, J. Kohout, The Role of Hydrostatic Pressure in Severe Plastic Deformation, Adv. Eng. Mater. 5 (2003) 330–337.

[95]   P.W. Bridgman, On torsion combined with compression, J. Appl. Phys. 14 (1943) 273–283.

[96]   A. Vorhauer, R. Pippan, On the homogeneity of deformation by high pressure torsion, Scr. Mater. 51 (2004) 921–925.

[97] T. Hebesberger, H.P. Stüwe, A. Vorhauer, F. Wetscher, R. Pippan, Structure of Cu deformed by high pressure torsion, Acta Mater. 53 (2005) 393–402.

[98] V.M. Segal, V.I. Reznikov, A.E. Drobyshevskiy, V.I. Kopylov, Plastic working of metals by simple shear, Russ. Metall. 1 (1981) 99–105.

[99] V.M. Segal, Materials processing by simple shear, Mater. Sci. Eng. A. 197 (1995) 157–164.

[100] Y. Saito, H. Utsunomiya, N. Tsuji, T. Sakai, Novel ultra-high straining process for bulk materials—development of the accumulative roll-bonding (ARB) process, Acta Mater. 47 (1999) 579–583.

[101] N. Tsuji, Y. Saito, S.H. Lee, Y. Minamino, ARB (accumulative roll-bonding) and other new techniques to produce bulk ultrafine grained materials, Adv. Eng. Mater. 5 (2003) 338–344.

[102] K. Topolski, W. Pachla, H. Garbacz, Progress in hydrostatic extrusion of titanium, J. Mater. Sci. 48 (2013) 4543–4548.

[103] G.P. Dinda, H. Rösner, G. Wilde, Synthesis of bulk nanostructured materials by repeated cold-rolling, Scr. Mater. 52 (2005) 577–582.

[104] http://thelibraryofmanufacturing.com/hydrostatic_extrusion.html, (n.d.).

[105] J.M. Rosenberg, H.R. Piehler, Calculation of the taylor factor and lattice rotations for bcc metals deforming by pencil glide, Metall. Trans. 2 (1971) 257–259.

[106] G. Gottstein, Physical foundations of materials science, Springer-Verlag Berlin Heidelberg, 2004.

[107] R. Pippan, S. Scheriau, A. Taylor, M. Hafok, A. Hohenwarter, A. Bachmaier, Saturation of fragmentation during severe plastic deformation, Annu. Rev. Mater. Res. 40 (2010) 319–343.

[108] D. Kuhlmann-Wilsdorf, N. Hansen, Geometrically necessary, Incidental and Subgrain boundaries, Scr. Metall. Mater. 25 (1991) 1557–1562.

[109] D.A. Hughes, N. Hansen, High angle boundaries formed by grain subdivision mechanisms, Acta Mater. 45 (1997) 3871–3886.

[110] N. Hansen, X. Huang, D.A. Hughes, Microstructural evolution and hardening parameters, Mater. Sci. Eng. A. 317 (2001) 3–11.

[111] O. Rezvanian, M.A. Zikry, A.M. Rajendran, Statistically stored, geometrically necessary and grain boundary dislocation densities: microstructural representation and modelling, Proc. R. Soc. A Math. Phys. Eng. Sci. 463 (2007) 2833–2853.

[112] H. Mughrabi, Dislocation wall and cell structures and long-range internal stresses in deformed metal crystals, Acta Metall. 31 (1983) 1367–1379.

[113] A.D. Rollett, U.F. Kocks, A Review of the stages of work hardening, Solid State Phenom. 35-36 (1993) 1–18.

[114] T. Ungar, M. Zehetbauer, Stage IV work hardening in cell forming materials, Part II. A new mechanism, Scr. Mater. 35 (1996) 1467–1473.

[115] M. Müller, M. Zehetbauer, A. Borbély, T. Ungár, Stage IV work hardening in cell forming materials, part I: Features of the dislocation structure determined by X-ray line broadening, Scr. Mater. 35 (1996) 1461–1466.

[116] B. Yang, H. Vehoff, A. Hohenwarter, M. Hafok, R. Pippan, Strain effects on the coarsening and softening of electrodeposited nanocrystalline Ni subjected to high pressure torsion, Scr. Mater. 58 (2008) 790–793.

[117] E. Schafler, Investigation of highly deformed metals by means of X-ray Bragg-peak

profile analysis, Doctoral thesis, University of Vienna, 1998.

[118] H.W. Zhang, X. Huang, N. Hansen, R. Pippan, M.J. Zehetbauer, Strengthening of Nickel Deformed by High Pressure Torsion, Mater. Sci. Forum. 584-586 (2008) 417–421.

[119] J. Gubicza, N.Q. Chinh, T. Csanádi, T.G. Langdon, T. Ungár, Microstructure and strength of severely deformed fcc metals, Mater. Sci. Eng. A. 462 (2007) 86–90.

[120] E.O. Hall, The Deformation and Ageing of Mild Steel: III Discussion of Results, Proc. Phys. Soc. Sect. B. 64 (1951) 747–753.

[121] R.W. Armstrong, I. Codd, R.M. Douthwaite, N.J. Petch, The plastic deformation of polycrystalline aggregates, Philos. Mag. 7 (1962) 45–48.

[122] M. Zehetbauer, Cold work hardening in stages IV and V of fcc metals -II. Model fits and physical results, Acta Metall. Mater. 41 (1993) 589–599.

[123] L.F. Zeipper, M.J. Zehetbauer, C. Holzleithner, Defect based micromechanical modelling and simulation of nanoSPD CP-Ti in post-deformation, Mater. Sci. Eng. A. 410-411 (2005) 217–221.

[124] Y. Estrin, L.S. Toth, A. Molinari, Y. Brechet, A dislocation based model for all hardening stages in large strain deformation, Acta Mater. 46 (1998) 5509–5522.

[125] W.J. Kim, C.Y. Hyun, H.K. Kim, Fatigue strength of ultrafine-grained pure Ti after severe plastic deformation, Scr. Mater. 54 (2006) 1745–1750.

[126] G. Purcek, G.G. Yapici, I. Karaman, H.J. Maier, Effect of commercial purity levels on the mechanical properties of ultrafine-grained titanium, Mater. Sci. Eng. A. 528 (2011) 2303–2308.

[127] V.V. Stolyarov, Y.T. Zhu, I.V. Alexandrov, T.C. Lowe, R.Z. Valiev, Grain refinement and properties of pure Ti processed by warm ECAP and cold rolling, Mater. Sci. Eng. A. 343 (2003) 43–50.

[128] W. Pachla, M. Kulczyk, M. Sus-Ryszkowska, A. Mazur, K.J. Kurzydlowski, Nanocrystalline titanium produced by hydrostatic extrusion, J. Mater. Process. Technol. 205 (2008) 173–182.

[129] S. Zherebtsov, W. Lojkowski, A. Mazur, G. Salishchev, Structure and properties of hydrostatically extruded commercially pure titanium, Mater. Sci. Eng. A. 527 (2010) 5596–5603.

[130] K. Ozaltin, W. Chrominski, M. Kulczyk, A. Panigrahi, J. Horky, M. Zehetbauer, M. Lewandowska, Enhancement of mechanical properties of biocompatible Ti–45Nb alloy by hydrostatic extrusion, J. Mater. Sci. 49 (2014) 6930–6936.

[131] V.-D. Cojocaru, D. Raducanu, T. Gloriant, I. Cinca, Texture Evolution in a Ti-Ta-Nb Alloy Processed by Severe Plastic Deformation, Jom. 64 (2012) 572–581.

[132] T. Inamura, H. Hosoda, K. Wakashima, S. Miyazaki, Anisotropy and temperature dependence of Young's modulus in textured TiNbAl biomedical shape memory alloy, Mater. Trans. 46 (2005) 1597–1603.

[133] W. Xu, X. Wu, M. Calin, M. Stoica, J. Eckert, K. Xia, Formation of an ultrafine-grained structure during equal-channel angular pressing of a β-titanium alloy with low phase stability, Scr. Mater. 60 (2009) 1012–1015.

[134] T. Furuta, S. Kuramoto, J.W. Morris, N. Nagasako, E. Withey, D.C. Chrzan, The mechanism of strength and deformation in Gum Metal, Scr. Mater. 68 (2013) 767–772.

[135] H. Yilmazer, M. Niinomi, M. Nakai, J. Hieda, Y. Todaka, T. Akahori, T. Miyazaki, Heterogeneous structure and mechanical hardness of biomedical β-type Ti-29Nb-13Ta-4.6Zr subjected to high-pressure torsion, J. Mech. Behav. Biomed. Mater. 10

(2012) 235–245.

[136] D. Kent, G. Wang, Z. Yu, X. Ma, M. Dargusch, Strength enhancement of a biomedical titanium alloy through a modified accumulative roll bonding technique, J. Mech. Behav. Biomed. Mater. 4 (2011) 405–416.

[137] Y.B. Wang, Y.H. Zhao, Q. Lian, X.Z. Liao, R.Z. Valiev, S.P. Ringer, Y.T. Zhu, E.J. Lavernia, Grain size and reversible beta-to-omega phase transformation in a Ti alloy, Scr. Mater. 63 (2010) 613–616.

[138] T. Yano, Y. Murakami, D. Shindo, Y. Hayasaka, S. Kuramoto, Transmission electron microscopy studies on nanometer-sized ω phase produced in Gum Metal, Scr. Mater. 63 (2010) 536–539.

[139] T. Saito, T. Furuta, J.H. Hwang, S. Kuramoto, K. Nishino, N. Suzuki, R. Chen, A. Yamada, K. Ito, Y. Seno, T. Nonaka, H. Ikehata, N. Nagasako, C. Iwamoto, Y. Ikuhara, T. Sakuma, Multi Functional Titanium Alloy GUM METAL'', Mater. Sci. Forum. 426-432 (2003) 681–688.

[140] S. Kuramoto, T. Furuta, J.H. Hwang, K. Nishino, T. Saito, Plastic deformation in a multifunctional Ti–Nb–Ta–Zr–O alloy, Metall. Mater. Trans. A. 37 (2006) 657–662.

[141] M. Hara, Y. Shimizu, T. Yano, N. Takesue, T. Furuta, S. Kuramoto, Mechanical anisotropy and ideal strength in a multifunctional Ti-Nb-Ta-Zr-O alloy (Gum Metal), Int. J. Mater. Res. 100 (2009) 345–348.

[142] M. Tane, T. Nakano, S. Kuramoto, M. Niinomi, N. Takesue, H. Nakajima, ω Transformation in cold-worked Ti–Nb–Ta–Zr–O alloys with low body-centered cubic phase stability and its correlation with their elastic properties, Acta Mater. 61 (2013) 139–150.

[143] M. Geetha, A.K. Singh, K. Muraleedharan, A.K. Gogia, R. Asokamani, Effect of thermomechanical processing on microstructure of a Ti–13Nb–13Zr alloy, J. Alloys Compd. 329 (2001) 264–271.

[144] I. Cvijović-Alagić, Z. Cvijović, S. Mitrović, M. Rakin, D. Veljović, M. Babić, Tribological behaviour of orthopaedic Ti–13Nb–13Zr and Ti–6Al–4V alloys, Tribol. Lett. 40 (2010) 59–70.

[145] T. Lee, Y.U. Heo, C.S. Lee, Microstructure tailoring to enhance strength and ductility in Ti–13Nb–13Zr for biomedical applications, Scr. Mater. 69 (2013) 785–788.

[146] A.P. Hammersley, S.O. Svensson, M. Hanfland, A.N. Fitch, D. Hausermann, Two-dimensional detector software: from real detector to idealised image or two-theta scan, High Press. Res. 14 (1996) 235–248.

[147] H.M. Rietveld, Line profiles of neutron powder-diffraction peaks for structure refinement, Acta Crystallogr. 22 (1967) 151–152.

[148] H.M. Rietveld, A profile refinement method for nuclear and magnetic structures, J. Appl. Crystallogr. 2 (1969) 65–71.

[149] W.A. Dollase, Correction of intensities of preferred orientation in powder diffractometry: application of the March model., J. Appl. Crystallogr. 19 (1986) 267–272.

[150] T.M. Sabine, B.A. Hunter, W.R. Sabine, C.J. Ball, Analytical Expressions for the Transmission Factor and Peak Shift in Absorbing Cylindrical Specimens, J. Appl. Crystallogr. 31 (1998) 47–51.

[151] H. Hermann, M. Ermrich, Microabsorption of X-ray intensity in randomly packed powder specimens, Acta Crystallogr. Sect. A Found. Crystallogr. 43 (1987) 401–405.

[152] T.M. Sabine, A reconciliation of extinction theories, Acta Crystallogr. Sect. A Found. Crystallogr. 44 (1988) 368–374.

[153] D.B. Wiles, R.A. Young, A new computer program for Rietveld analysis of X-Ray-powder diffraction patterns, J. Appl. Crystallogr. 14 (1981) 149–151.

[154] G. Caglioti, A. Paoletti, F.P. Ricci, Choice of collimators for a crystal spectrometer for neutron diffraction, Nucl. Instruments. 3 (1958) 223–228.

[155] L.B. McCusker, R.B. Von Dreele, D.E. Cox, D. Louër, P. Scardi, Rietveld refinement guidelines, J. Appl. Crystallogr. 32 (1999) 36–50.

[156] L.W. Finger, D.E. Cox, A.P. Jephcoat, Correction for powder diffraction peak asymmetry due to axial divergence, J. Appl. Crystallogr. 27 (1994) 892–900.

[157] D.L. Bish, S.A. Howard, Quantitative phase analysis using the Rietveld method, J. Appl. Crystallogr. 21 (1988) 86–91.

[158] R.J. Hill, C.J. Howard, Quantitative phase analysis from neutron powder diffraction data using the Rietveld method, J. Appl. Crystallogr. 20 (1987) 467–474.

[159] O. Engler, V. Randle, Introduction to texture analysis: macrotexture, microtexture and orientation mapping, 2nd ed., CRC press, Boca Raton, 2010.

[160] K. Pawlik, Determination of the Orientation Distribution Function from Pole Figures in ArbitrariIy Defined Cells, Phys. Solid State. 134 (1986) 477–483.

[161] K. Pawlik, P. Ozga, Texture Analysis Software, "Göttinger Arbeiten zur Geologie und Paläontologie", SB4, 1999.

[162] T. Ungár, G. Tichy, J. Gubicza, R.J. Hellmig, Correlation between subgrains and coherently scattering domains, Powder Diffr. 20 (2005) 366–375.

[163] G. Ribárik, T. Ungár, J. Gubicza, MWP-fit: a program for Multiple Whole Profile fitting of diffraction profiles by ab-initio theoretical functions, J. Appl. Crystallogr. 34 (2001) 669–676.

[164] T. Ungár, J. Gubicza, G. Ribárik, A. Borbély, Crystallite size distribution and dislocation structure determined by diffraction profile analysis : principles and practical application to cubic and hexagonal crystals, J. Appl. Crystallogr. 34 (2001) 298–310.

[165] B.E. Warren, B.L. Averbach, The effect of cold-work distortion on x-ray patterns, J. Appl. Phys. 21 (1950) 595–599.

[166] B.E. Warren, B.L. Averbach, The separation of cold-work distortion and particle size broadening in x-ray patterns, J. Appl. Phys. 23 (1952) 497.

[167] M. Wilkens, The determination of density and distribution of dislocations in deformed single crystals from broadened X-ray diffraction profiles, Phys. Status Solidi. 2 (1970) 359–370.

[168] T. Ungár, I. Dragomir, Á.;. Révész, A. Borbély, The contrast factors of dislocations in cubic crystals: the dislocation model of strain anisotropy in practice, J. Appl. Crystallogr. 32 (1999) 992–1002.

[169] T. Ungár, Microstructural parameters from X-ray diffraction peak broadening, Scr. Mater. 51 (2004) 777–781.

[170] J. Martinez-Garcia, M. Leoni, P. Scardi, A general approach for determining the diffraction contrast factor of straight-line dislocations, Acta Crystallogr. Sect. A Found. Crystallogr. 65 (2009) 109–119.

[171] I. Groma, X-ray line broadening due to an inhomogeneous dislocation distribution, Phys. Rev. B. 57 (1998) 7535–7542.

[172] M. Kerber, E. Schafler, M. Zehetbauer, Processing and evaluation of X-ray line profiles

measured from nanostructured materials produced by severe plastic deformation, Rev.Adv.Mater.Sci. 10 (2005) 427–433.

[173] A. Borbély, J. Dragomir-Cernatescu, G. Ribárik, T. Ungár, Computer program ANIZC for the calculation of diffraction contrast factors of dislocations in elastically anisotropic cubic, hexagonal and trigonal crystals, J. Appl. Crystallogr. 36 (2003) 160–162.

[174] D.W. Marquardt, An Algorithm for Least-Squares Estimation of Nonlinear Parameters, J. Soc. Ind. Appl. Math. 11 (1963) 431–441.

[175] K. Levenberg, A method for the solution of certain nonlinear problems in least squares, Quart. Appl. Math. 2 (1944) 164–168.

[176] C. Gammer, C. Mangler, C. Rentenberger, H.P. Karnthaler, Quantitative local profile analysis of nanomaterials by electron diffraction, Scr. Mater. 63 (2010) 312–315.

[177] D.B. Williams, C.B. Carter, Transmission electron microscopy; a textbook for materials science, Plenum Press, New York, 1996.

[178] http://www.aeisndt.com/mechanical-testing-hardness-testing.html, (n.d.).

[179] W.C. Oliver, G.M. Pharr, An improved technique for determining the hardness and elastic modulus using load and displacement sensing indentation experiments, J. Mater. Res. 7 (1992) 1564–1583.

[180] W.C. Oliver, G.M. Pharr, Measurement of hardness and elastic modulus by instrumented indentation: Advances in understanding and refinements to methodology, J. Mater. Res. 19 (2004) 3–20.

[181] E. Arzt, Size effects in materials due to microstructural and dimensional constraints: a comparative review, Acta Mater. 46 (1998) 5611–5626.

[182] J. Horky, M. Lederer, B. Weiss, M. Zehetbauer, B. Zagar, Application of a locally operating laser-speckle strain sensor on tensile deformation of miniaturized nanostructured specimens, in: 20th IMEKO TC2 Symp. Photonics Meas., 2011: pp. 1–5.

[183] I. Yamaguchi, Speckle displacement and decorrelation in the diffraction and image fields for small object deformation, Opt. Acta Int. J. Opt. 28 (1981) 1359–1376.

[184] E.S. Watson, M.J. O'Neill, Differential Microcalorimeter, US Patent -3,263,484, 1966.

[185] P. Gill, T.T. Moghadam, B. Ranjbar, Differential scanning calorimetry techniques: applications in biology and nanoscience., J. Biomol. Tech. 21 (2010) 167–193.

[186] D. Setman, Lattice defects in HPT processed fcc nanometals studied by differential scanning calorimetry, 2010.

[187] A. Panigrahi, M. Bönisch, T. Waitz, M. Calin, J. Eckert, W. Skrotzki, M. Zehetbauer, Thermal stability of HPT-induced omega phase in biocompatible Ti–16.1 Nb alloys, in: M. Militzer, G. Botton, L.Q. Chen, J. Howe, C. Sinclair, H. Zurob (Eds.), Proc. 7th Int. Conf. Solid-Solid Phase Transform., The Minerals, Metals & Materials Society (TMS), USA, 2015: pp. 263–268.

[188] A.D. Rollett, S.I. Wright, Typical Textures in Metals, in: H.-R. Kocks, U.F. Tomé, C.N. Wenk (Ed.), Texture Anisotropy Prefer. Orientations Polycrystals Their Eff. Mater. Prop., Cambridge University Press, UK, 1998: pp. 178–238.

[189] H.-R. Wenk, Pole Figure Measurements wih Diffraction Techniques, in: H.-R. Kocks, U.F. Tomé, C.N. Wenk (Ed.), Texture AnisotropyPreferred Orientations Polycrystals Their Eff. Mater. Prop., Cambridge University Press, UK, 1998: pp. 126–176.

[190] S. Li, I.J. Beyerlein, M.A.M. Bourke, Texture formation during equal channel angular extrusion of fcc and bcc materials: Comparison with simple shear, Mater. Sci. Eng. A.

394 (2005) 66–77.

[191] I.J. Beyerlein, L.S. Tóth, Texture evolution in equal-channel angular extrusion, Prog. Mater. Sci. 54 (2009) 427–510.

[192] M. Bönisch, M. Calin, T. Waitz, A. Panigrahi, M. Zehetbauer, A. Gebert, W. Skrotzki, J. Eckert, Thermal stability and phase transformations of martensitic Ti–Nb alloys, Sci. Technol. Adv. Mater. 14 (2013) 055004.

[193] B. Srinivasarao, a. P. Zhilyaev, M.T. Pérez-Prado, Orientation dependency of the alpha to omega plus beta transformation in commercially pure zirconium by high-pressure torsion, Scr. Mater. 65 (2011) 241–244.

[194] K. Edalati, Z. Horita, S. Yagi, E. Matsubara, Allotropic phase transformation of pure zirconium by high-pressure torsion, Mater. Sci. Eng. A. 523 (2009) 277–281.

[195] M.T. Pérez-Prado, A.A. Gimazov, O.A. Ruano, M.E. Kassner, A.P. Zhilyaev, Bulk nanocrystalline ω-Zr by high-pressure torsion, Scr. Mater. 58 (2008) 219–222.

[196] T. Antretter, F.D. Fischer, (private communication), in: n.d.

[197] Y. Mantani, K. Kudou, Effect of plastic deformation on material properties and martensite structures in Ti-Nb alloys, J. Alloys Compd. 577 (2013) S448–S452.

[198] J. Sietsma, Nucleation and growth during the austenite-to-ferrite phase transformation in steels after plastic deformation, in: Phase Transform. Steels, Elsevier, 2012: pp. 505–526.

[199] R. Ding, Z.X. Guo, A. Wilson, Microstructural evolution of a Ti–6Al–4V alloy during thermomechanical processing, Mater. Sci. Eng. A. 327 (2002) 233–245.

[200] T. Seshacharyulu, S.C. Medeiros, W.G. Frazier, Y.V.R.K. Prasad, Microstructural mechanisms during hot working of commercial grade Ti-6Al-4V with lamellar starting structure, Mater. Sci. Eng. A. 325 (2002) 112–125.

[201] H.S. Kim, On the rule of mixtures for the hardness of particle reinforced composites, Mater. Sci. Eng. A. 289 (2000) 30–33.

[202] D. De Fontaine, Mechanical instabilities in the b.c.c. lattice and the beta to omega phase transformation, Acta Metall. 18 (1970) 275–279.

[203] W. Pan, M. Todai, T. Nakano, β-Phase instability in binary Ti-x Nb biomaterial single crystals, Mater. Trans. 54 (2013) 156–160.

[204] M. Todai, T. Fukuda, T. Kakeshita, Relation between negative temperature coefficient in electrical resistivity and athermal ω phase in Ti-xNb (26 ≤ x ≤ 29 at.%) alloys, J. Alloys Compd. 577 (2013) S431–S434.

[205] R.P. Kolli, W.J. Joost, S. Ankem, Phase Stability and Stress-Induced Transformations in Beta Titanium Alloys, JOM. 67 (2015) 1273–1280.

[206] T. Inamura, Y. Kinoshita, J.I. Kim, H.Y. Kim, H. Hosoda, K. Wakashima, S. Miyazaki, Effect of {001} ⟨110⟩ texture on superelastic strain of Ti–Nb–Al biomedical shape memory alloys, Mater. Sci. Eng. A. 438-440 (2006) 865–869.

[207] V.D. Cojocaru, D. Raducanu, T. Gloriant, D.M. Gordin, I. Cinca, Effects of cold-rolling deformation on texture evolution and mechanical properties of Ti–29Nb–9Ta–10Zr alloy, Mater. Sci. Eng. A. 586 (2013) 1–10.

[208] B. Sander, D. Raabe, Texture inhomogeneity in a Ti-Nb-based β-titanium alloy after warm rolling and recrystallization, Mater. Sci. Eng. A. 479 (2008) 236–247.

[209] Y.F. Xu, D.Q. Yi, H.Q. Liu, X.Y. Wu, B. Wang, F.L. Yang, Effects of cold deformation on microstructure, texture evolution and mechanical properties of Ti-Nb-Ta-Zr-Fe alloy

for biomedical applications, Mater. Sci. Eng. A. 547 (2012) 64–71.

[210] M.A.-H. Gepreel, Texturing Tendency in β-Type Ti-Alloys, in: P. Wilson (Ed.), Recent Dev. Study Recryst., InTech, 2013. doi:http://dx.doi.org/10.5772/53588.

[211] M. Abdel-Hady, K. Hinoshita, M. Morinaga, General approach to phase stability and elastic properties of β-type Ti-alloys using electronic parameters, Scr. Mater. 55 (2006) 477–480.

[212] M. Abdel-Hady, H. Fuwa, K. Hinoshita, H. Kimura, Y. Shinzato, M. Morinaga, Phase stability change with Zr content in β-type Ti-Nb alloys, Scr. Mater. 57 (2007) 1000–1003.

[213] H. Matsumoto, S. Watanabe, S. Hanada, Microstructures and mechanical properties of metastable β TiNbSn alloys cold rolled and heat treated, J. Alloys Compd. 439 (2007) 146–155.

[214] L.S. Tóth, K.W. Neale, J.J. Jonas, Stress response and persistence characteristics of the ideal orientations of shear textures, Acta Metall. 37 (1989) 2197–2210.

[215] L.S. Tóth, Y. Estrin, R. Lapovok, C. Gu, A model of grain fragmentation based on lattice curvature, Acta Mater. 58 (2010) 1782–1794.

[216] W. Skrotzki, A. Eschke, B. Joni, T. Ungár, L.S. Tóth, Y. Ivanisenko, L. Kurmanaeva, New experimental insight into the mechanisms of nanoplasticity, Acta Mater. 61 (2013) 7271–7284.

[217] S. Guo, J. Zhang, X. Cheng, X. Zhao, A metastable β-type Ti–Nb binary alloy with low modulus and high strength, J. Alloys Compd. 644 (2015) 411–415.

11. Curriculum Vitae

M.Tech. PANIGRAHI Ajit
Physics of Nanostructured Materials
Faculty of physics
University of Vienna
Boltzmanngasse -5/EG/Zi.32
A-1090, Vienna, Austria
Tel: +43 1 4277 72846
e-mail: ajit.panigrahi@univie.ac.at

Date of Birth :   25.12.1986
Place of Birth :   Bhubaneswar, India
Marital status :   Unmarried
Nationality   :   Indian

Education

Since 10/2011
- PhD studies at University of Vienna, Faculty of Physics, Vienna, Austria.
- The thesis title "Nanostructured Ti-based biomaterials processed by severe plastic deformation" under supervision of Prof. M. Zehetbauer and Prof. T. Waitz, University of Vienna (through EU-Marie Curie ITN Fellowship for the project BioTiNet).

08/2009–
06/2011
- Master of Technology (M.Tech.) in the dept. of Metallurgical and Materials Engineering at Indian Institute of Technology, IIT Madras, Tamilnadu, India.
- The thesis titled "The effect of up-scaling of equal channel angular processing on texture evolution in technical pure aluminum" under joint supervision of Prof. W. Skrotzki, Technical University of Dresden, Germany and Prof. S. Sankaran, IIT Madras (through DAAD-IIT sandwich programme).
- Graduated with distinction on 22.07.2011.

08/2005– 05/2009	• Bachelor of Technology (B.Tech.) in the dept. of Metallurgical and Materials Engineering at National Institute of Technology, NIT Rourkela, Odisha, India. • The thesis title "Characterization of hybrid FRP composite with hydrothermal exposure under varied ambient conditions" under Prof. U.K. Mohanty. • Graduated with distinction on 06.07.2009.
07/2001– 05/2003	Intermediate studies (+2) in science at BJB junior college, Bhubaneswar, Odisha, India.
1990–2001	Elementary and high school studies at Capital high school, Bhubaneswar, Odisha, India.

List of Publications

1. M. Bönisch, **A. Panigrahi**, M. Calin, T. Waitz, M. Zehetbauer, W. Skrotzki, J. Eckert, Thermal stability and latent heat of Nb-rich martensitic Ti–Nb alloys, J. Alloys Compd. -Submitted.

2. **A. Panigrahi**, B. Sulkowski, T. Waitz, K. Ozaltin, W. Chrominski, A. Pukenas, J. Horky, M. Lewandowska, W. Skrotzki, M. Zehetbauer, Mechanical properties, structural and texture evolution of biocompatible Ti–45Nb alloy processed by severe plastic deformation, J. Mech. Behav. Biomed. Mater. 62 (2016) 93–105.

3. A. Grill, J. Horky, **A. Panigrahi**, G. Krexner, M. Zehetbauer, Long-term hydrogen storage in Mg and ZK-60 after severe plastic deformation, Int. J. Hydrogen Energy 40 (2015) 17144–17152.

4. **A. Panigrahi**, M. Bönisch, T. Waitz, M. Calin, J. Eckert, W. Skrotzki, M. Zehetbauer, Thermal stability of HPT-induced omega phase in biocompatible Ti–16.1 Nb alloys, Proceedings of the 7th International Conference on Solid-Solid Phase Transformations in Inorganic Materials PTM (2015), TMS USA, 263-268.

5. **A. Panigrahi**, M. Bönisch, T. Waitz, E. Schafler, M. Calin, J. Eckert, W. Skrotzki, M. Zehetbauer, Phase transformations and mechanical properties of biocompatible Ti–16.1 Nb processed by severe plastic deformation, J. Alloys Compd. 628 (2015) 434–441.

6. **A. Panigrahi**, N. Scheerbaum, P. Chekhonin, J. Scharnweber, B. Beausir, M. Hockauf, S. Sankaran, W. Skrotzki, Effect of back pressure on material flow and texture in ECAP of Aluminum, IOP Conf. Series: Mater. Sci. Eng. 63 (2014) 012153.

7. K. Ozaltin, W. Chrominski, M. Kulczyk, **A. Panigrahi**, J. Horky, M. Zehetbauer, M. Lewandowska, Enhancement of mechanical properties of biocompatible Ti–45 Nb alloy by hydrostatic extrusion, J.   Mater. Sci. (2014) 49: 6930-6936.

8. B. Sulkowski, **A. Panigrahi**, K. Ozaltin, M. Lewandowska, B. Mikułowski, M. Zehetbauer, Evolution of strength and structure during SPD processing of Ti–45 Nb alloys: experiments and simulations, J. Mater. Sci. (2014) 49: 6648–6655.

9. R. S. Turtelli, C.B. Nunes, K.T. Tiguman, D. Geist, **A. Panigrahi**, C. Grijalva, S. Sorta, R. Grössinger, Michael Zehetbauer, Antiferromagnetism and low Magnetostriction in Fe100−xMnx (x = 38, 42, 46, 50, and 55) alloys, IEEE transactions of magnetics 50 (2014) No. 4.

10. M. Bönisch, M. Calin, T. Waitz, **A. Panigrahi**, M. Zehetbauer, A. Gebert, W. Skrotzki, J. Eckert, Thermal stability and phase transformations of martensitic Ti–Nb alloys, Sci. Technol. Adv. Mater. 14 (2013) 055004.

List of Conference Contributions (Talks)

1. R. Chulist, M. Prokopowicz, **A. Panigrahi**, M. Zehetbauer, N. Schell, W. Skrotzki, Texture evolution of HPT-processed Fe-based shape memory alloys, ICFSMA 2016, 5th international Conference on Ferromagnetic Shape Memory Alloys, 5–9 September 2016, Miyagi (Japan)–Talk.

2. S. Tulić, M. Kerber, **A. Panigrahi**, T. Waitz, High Temperature Ti–Ni–Pd Shape Memory Alloys Subjected to High Pressure Torsion, CIMTEC 2016, Conferences Internationales Materiaux Et Technologies, 5–9 June, 2016, Perugia (Italy) –Talk.

3. T. Waitz, **A. Panigrahi**, C. Mangler, P. Schindler, C. Gammer, M. Peterlechner, P. Müllner, R.D. James, M. Matsuda, Phase transformation of alloys processed by severe plastic deformation, Euromat 2015, 20–24 September, 2015, Warsaw (Poland) – Invited Talk.

4. M. Matsuda, M. Kerber, **A. Panigrahi**, S. Tulic, T. Waitz, Microstructural characterization of high temperature TiPd and TiNiPd shape memory alloys subjected to high pressure torsion, 157th Fall Annual Meeting of Japan Institute of Metals and Materials, 16–18 September, 2015, Kyushu University (Japan) –Talk.

5. **A. Panigrahi**, M. Bönisch, T. Waitz, M. Calin, J. Eckert, W. Skrotzki, M. Zehetbauer, Thermal stability of bulk nanocrystalline ω-phase in Ti–16.1 Nb processed by high pressure torsion, ICSMA, 17th -International Conference on Strength of Materials, 09–14. Aug. 2015, Brno (Czech Republic) – Talk.

6. C. Ebner, M. Matsuda, **A. Panigrahi**, M. Kerber, C. Rentenberger, T. Waitz, Nanocrystalline B2 CoZr alloys processed by high pressure torsion, ICSMA, 17th -International Conference on Strength of Materials, 09–14. Aug. 2015, Brno (Czech Republic) – Talk.

7. M. Lewandowska, A. Krawczyńska, **A. Panigrahi**, E. Schafler, M. Zehetbauer, Precipitation process in nanostructured 7475 Aluminum alloy, International conference on solid-solid Phase Transformation in inorganic Materials, PTM-2015, 28 June – 3 July, Whistler, BC (Canada) – Talk.

8. **A. Panigrahi**, M.Bönisch, T. Waitz, M. Calin, J. Eckert, W. Skrotzki, M.Zehetbauer, HPT induced phase transformation in biocompatible Ti–16.1 Nb alloy, International conference on solid-solid Phase Transformation in inorganic Materials, PTM-2015, 28 June – 3 July (Canada) – Talk.

9. M. Matsuda, C. Ebner, **A. Panigrahi**, M. Kerber, C. Rentenberger, T. Waitz, B2 CoZr alloys processed by high pressure torsion, 156th Fall Annual Meeting of The Japan Institute of Metals and Materials, 18–20 March, 2015, University of Tokyo (Japan) –Talk.

10. **A. Panigrahi**, B. Sulkowski, T. Waitz, A. Hohenwarter, M. Zehetbauer, Mechanical biocompatibility of Ti-13Nb-13Zr processed by SPD: Symposium- Advanced Materials in Dental and Orthopaedic Applications, TMS 2015, 15–19 March, Orlando, Florida (USA) – Talk.

11. **A. Panigrahi**, B. Sulkowski, K. Ozaltin, T. Waitz, M. Lewandowska, W. Skrotzki, M. Zehetbauer, Texture evolution in bcc Ti–45 Nb after severe plastic deformation: ICOTOM17, 17th International Conference on Texture of Materials, Aug. 24–29, 2014, Dresden (Germany) – Talk.

12. B. Sulkowski, **A. Panigrahi**, K. Ozaltin, M. Lewandowska, B. Mikulowski, W. Skrotzki, M. Zehetbauer, Effect of texture on mechanical properties of Ti–45 Nb alloy: Experiments and Simulations: ICOTOM17, 17th International Conference on Texture of Materials, Aug. 24–29, 2014, Dresden (Germany) – Talk.

13. **A. Panigrahi**, N. Scheerbaum, P. Chekhonin, J. Scharnweber, B. Beausir, M. Hockauf, S. Sankaran, W. Skrotzki, Effect of backpressure on ECAP: NanoSPD6, 6th International conference on Nanomaterials by Severe Plastic Deformation, June 30–July 4, 2014, Metz (France) – Invited talk.

14. B. Sulkowski, **A. Panigrahi**, K. Ozaltin, M. Lewandowska, B. Mikulowski, M. Zehetbauer, Simulations of strengthening and structure fragmentation of SPD processed Ti–45 Nb biomedical alloy: NanoSPD6, 6th International conference on Nanomaterials by Severe Plastic Deformation 6, June 30–July 4, 2014, Metz (France) –Talk.

15. B. Sulkowski, **A. Panigrahi,** K. Ozaltin, M. Lewandowska, B. Mikulowski, M. Zehetbauer, Modelling and simulation of mechanical properties and microstructure of SPD nanostructured Ti–45 Nb biomaterials: TMS 2014, February 16–20 2014, San Diego, California (USA) – Talk.

16. **A. Panigrahi**, T. Waitz, E. Schafler, M. Bönisch, M. Calin, J. Eckert, A. Gebert, W. Skrotzki, M. Zehetbauer, Ultrafine grained Ti-Nb alloys for orthopaedics: TMS 2014, February 16–20 2014, San Diego, California (USA) – Talk.

17. B. Sulkowski, **A. Panigrahi**, B. Mikulowski, M. Zehetbauer, Simulation of strength and microstructure of Ti-Nb alloys for medical application: Conference on Computational Modelling and Nanostructured Materials (ICCMNM), September 3-6 2013, Frankfurt (Germany) – Talk.

18. M. Zehetbauer, **A. Panigrahi**, B. Sulkowski, B. Mikulowski, K. Ozaltin, M. Lewandowska, W. Skrotzki, M. Bönisch, M. Calin, J. Eckert, Enhancing Mechanical Properties of Biomedical Materials: Experiments and Modelling: Conference on Computational Modelling and Nanostructured Materials (ICCMNM), September 3-6 2013, Frankfurt (Germany) – invited Talk.

19. **A. Panigrahi**, T. Waitz, E. Schafler, M. Bönisch, M. Calin, J. Eckert, A. Gebert, W. Skrotzki, M. Zehetbauer, SPD processed TiNb alloys for orthopaedic applications: ICSMA 16th – International Conference on Strength of Materials, 19-24. Aug. 2012, Bangalore (India) – Talk.

List of Conference Contributions (Posters)

1. T. Waitz, M. Matsuda, M. Kerber, **A. Panigrahi**, High Temperature TiPd Shape Memory Alloys Subjected to Severe Plastic Deformation, International Conference on high-Temperature Shape Memory Alloys, HTSMAs 2015, 5 – 8 May, Wildbad Kreuth, (Germany)– Poster.

2. **A. Panigrahi**, B. Sulkowski, T. Waitz, M. Bönisch, M. Calin, J. Eckert, W. Skrotzki, M. Zehetbauer, Mechanical properties of orthopaedic Ti–Nb alloys after severe plastic deformations: NanoSPD6, 6th International conference on Nanomaterials by Severe Plastic Deformation, June 30–July 4, 2014, Metz (France) – Poster.

Awards and achievements:

- ✓ Awarded Marie Curie ITN fellowship PhD study in BioTiNet Project.
- ✓ Awarded Deutscher Akademischer Austausch Dienst (DAAD)-IIT scholarship during master project work in Germany.
- ✓ 46th All India Rank in Graduate Aptitude Test in Engineering (GATE) examination in Metallurgical Engineering.